Doctoral Dissertation
Doctoral Program in Energy Engineering (33^{th}cycle)

Research on the fluid dynamics in diesel injection systems, design of innovative closed-loop control strategies, assessment of a new flowmeter for high-pressure fluids and 1D modelling of liquid and gaseous flows

By

Oscar Vento

******

Supervisors:
Prof. Alessandro Ferrari
Prof. Antonio Mittica

Doctoral Examination Committee:
Prof. Giancarlo Chiatti, Referee, Università di Roma Tre
Prof. Petter Dahlander, Chalmers University of Technology
Prof. Jingping Liu, Referee, Hunan University

Politecnico di Torino
2021

Declaration

I hereby declare that, the contents and organization of this dissertation constitute my own original work and does not compromise in any way the rights of third parties, including those relating to the security of personal data.

Oscar Vento
2021

* This dissertation is presented in partial fulfillment of the requirements for **Ph.D. degree** in the Graduate School of Politecnico di Torino (ScuDo).

Abstract

The Common Rail (CR) injection system represents the most diversified fuel injection system for diesel engines. It allows high pressure injection levels and many injection events during an engine cycle. Due to its importance, it is still in-depth explored from different aspects and represents the main topic of numerous research works. The internal dynamics of the injector and modifications in the system layout are widely studied and injector manufacturers are focusing their work on different strategies to control the injected mass. In addition, the CR system presents many features still to be studied from the fluid dynamics point of view, leading also to the development of new measuring devices.

In this study, the fuel temperature effect on the CR hydraulic performance has been investigated. The measured temperature at the injector nozzle exit has been compared with the one obtained by means of a thermodynamic model in which the pump compression follows an isentropic process, while the process inside the injector is assumed as isenthalpic. This value is well correlated with the measured temperature, but it represents an overestimation. By means of a numerical model, the internal fluid dynamics process in an injector has been investigated with reference to the fuel temperature variations. For the considered temperature range, the main effect of the fuel temperature regards the needle lift trace and a higher needle lift peak value is reached when the fuel temperature augments.

The layout and the algorithm of an innovative flow-meter has been presented. It is able to measure the instantaneous flow-rate of a high-pressure flow with a superior dynamic response. A 3D model of an external gear pump, validated from the pressure point of view, has been used to further assess the accuracy of the presented flow-meter, by comparing the numerical flow ripple with the experimental one.

As far as the control strategies for the injected mass are concerned, an approach based on physical equations and one based on a TFA virtual sensor

are presented. In the former, the mass at the injector inlet is evaluated, which correlates well with the injected one. Hence, a closed-loop control has been set-up and tested by means of a rapid prototyping hardware. The ET provided to the injector solenoid is corrected, for each engine cycle, based on the predicted inaccuracy on the injected mass. Tests have been performed for both single and pilot-main injections. Pertaining to single injections, the error due to a different thermal regime experienced by the injector has been reduced below 1 mg, while for pilot-main injections, the oscillations amplitude of the overall injected mass with respect to the dwell-time has been reduced below 2 mg. The TFA-based technique consists in the estimation of the injection temporal length (ITL) by analysing the mean instantaneous frequency evaluated for the pressure trace at the injector inlet. This allows to control the injected mass by means of a correlation based on the ITL and the rail pressure, independent on the fuel temperature. For a wide range of working conditions (in terms of rail pressure and ET), the error in the injected mass estimation is below 1 mg.

Pertaining to the system layout, an innovative diesel injection system, the Common Feeding (CF), has been experimentally and numerically investigated. In this system the rail is substituted by an accumulation volume directly mounted on the pump, leading to a cost reduction and to an easier installation on the engine. The experimental campaign has been conducted by considering a CR system where the rail size has been varied, in order to understand which is its effect on the hydraulic performance, in terms of single and double injections. The performance of the CR system has been compared with the CF one. By means of a 1D numerical model, the effect of the different rail size has been investigated from the injector internal dynamics point of view.

Regarding to the 1D fluid dynamics simulations, the unsteady friction effect on simulations has been investigated. A 2 m long high-pressure pipe has been equipped with three piezoresistive transducers, the pressure time histories at the two extremities have been selected as boundary conditions of the pipe numerical model, while the one in the middle has been compared with the numerical outcomes. In addition, with a 1D numerical injector model the different unsteady friction techniques have been applied and compared. It has been observed that when two pressure signals are used as boundary conditions, no evident improvements are provided by the unsteady friction model, while when only one boundary condition is a pressure signal (as in the injector model)

the unsteady friction increases the accuracy of the results, but the improvement is not related to the selected method.

Finally, an analysis of the scopes to model compressible flows by means of the polytropic evolution has been performed. A new set of analytical equations has been proposed, which allows both the heat transfer and the wall friction. The steady-state flow properties obtained by means of the new equations have been compared with the ones of the Fanno flow. Limits of the polytropic assumption have been investigated by means of a numerical code, where a variable polytropic coefficient can be adopted. This method allows to reach the choking condition with a Mach number equals to 1. The proposed formulas are able to accurately predict the viscous diabatic flow properties distribution, if a local maximum in the temperature is not present. In addition, an analytical formula to obtain the Mach number corresponding to the maximum temperature featured by the flow has been deduced.

Keywords: Common Rail, fuel temperature, Common Feeding, closed-loop, flow-meter, polytropic, frequency dependent friction.

Acknowledgements

The work presented in this thesis was carried out at DENERG department of Politecnico di Torino, in Turin, from 2017 to 2021.

I want to sincerely acknowledge my advisors, Prof. Alessandro Ferrari and Prof. Antonio Mittica. Everything I learned is the result of their guidance and their constant support has made possible all the achieved goals.

I am also sincerly grateful to all the DENERG technicians who helped me in these years.

Finally, all my gratitude goes to my PhD colleagues, Tantan Zhang and Zhiru Jin, my PhD carrier would not be the same without them and without all the experiences shared together, especially during the experimental campaigns and the theoretical analysis.

to my family
to my friends
to my Love

Contents

List of Figures

List of Tables

Nomenclature

Roman Symbols

A pipe internal cross-section area

a speed of sound

A, $A*$ Vardy and Brown's approximated weigh function coefficients

a_k, b_k coefficients of the kth harmonic term

b annulus thickness

B, B^* Vardy and Brown's approximated weigh function coefficients

C Courant number

c constant specific heat of the polytropic evolution

c_1, c_2 constants of integration

C_c contraction coefficient

C_d discharge coefficient

c_p heat capacity at constant pressur

CF Common-Feeding

CFL Courant, Friedrichs and Lewy condition

CN cavitation number

CO carbon monoxide

CR Common Rail

$D,\ d$	pipe diameter
D_h	hole diameter
DC	duty cycle
DT	dwell time
E	total energy per unit of volume
E_b	bulk modulus
E_f	energy of a signal
ECU	Electronic Control Unit
EGR	exhaust gas recirculation
f	signal function
F_{fric}	friction force
FFT	fast Fourier transform
G	mass flow-rate
h	enthalpy
h_w	window function
HC	hydrocarbon
i	complex variable
IP	index of performance
ITL	injection temporal length
J	Bessel function of the first type, impulse
K	geometrical term
L	pipe length
l_w	global viscous power dissipation per unit of mass flow-rate

M integer number

m polytropic exponent

$m_k,\ n_k$ fitting coefficients

Ma Mach number

$MSPE$ mean squared percentage error

NCD nozzle closure delay

NCS Needle Closing Sensor

NO_x nitrogen oxides

NOD nozzle opening delay

$P_1,\ P_2$ pressure transducers

P_f energy density spectrum

p_v vapour pressure

Q volumetric flow-rate

q heat transfer per unit of mass flow-rate

R elasticity constant of a perfect gas

$R_1,\ R_2$ Riemann variables

Re Reynolds number

s Laplace complex variable, entropy

$STFT$ short time Fourier transform

T_p period

TFA time-frequency analysis

U section-averaged flow velocity

v needle velocity

V_{cc} control chamber volume

V_{dc} delivery chamber volume

W Zielke's weight function

W_{app} approximated weight function

Y Bessel function of the second type

$y_k,\ z_k$ discretization functions

z generic complex number

ET energizing time

FMV fuel metering valve

p_{nom} nominal rail pressure level

PCV pressure control valve

Greek Symbols

α variable associated to the viscosity

β thermal expansivity

Δt numerical time step

Δx numerical space step

δ flow regime coefficient

δ_r radial distance between the needle and the injector holder

η time variable

γ ratio between the heat capacity at constant pressure and the one at constant volume

λ friction factor

$\lambda_1,\ \lambda_2$ eigenvalues of the Euler equations

μ dynamic viscosity

ν kinematic viscosity

ω_k circular frequency of the kth harmonic

σ coefficient of variation

θ angular coordinate

ε roughness size

Mathematical Symbols

$\mathcal{J}_1$ first type modified ratio of the zero and the first-order Bessel functions

1D one-dimensional

3D three-dimensional

Subscripts and superscripts

. flux

0 stagnation property

1 pipe inlet

2 pipe outlet

$*$ pertaining to choking condition

θ along the angular coordinate

$\wedge$ Laplace domain quantity

acc accumulator

aft after injection

$ch, Fanno$ choking condition for the Fanno flow

$crit$ critical

dyn dynamic

est	estimated
exp	experimental
$Fanno$	pertaining to the Fanno flow
i	space index
lam	laminar
$main$	main injection
n	time index
num	numerical
p	at constant pressure
pil	pilot injection
pol	pertaining to the polytropic flow
s	following an isentropic process
st	steady-state contribution
T	following an isothermal process
u	unsteady
v	at constant volume
wou	without unsteady friction

Chapter 1

Introduction

Internal combustion engines are facing considerable challenges due to their role in energy consumption, environemental pollution and climate change [1].

Researchers and engineers are forced to achieve further progress on an already existing technology, driven by the more stringent and severe pollutant emission strandards [2]. All the elements of the powertrain are involved in this development. Improvements in the combustion chamber shape, affecting the soot formation and in-cylinder nitrogen oxides (NO_x) in diesel engines [3]. Development in the after-treatment systems through which a sensible reduction of pollutants can be achieved [4]. Optimization in the fuel injection system apparatus, that has a key role in a powertrain since combustion [5], emissions [6] and efficiency [7] are strongly related to the injection events.

The Common Rail (CR) fuel injection system has given many degrees of freedom in terms of injection timing, injection rate and number of injection events during a single engine cycle [8].

Due to its versatility, the CR system has been in-depth explored in many research activities, also by means of 1D numerical diagnostic tools, leading to the design of innovative control strategies to improve its performance, the development and optimization of new fuel injection system layouts and flow-meters and to enhance the quality of numerical simulations, regarding the overall injection system, the injector or the high-pressure pipelines, studied with the assumption of the 1D flow.

1.1 Thermal effects on the hydraulic performance of the CR injection system

The shape and the amount of fuel of every injection event are able to strongly affect the engine-out emission control and the combustion [9] and both the design parameters, related to the injector structure [10], and physical factors, i.e. the ambient conditions [11] and the fuel properties [12], must be correctly considered. If an injection is performed with an high pressure level and the nozzle features small injection holes, the optimal level of fuel atomization, easy evaporation and mixture homogeneity is achieved [13]. A reduction in terms of soot and hydrocarbon (HC) emissions, due to the diminished liquid length, leading to an attenuated impingement on walls can be coupled with a NO_x emission level reduction if a high EGR (exhaust gas recirculation) rate is simultaneously applied [14]. Moreover, the number and the position of the nozzle orifices are able to affect the jet interaction with the squish regions and the lift-off flame, due to modified in- and near-nozzle flow patterns [15].

The fuel temperature exerts its influence also on the spray development and, consequently, on the combustion evolution. For both a DME (dimethyl ether) and the diesel fuel, when the fuel temperature increases the maximum combustion pressure is reduced and, in addition, the combustion start is delayed, due to a faster evaporation and a lower fuel penetration. These effects permit to reduce NO_x emissions [16, 17]. However, a lower fuel temperature causes a non-uniform fuel-air mixture, leading to an increment in unburned HC and the time instant at which a constant level of evaporation rate is reached results to be delayed [18]. Biodiesel fuelled engines are particularly affected by these effects, in fact the fuel economy and the NO_x emission level are significantly different if the fuel temperature varies, when the engine operates under low EGR rates [19].

Pertaining to the spray development, the liquid penetration length is the most sensitive parameter to the fuel temperature. In fact, a reduction up to 15% can be noticed if the temperature changes from 15 ℃ to 70 ℃ [20]. If a pure biodiesel (B100), characterized by a high viscosity, is taken into account, the preheating fuel temperature has a key role. It has been seen that an augmented fuel temperature is able to enlarge both the spray area and the spray angle cone, which are usually smaller, for a certain temperature, compared to the

normal diesel fuel; besides, the pump efficiency improves (the viscous friction loses diminish with the fuel temperature) [21].

The fuel temperature effects on CR systems employed on marine diesel engines have also been studied: for a reduced fuel temperature, the initial momentum and surface tensions of the droplets increase, due to the increased fuel density, hence the droplet breakup results to be repressed [22].

The fuel flowing in the injection circuit is far to be isothermal. The biggest contribution of heat to the fuel tank is given by the returning lines of fuel throttled by the injectors pilot stages [23]. When the fuel is compressed by the pump, its temperature increases of 1 ℃ every 100 bar of compression. Pertaining to the injector, the inner fuel has been usually assumed as isothermal [24, 25]. This approximation leads to an underestimation of the temperature rise due to the passage through the nozzle orifices (the rise in temperature due to the dissipation is neglected) [26]. The changes of fuel properties with the temperature, in terms of bulk modulus [27], viscosity and density [24] modify the internal injector dynamics. If a ballistic injector is considered (under the usual working conditions the needle does not reach the upper stroke-end [28]), the needle dynamic is affected by the pressure and viscous forces, which are a function of the temperature [29]. Regarding to the nozzle orifices, a complex temperature pattern can be described by means of a 3D numerical simulation, highlighting different behaviour between the core flow and the boundary layer. As an example, for a 2000 bar injection, the maximum fuel temperature difference inside the described pattern can reach 80 ℃. If this difference is neglected, a remarkable difference in fuel properties is not taken into account [30].

1.2 Application of an innovative high-pressure flowmeter

The instantaneous high-pressure flow-rate of a complex hydraulic power system can only be predicted by means of numerical models, however, this implies to involve advanced modelling techniques from the hydraulics, mechanical and electronic points of view [31].

An high-pressure flowmeter should feature many characteristics, such as a reduced size and a non-invasive shape, the capability to operate at high-pressure and to have an adequate dynamic performance.

Positive displacement [32], Coriolis [33] and turbine [34] flow-meters feature an excessive size and a relatively low dynamic response [35]. Obstruction meters [36] are able to estimate the flow velocity by correlating it to the pressure drop measured across a calibrated orifice, but these kind of instruments are suitable only for steady-state measurements. Pertaining to the induction based flow-meters [37], despite their high dynamic performance, they require a working fluid featuring an electrical conductivity higher than 0.1 μS/cm, while diesel and gasoline fuels are characterized by a much lower conductivity than the just mentioned threshold [32]. Finally, flow-meters based on the laser Doppler velocimetry technique [38] require a high initial setup cost and they only allow to measure laminar flow-rates. In addition, the requirements from the setup point of view do not permit to overcome 100 bar of pressure [39].

Concerning to the flow-rate estimation techniques based on instantaneous pressure measurements, they are able to achieve a superior dynamic response with a compact size, both features of the pressure transducers [40]. If the system is characterized by a single direction pressure wave propagation, a mathematical link between one pressure time history and the flow-rate exists [41]. Nevertheless, a single pressure trace cannot be linked to the instantaneous flow-rate if the pressure waves travel back and forth along the considered duct [42, 43].

1.3 Development of a closed-loop control strategy for the injected mass

A CR system results to be servo-controlled, if the nominal rail pressure p_{nom} and the energizing time ET (the duration of the current signal) are fixed the injected quantity can be determined [44]. Values of p_{nom} and ET are stored into the ECU calibration maps, obtained by means of preliminary calibration tests [45]. Since no feedback signals are involved, the injected mass control is of the open-loop type. As far as a multiple injection is concerned, the injector opening and closure events trigger pressure oscillations or particular needle valve dynamics and these phenomena can affect the fuel injected quantity, therefore

the accuracy of the fuel dosage can become challenging [46]. Furthermore, for a fixed value of ET and p_{nom}, the effectively injected mass varies with the engine thermal regime [47].

The development of robust closed-loop control strategies for the injected mass in diesel injection systems represents the main topic of many studies [48]. For example, in [49] a mass sensing mechanism has been proposed for automatic fuel injection systems. This mechanism is based on two physical equations, the first is able to correlate the needle lift to the fuel volumetric flow-rate, while the second is used to determine the fuel properties by knowing the actual thermal regime.

An engine diagnostic model can also be used to estimate the injected mass, based on the value of the oxygen concentration at the exhaust manifold, measured by using a lambda sensor [50]. The estimation of the injected mass is performed by considering the difference in oxygen fractions between the total flow-rates entering and leaving the cylinder [51]. The latter is obtained by means of the engine model with the assumption of nil EGR fraction at the cylinder inlet, and it is compared with the measured one. Such a model requires accurate measurements at the intake and exhaust manifolds, in terms of both temperature and pressure, and a sophisticated calibration.

Another strategy is based on a miniaturized volumetric flow sensor integrated into the injector nozzle [52]. A thermoresistive measurement constitutes the base of the sensor working principle. The nozzle is equipped with a hot wire anemometer, with Ti/Pt metallization on a low temperature co-fired ceramic substrate, and the injected mass is obtained by considering the maximum deviation of a balanced Wheatstone bridge.

In recent years, different injection system manufacturers developed injectors featuring additional devices in order to increase the injected mass accuracy. Denso designed the *i*-ART injector [53], consisting in the application of a piezoelectric pressure sensor into the pilot stage. Some relevant key instants, such as the start of injection, the instant when the maximum injection rate is reached and the end of injection, are identified by analysing the acquired control chamber pressure trace [54]. Finally, by means of a flow-rate model, the injected mass is estimated [55]. The NCS (stands for Needle Closing Sensor) is a technology developed by Bosch. The basic principle is similar to the *i*-ART injector one. The force inside the control chamber due to the fuel pressure

is measured by means of a transducer and the relevant instants regarding to the upstrokes and downstrokes of the needle can be detected. Therefore, the estimation of the injected quantity is obtained by means of a model where the deduced needle lift trace is used [56]. The last relevant technology has been proposed by Delphi: the "Switch" technology [57]. An electric circuit inside the injector closes in two different ways when the non-ballistic needle reaches the nozzle seat or the upper stroke-end. Hence, by measuring the voltage, the two time instants pertaining to the opening and closure of the nozzle can be identified and the injected mass is evaluated by means of a need lift-based model. All the presented strategies are characterized by the usage of complex transfer functions and models between the measured quantity and the injected mass, leading to the difficulty to achieve a satisfactory control for different working condition. For this reason, these technologies can be considered as compensative strategies for the injected mass instead of closed-loop controls.

Particular injection strategies, such as the digital rate shaping, allow to obtain discontinuities in the injection patter, leading to a more controllable heat release growth and a reduced peak of heat release rate. Soot emissions and combustion noise result to be reduced [56, 58], as well as benefits in fuel economy can be achieved [59]. If ramp-type or boot-type shapes are considered, a decrement in soot, carbon monoxide (CO) and hydrocarbon engine out emissions can be achieved [60, 61].

Generally, solenoid or piezoelectric injectors are able to perform these complex injection strategies [62]. However, hydraulic instabilities, below a certain dwell-time (DT) value, are not avoidable [46]. As an example, the overall injected mass of a pilot-main injection can anomalously increase for small changes in DT, in the short dwell-time range [46, 63].

A new tool applied in the analysis of non-stationary signals is the time-frequency analysis (TFA) [64]. It has been employed to detect and diagnose machinery faults [65, 66] and it has been used in diesel engines in order to study the combustion and knock by evaluating the engines vibration signals [67, 68]. A signal in the time domain is usually characterized in the time-frequency one by means of the short-time Fourier transform (STFT). Characteristic combustion parameters as the peak combustion pressure and peak pressure rise rate have been estimated with this technique [69].

1.4 Numerical and experimental analysis of the Common Feeding injection system

In the last years, different contributions improved the CR system under different aspects. The employment of the pressure balanced pilot valve to the solenoid injectors has given the chance to reach higher nominal pressures with low static leakage, reducing the energy consumption [70]. In addition, an integrated Minirail inside the injector helps to damp the pressure waves and different injector inner leakage paths are removed [71, 72]. The control chamber has been equipped with an innovative device, the control-plate, in order to restrain the fuel flowing across the pilot valve, when it is open [54].

Besides, the structure of the entire injection system has been taken into account for further optimizations [73]. Nowadays, a key point of the design of new injection system regards an optimum trade-off between a low-priced layout and the capability to maintain high-performance targets [74]. A progressive reduction of the rail size (from 20 cm^3 to 5 cm^3) has been investigated and this modification did not affect the injection system performance for a wide range of working conditions [43]. Among the different proposed optimizations, the Common Feeding (CF) injection system, featuring the absence of the rail (a chamber is directly integrated in the high-pressure pump), results to be an optimal opportunity to achieve a reduction in manufacturing costs (the rail is removed) and to allow an easier installation by keeping the overall performance [43, 75].

1.5 Assessment of unsteady friction models in high-pressure flows simulation

The choice of the method to model the skin friction can lead to a discrepancy between an experimental pressure trace and the correspondent numerical one obtained for a 1D transient flow [76]. During or after a sharp change in the flow velocity, the shear stress on the pipe walls can significantly deviate from the one corresponding to the steady flow. This difference can become unacceptable if is required to know the shape of a wave front, together to its amplitude [77].

Frequency dependent friction (or unsteady friction) simulation is, nowadays, a challenging subject and different researches [78–81] have been focused to this topic, due to its wide range of application.

The unsteady friction is used when an impulsive event, such as the water hammer, is analysed. Generally, it has been seen that when a fast change involves the flow properties it is required to appropriately evaluate the head loss, in fact the standard steady-state models are not able to provide a satisfactorily matching between the numerical results and the experimental data [82]. Different applications in which a water-hammer like phenomena occur require a correct estimation of the unsteady friction: start and stop phases of a pump, opening and closure of a valve [83–85]. Moreover, when the acoustic cavitation events take place [86], the steady-state friction is not enough during the simulation of cavitation collapse, that is regarded as a dynamic shock [87].

As far as a more gently varying unsteady flow is concerned, the unsteady friction tends to modify the acceleration and deceleration phases of the flow, with respect to the standard steady friction. In addition, also the resonance conditions in forced oscillation systems result to be affected by the frequency dependent friction, which finds another application in the evolution of railway tunnels steep fronted pressure waves [88].

Obstructions [89], leakages [90, 91] or clogging in pipelines give an effort to the damping of a sharp transient event, and the analysis of the propagation of a purposely-induced pressure wave can be applied to detect them. In these kind of applications, the frequency dependent friction must be considered, in order to avoid to neglect an important damping contribution of pressure waves, and its effect could be wrongly imputed to other causes. From studies focused on the instantaneous flow-rate measurement on 1D transient flows one has been seen that the unsteady friction implementation can help the results accuracy [92]. Finally, numerical-experimental activities regarding fluid power systems [93] and pneumatic brake circuits [94], have shown the importance of the frequency dependent friction modelling in these applications.

During its operation, the Common Rail fuel injection system presents many impulsive events. In fact, at the end of every injection, when the needle reaches its downstroke end and closes the nozzle, a water hammer event is triggered [95]; more in general, both the injector and the pump working induce high-frequency pressure waves along the injector feeding pipe [96].

1.6 Compressible 1D flows in constant area ducts

In the early 20th century, Fanno and Rayleigh developed theoretical models to analyse compressible steady-state flows through one-dimensional constant cross-section pipes. The Fanno model has been developed by assuming a viscous adiabatic flow, whereas the Rayleigh model has been obtained by means of the hypothesis of an inviscid diabatic flow [97]. These models, based on mass, momentum and energy conservation equations [98], are able to provide a closed-form prediction of the flow properties along the duct, for a certain assigned set of boundary conditions [99]. Concerning to the diabatic viscous flow, at the moment it has not been solved in closed form, neither for steady-state conditions [100], hence only numerical solutions exist.

Compressible flows in pipes, ducts, or in other configurations in which friction, kinetic energy and heat play a key role for technical problems, are often diffused in engineering industrial systems [97, 101, 102]. By means of a correct determination of the choking limits it is possible to improve the design of helium-cooled graphite beam stops, where an evolution whit friction and heat flux is considered for the monoatomic gas in a constant area pipe [103]. The effects of wall friction and heat on subsonic flows have been numerical analysed for buried high-pressure pipelines, characterized by a non-negligible convective heat transfer with the exposed ground surface [104]. The qualification and sizing of safety devices, as rupture disks and pressure relief valves, the analysis and layout of process gas distribution systems and the modelling of accidents consequences and release rates in nuclear and chemical industries [105], all force the engineers to manage one-dimensional compressible flows with significant kinetic energy transfer and friction losses. In addition, when a long duct is taken into account, the heat transfer cannot be neglected [106], and only numerical solutions are available.

Another recent important application regards fluid channels applied in cooling systems for electronics, where the miniaturisation leads to high dissipated power densities in numerous devices where efficient micro-scale fluid systems are required. When a micro-flow is considered the surface friction becomes dominant over the inertial effects and, if gaseous flows are taken into account, the compressibility becomes not negligible [102]. Heat pumps, reactors and

heat exchangers in aerospace engineering [107, 108], such as mixing chamber for ejectors [109], are diffused applications of capillarity tube flows. Furthermore, one-dimensional compressible flow models span from vacuum or pressurised systems [102] to heavy-duty gas turbines [110], and from bioengineering systems to blowdown wind tunnels. The intake and exhaust systems of an internal combustion engine are usually modelled by means of 1D compressible viscous flows.

Different works have been focused on the evolution of a compressible flow in constant cross-section area pipe from a theoretical point of view. Due to the flow compressibility, friction is not constant and it cannot be estimated by means of the canonical fluid dynamic correlations (e.g., Blasius and Colebrook-White), since they were obtained from experimental campaigns based on incompressible flows. It has been seen [111, 112] that compressibility tends to make the velocity profile more flat (similarly to the turbulence effect). As a consequence, the velocity gradient at the wall, which depends on the friction, results to be modified and a flattened velocity profile also affects the flow temperature and pressure.

As far as the heat flux is concerned, it is usually assumed as constant along a pipe to make the analysis easier [100], but a variable heat flux model can often be more appropriate; different correlations, such as those of Sieder-Tate [113] and Dittus-Boelter [114], are available in the literature and hold for incompressible flows, and express the Nusselt number as a function of both Prandtl and Reynolds numbers.

When the flow cannot be considered as incompressible, an accurate compressible correlation for the friction coefficient and for the convective heat transfer coefficient should also include the Mach number. Different research works have been done on compressible correlations for heat transfer and friction coefficients in compressible flows, for both laminar and turbulent flow conditions [100, 112, 115, 116].

The extension of the model to real gases, vapours [117] and mixtures [118] represent another important branch of compressible flow theoretical works. From [119], where a homogeneous two-phase flow (with both liquid and vapour) is considered, it has been seen that Fanno's flow could be extended to a cavitating flow, as already stated in [118].

1.7 Contributions and outline

In this work, the effect of the fuel temperature on the CR system performance has been analysed and an innovative flowmeter has been assessed. In addition, different innovative closed-loop strategies for the injected mass have been developed. The new CF injection system, manufactured for the Chinese light duty commercial vehicles market, has been characterized. As far as the numerical simulations are concerned, the effect of the frequency dependent friction in 1D simulations has been investigated and the scopes of the polytropic approach in modelling compressible flows through constant cross-section pipes have been in-depth explored.

In Chap. 2, the sensitivity of the injector working conditions on the fuel temperature has been analysed. The temperature at the injector outlet has been measured and a comparison with the one obtained by means of a thermodynamic model has been performed. In addition, a one-dimensional numerical diagnostic model of the injector has been used to understand the internal injector dynamics, in terms of needle lift and pressure in the control chamber.

In Chap. 3, an innovative flowmeter has been used to measure the instantaneous high-pressure flow-rate delivered by an external gear pump and its accuracy has been further assessed by means of a 3D numerical model. The innovative flowmeter algorithm is based on the measure of two pressure signals along the delivery line fed by the pump. This chapter is based on what is published in [120].

In Chap. 4, two new strategies to predict and control the injected mass have been presented. The working principle is based on the analysis of pressure time histories measured, by means of piezoresistive transducers, along the rail-to-injector pipe. The first method is based on physical equations and it has been tested thanks to a rapid prototyping hardware, the other uses a TFA-based tool. Both single and pilot-main injections have been considered in the experimental campaign. After the assessment of the new control strategy, a comparison in terms of injected mass accuracy between the standard CR system and the injection system equipped with the innovative control based on physical equations has been performed. The content reported in this chapter is based on what is published in [121] and [122].

In Chap. 5, a prototypal version of the Common Feeding injection system has been designed and manufactured in order to match the requirements of a light duty commercial diesel engine for the Chinese market. Tests have been performed for both the CR and the CF systems, in terms of single injections and double injections (both pilot-main and main-after schedules). The effect of the rail size in the CR system performance has been investigated by means of an hydraulic characterization of the CR with four different accumulation volumes. The overall performances between the CR and the CF systems have been compared. Finally, a 1D numerical diagnostic tool of the injector has been used to better understand the internal injector behaviour when the rail size is modified. The content of this chapter is based on a research article published in [123].

In Chap. 6, the pressure time histories of a long, high-pressure pipe have been numerically obtained. The numerical outcomes have been compared with the experimental traces measured by means of a pressure transducer mounted on the considered pipe. A review and a benchmark of the different frequency dependent friction models have been performed by means of a comparison between the different models results. The effect of the unsteady friction on a CR system has been investigated by means of a 1D diagnostic model. The presented work is based on what is published in [124].

In Chap. 7, a general polytropic modelling approach has been used in the simulation of compressible flows with both wall friction and heat transfer, along a constant cross-section pipe. One task is to obtain explicit solutions that can be used in fast engineering or design tools where a 1D compressible flow is involved. In order to validate the proposed approach based on a new set of analytical relations, the results have been compared with the ones of the Fanno model. Another objective is represented by the definition of the polytropic model scope in compressible flow simulations along a pipe. Thanks to this investigation, theoretical researches on Fanno subsonic flows approximation by means of a polytropic expression, in order to evaluate the mass flow-rate and the pressure drop in choking condition, have been extended [101, 125, 126]. The content presented in this chapter is based on a research article published in [127].

Chapter 2

Thermal effects on the hydraulic performance of a Common Rail injection system

2.1 Experimental setup

The experimental campaign has been carried out on the Moehwald Bosch hydraulic test bench installed at the ICE laboratory of Politecnico di Torino. The bench is able to provide a nominal power of 35 kW, a maximum torque of 100 Nm and a maximum speed of 6100 rpm. In order to measure instantaneous pressures and temperatures at several locations in the high-pressure hydraulic circuit of the fuel injection system, the bench is instrumented with piezoresistive pressure transducers and thermocouples. The electrical current signals to the injectors have been measured through a current clamp.

The injected mass and the injected flow-rate pattern has been measured by means of the HDA flowmeter [128]. As far as the injector fuel leakages are concerned, they have been detected with the KMM device [70]. The HDA flowmeter employees Zeuch's method to obtain the injected mass flow-rate: the pressure time history in a closed volume where the injection occurs is measured and, by evaluating the speed of sound in the chamber through an ultrasonic sensor, the injected flow-rate is obtained. At the end of an injection cycle, a certain fuel quantity is discharged in order to restore the initial pressure in the chamber.

Shell V-Oil 1404 (ISO 4113) calibration fluid is used in the hydraulic test bench, since it is able to reproduce the diesel fuel properties over an appropriate temperature and pressure range.

A Bosch CR diesel injection system for passenger car has been adopted. A high-pressure rotary pump, featuring a double effect single piston and a displacement of 430 mm^3/rev, has been used to deliver the high-pressure fuel to the rail. Tests presented in this chapter have been performed with a solenoid actuated CRI 2.18 injector, and its scheme is reported in Fig. 2.1. It is equipped with a pressure balanced pilot valve.

Pertaining to its working principle, high-pressure fuel enters the injector through the rail-to-injector pipe. A part of the fuel reaches the delivery chamber (volume V_{dc}), located upstream of the nozzle zone, while the other fuel part reaches the control chamber (volume V_{cc}) passing across the Z hole.

When the ECU switches on the electrical current to the solenoids, the pilot valve discharges the control volume through the A hole, therefore, forces acting

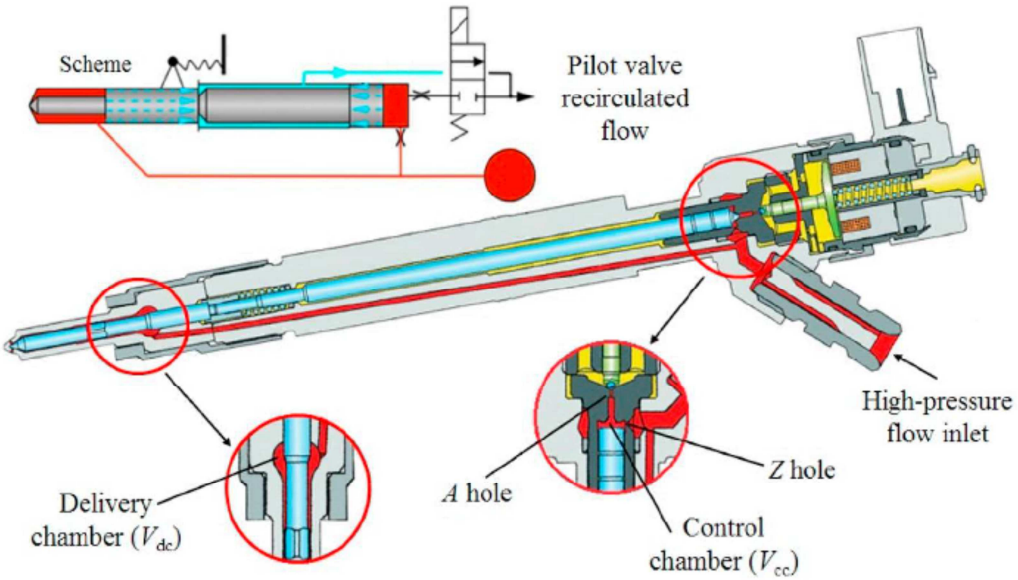

Figure 2.1: CRI 2.18 solenoid injector.

on the needle result unbalanced. The needle starts its opening phase, the nozzle results to be opened and the fuel is injected through the injection holes. When the electrical current to the solenoid is switched off by the ECU, the pilot-valve stops the discharging of the control chamber, making the pressure rise: this induces the needle closure phase. The injection phase ends when the needle reaches its downstroke and the nozzle is again closed.

The whole experimental campaign presented in this chapter has been performed at a fixed pump speed of 2000 rpm, corresponding to an engine speed of 2000 rpm. Since no obvious effects on the CR performance can be ascribed to the pump speed, the results can be generalized to other engine speeds.

The injector feeding pipe has been equipped with a piezoresistive transducer, mounted 4 cm far from the injector inlet, to measure the pressure time history ($p_{inj,in}$) that will be used as a boundary condition for the 1D injector diagnostic model. The adopted transducer is able to measure pressure up to 2000 bar and its linearity error is below $\pm 0.1\%$ of the fuel scale value. It has been assumed that the uncertainty is only ascribable to the linearity error, that is lower than ± 2 bar.

A PT100 temperature sensor has been used to measure the fuel temperature at the nozzle hole exit. It has been mounted 25 mm below the injector tip along a duct where the fuel is injected (the counterpressure is 40 bar). The same injector characterized from the hydraulic point of view on the HDA has been moved to the pipe equipped with the P100 sensor in order to measure the injected fuel temperature under the same working conditions.

In this analysis, single injections have been considered and different ET values have been selected for 800 bar, 1400 bar and 1700 bar of p_{nom} level. The fuel temperature in the tank (T_{tank}), almost coincident with the one at the pump inlet, as been selected in a range from 28 ℃ to 68 ℃. The former value represents the smallest temperature that can be set in the test rig while the latter is the maximum available temperature (for safety reasons).

2.2 Fuel properties and temperature evolution in the CR apparatus

All the fuel properties are affected by the temperature. The ones taken into account in this analysis are the density ρ, the bulk modulus E_b and the dynamic viscosity μ. As a consequence, the thermal expansivity $\beta = -\frac{1}{\rho}\left(\frac{\partial \rho}{\partial T}\right)_p$ can be calculated. In Fig. 2.2 the trends of the ISO 4113 oil properties are reported, as a function of the temperature, for different rail pressures [24], symbols represent the experimental values, while the solid lines stand for the polynomial interpolating expressions.

The test rig is able to precisely control the fuel tank temperature (T_{tank}). If an isentropic compression is assumed through the pump, the temperature increment due to the compression can be estimated. Under the assumption of an isentropic compression, the fundamental thermodynamic relation can be

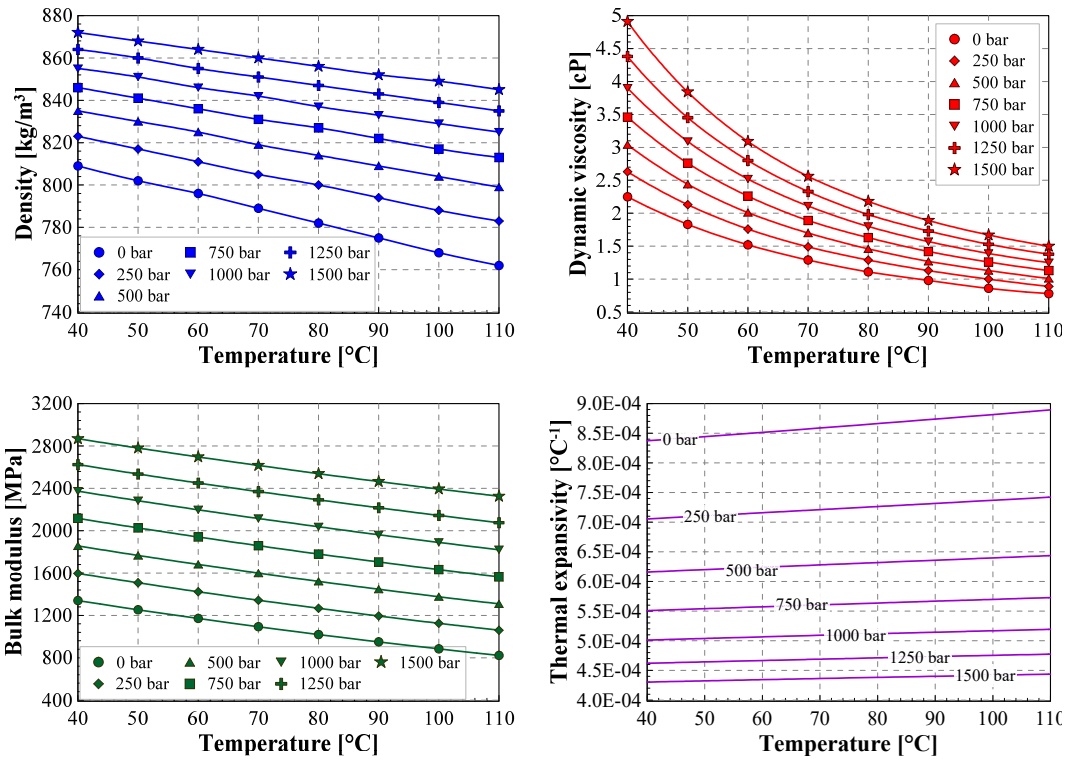

Figure 2.2: ISO 4113 oil properties for different temperatures and pressures.

written as:

$$dh = \frac{dp}{\rho} \tag{2.1}$$

where p is the flow pressure and h represents the enthalpy. For a liquid, the enthalpy can be expressed as:

$$dh = c_p dT + (1 - \beta T)\frac{dp}{\rho} \tag{2.2}$$

where c_p stands for the specific heat at constant pressure, while T is the fuel temperature. By combining Eqs. (2.1) and (2.2), one has:

$$c_p dT = \beta T \frac{dp}{\rho} \tag{2.3}$$

From Eq. (2.3) it is possible to obtain an estimation of the temperature in the high-pressure circuit, for a certain compression. By means of an isenthalpic process the fuel temperature through the injector can be obtained [24], if the injector is modelled as a series of restrictors. The injected fuel temperature can be estimated by means of the following relation:

$$c_p dT = (\beta T - 1)\frac{dp}{\rho} \tag{2.4}$$

2.3 Experimental results

Fig. 2.3 shows the trend of the measured fuel temperature at the nozzle exit when ET is varied ($p_{nom} = 800$ bar), for both $T_{tank} = 40$ °C and $T_{tank} = 68$ °C. As can be inferred from Fig. 2.3, after a certain value of ET the temperature stops to rise and reaches a constant asymptotic value. This trend can be interpreted by considering the applied measuring procedure. When the injection is short (small values of ET), the injected flow-rate is not enough to let the sensor to correctly measure the steady-state temperature. On the other side, if the ET increases the measured temperature grows till an asymptotic value, that is the one compared with the isenthalpic one. In addition, these measured temperature values (obtained for different rail pressure level) have been used as an input datum in the numerical model, at the nozzle outlet. In Fig. 2.4 the measured fuel temperature (corresponding to $ET = 3000$ µs) is reported with respect to the corresponding temperature obtained, for a certain pressure,

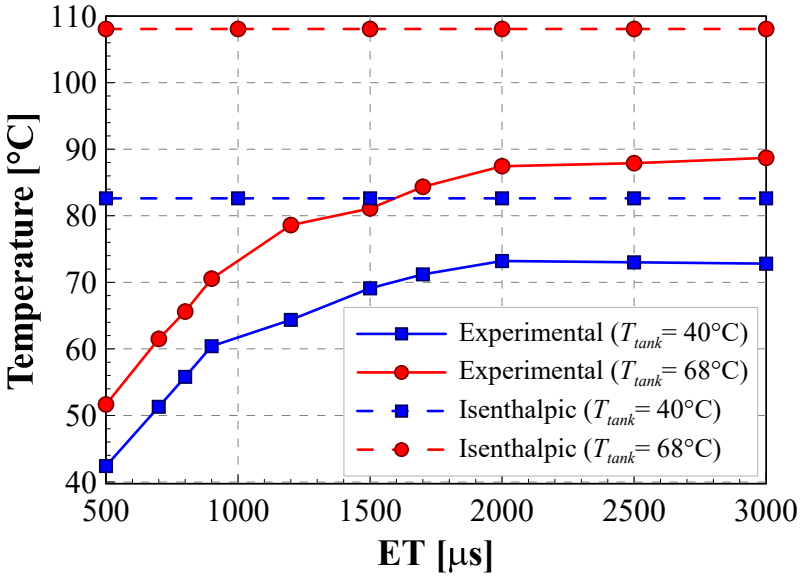

Figure 2.3: Fuel temperature measured at the nozzle exit (p_{nom}=800 bar).

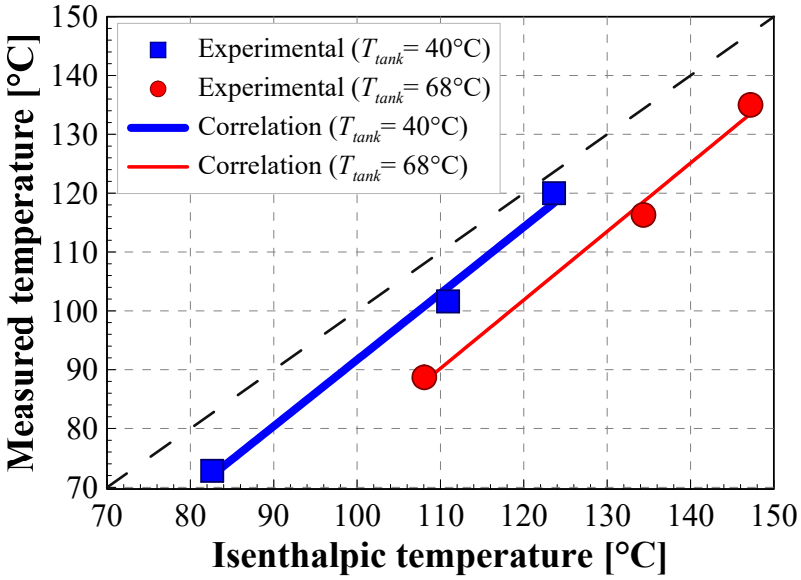

Figure 2.4: Correlation between the isenthalpic temperature and the measured one at the nozzle exit.

by following the isenthalpic process, for both 40 °C and 68 °C of T_{tank}. Even if the curves are not close to the bisector and by considering that with the isenthalpic assumption the temperature is overestimated, it results to be a reasonable estimation. Moreover, the two temperatures are well correlated.

As a consequence, for a fixed T_{tank} and p_{nom}, the isenthalpic temperature at the nozzle can be calculated by means of Eq. (2.4) and an estimation of the real temperature can be obtained through a correlation, determined for each injector typology.

Fig. 2.5 reports the injected flow-rates for two different T_{tank} ($p_{nom} =$ 1600 bar, $ET = 600$ µs). As can bee seen, the injection temporal length (ITL) augments with T_{tank}, leading to an increased injected fuel quantity, for fixed ET and p_{nom}.

2.4 Model description

A 1D numerical diagnostic tool of the injector, developed and already calibrated in previous works [31, 124] has been employed for this analysis. A scheme of the one-dimensional model is reported in Fig. 2.6. The developed numerical model considers all the main hydraulic characteristics of the injector, together with the electromagnetic setup and the mechanical components. It is constituted as a network of zero-dimensional chambers (cf. Fig. 2.6) connected by means of 1D pipes, which are solved through a Lax-Wendroff scheme. The considered forces can be ascribed to hydraulic, mechanical and electromagnetic effects and all the moving components are governed by the Newton laws of

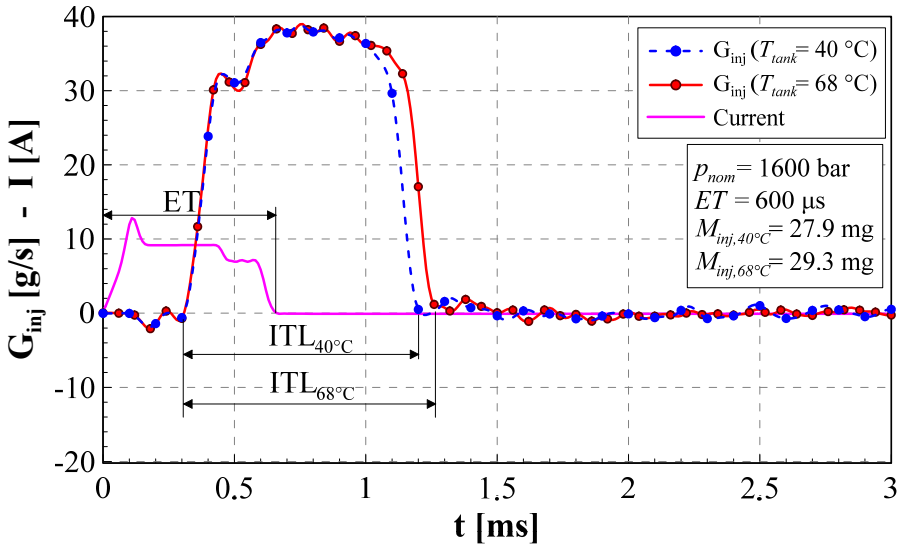

Figure 2.5: Injected flow-rate for $T_{tank} = 40$ °C and $T_{tank} = 68$ °C ($p_{nom} = 1600$ bar, $ET = 600$ µs).

motion, written in the ordinary differential form. The provided boundary conditions are the measured pressure trace at the injector inlet ($p_{inj,in}$) and the energizing current signal to the injector pilot stage solenoid. In the annular passage, when the needle moves, the presence of a thin fluid boundary layer between the needle and the injector body generates a viscous force. This flow layer follows the Poiseuille law. The viscous friction acting on the needle can be expressed as [129]:

$$F_{fric} = \frac{\mu \cdot L_c \cdot v \cdot \pi \cdot d_n}{\delta_r} \tag{2.5}$$

where d_n is the needle diameter, L_c is the length of the annular passage, v is the velocity of the needle and δ_r represents the radial distance between the needle and the injector holder.

The needle movement is linked to the pressure variation in the control chamber, that depends on the control chamber discharge and refilling phases, across the A and Z holes, respectively (cf. Fig. 2.6). The Z hole is usually non-cavitating, while the A hole can experience cavitation [130].

The general definition of a discharge coefficient is given by the ratio between the effective flow-rate to the ideal one, where the latter is obtained by applying the Bernoulli equation for a liquid flow [131]. If a hole does not experience cavitation, the discharge coefficient C_d is defined as follow [132]:

$$C_d = C_{d,max} \cdot \tanh\left(\frac{2 \cdot Re}{Re_{crit}}\right) \tag{2.6}$$

where $C_{d,max}$ is the maximum discharge coefficient, Re is the Reynolds number and Re_{crit} is the critical Reynolds number, which is the threshold between laminar and turbulent flow conditions. The Reynolds number is evaluated by means of the following relation:

$$Re = \frac{D_h}{\nu} \cdot \sqrt{\frac{2 \cdot \Delta p}{\rho}} \tag{2.7}$$

where D_h is the hole diameter, ν is the fluid kinematic viscosity and Δp stands for the pressure drop across the hole. When the flow, passing through a hole, is subjected to cavitation, the cavitation number CN is introduced [133]:

$$CN = \frac{p_1 - p_v}{p_1 - p_2} \tag{2.8}$$

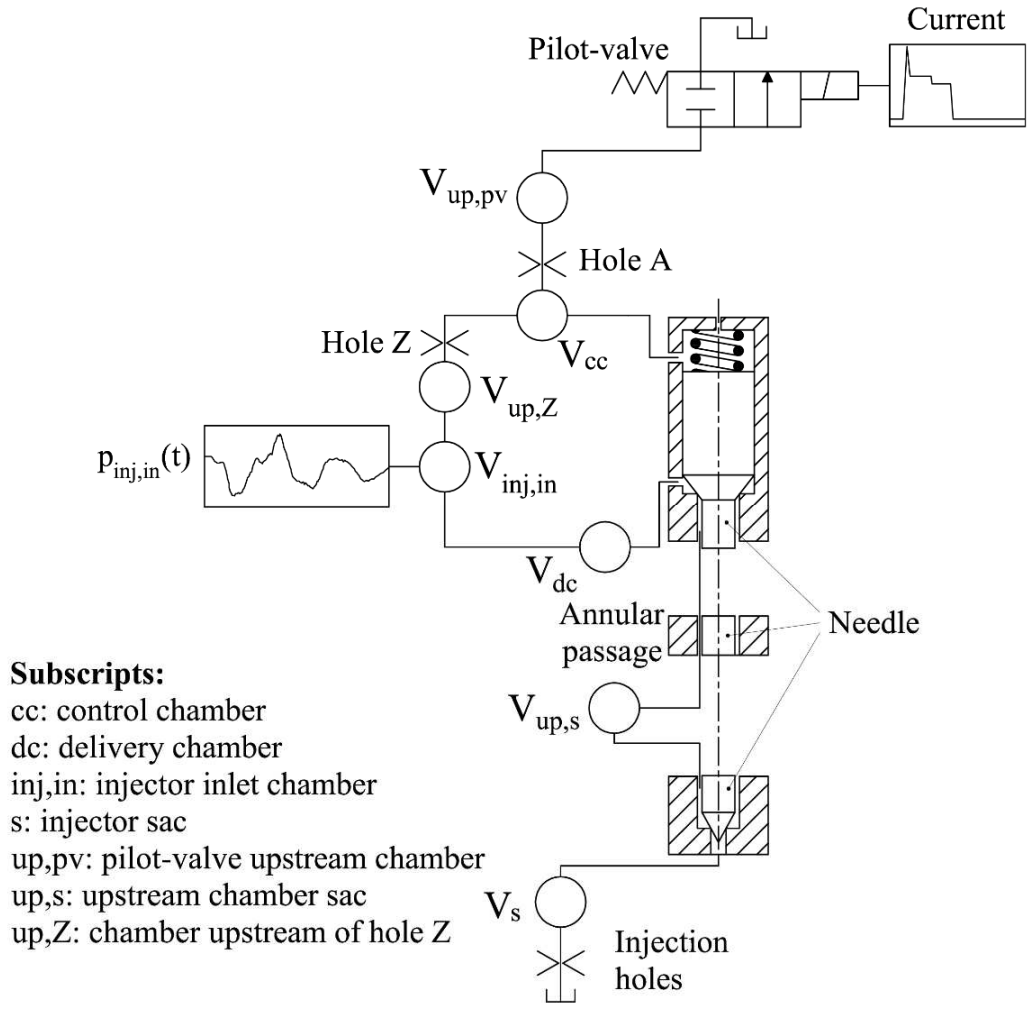

Figure 2.6: Scheme of the 1D injector diagnostic tool.

where p_1 is the pressure at the hole inlet, p_2 stands for the pressure at the hole outlet and p_v represents the vapour pressure of the fuel. Below the critical cavitation number, namely CN_{max} (that is experimentally obtained), C_d is evaluated by taking into account the actual CN and the contraction coefficient C_c [134]:

$$C_d = C_c \cdot \sqrt{CN} \tag{2.9}$$

In the present analysis, the C_d for the flow across Z is obtained with Eqs. (2.6) and (2.7), while the complete submodel involving CN, given by Eqs. (2.6)-(2.9) is applied for the A hole and the nozzle holes, in order to take into account possible cavitation phenomena.

2.5 Numerical model results

Fig. 2.7 reports the experimental injected flow-rates (represented with symbols) and the numerical ones (represented with continuous lines) for two values of nominal rail pressures, namely 800 bar (cf. Fig. 2.7a) and 1700 bar (cf. Fig. 2.7b). In this case the fuel temperature in the tank was set at 40 °C and different ET values have been considered. The corresponding results pertaining to $T_{tank} = 68$ °C have been reported in Fig. 2.8. In both the cases, the numerical results accurately predict the experimental flow-rates.

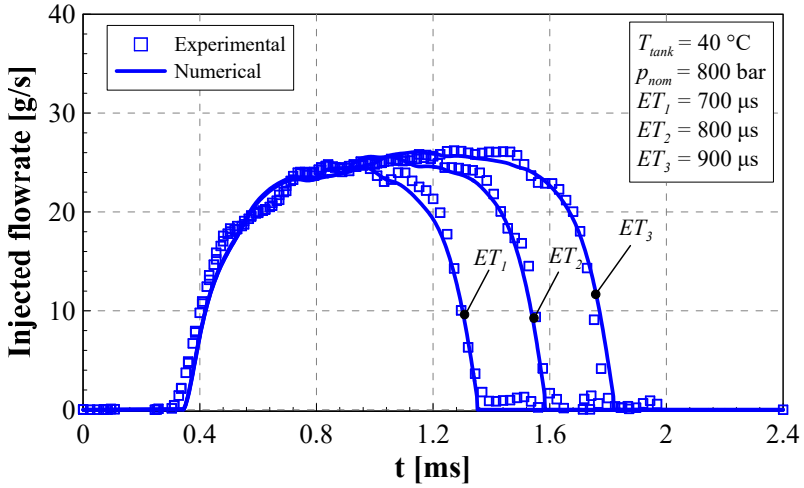

(a) $p_{nom} = 800$ bar

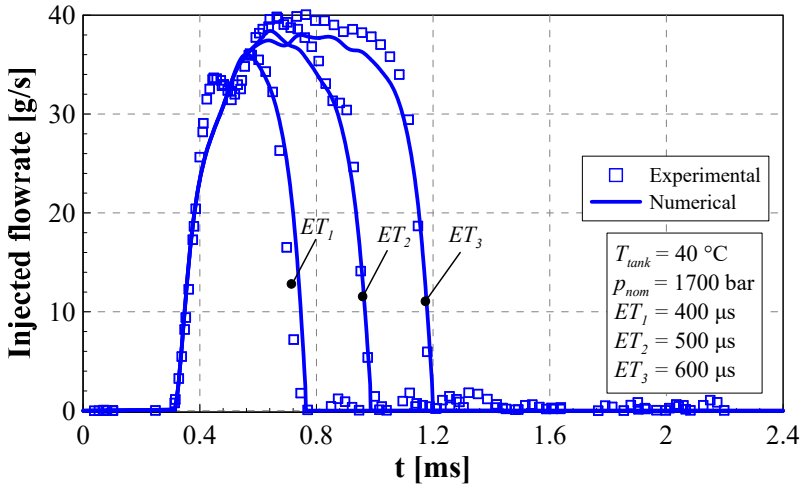

(b) $p_{nom} = 1700$ bar

Figure 2.7: Comparison between the numerical flow-rates and the experimental ones, for different ET values ($T_{tank} = 40$ °C).

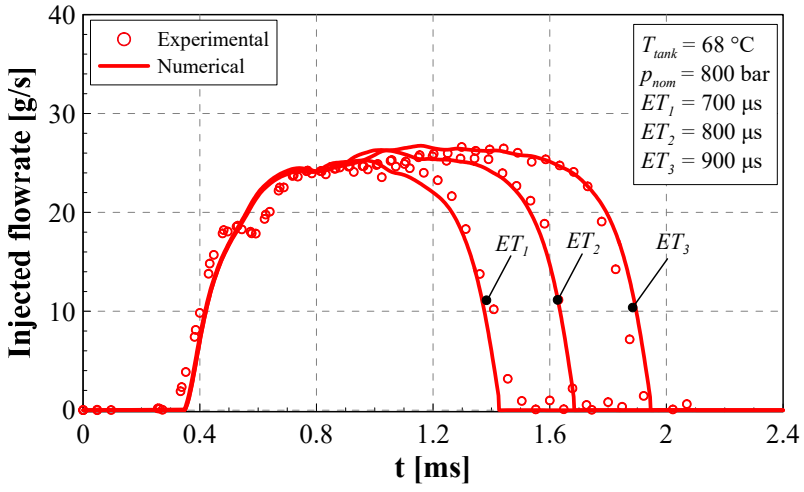

(a) $p_{nom} = 800$ bar

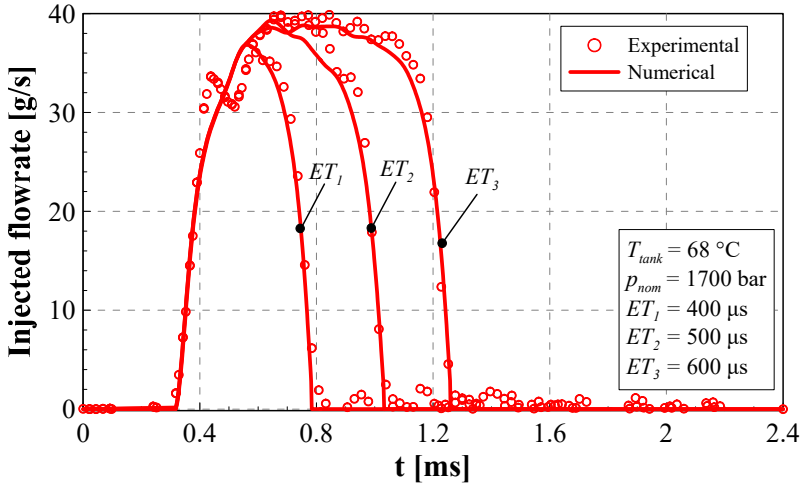

(b) $p_{nom} = 1700$ bar

Figure 2.8: Comparison between the numerical flow-rates and the experimental ones, for different ET values ($T_{tank} = 68$ °C).

Figure 2.9 shows the control chamber pressure time histories for both the considered fuel temperatures in the tank ($p_{nom} = 800$ bar, $ET = 800$ µs). As can be noticed, there is not a significant effect of the fuel temperature on the pressure traces in the control chamber, in fact both the flow-rates through the A and Z holes are almost identical in the two cases. This outcome is in line with the results present in the literature: the effect of the fuel temperature on the pressure trace inside the control chamber, namely the flow-rates across the Z and A holes, becomes significant only if the temperature at the injector inlet is below 0 °C [130]. For both the considered T_{tank} temperatures, the A

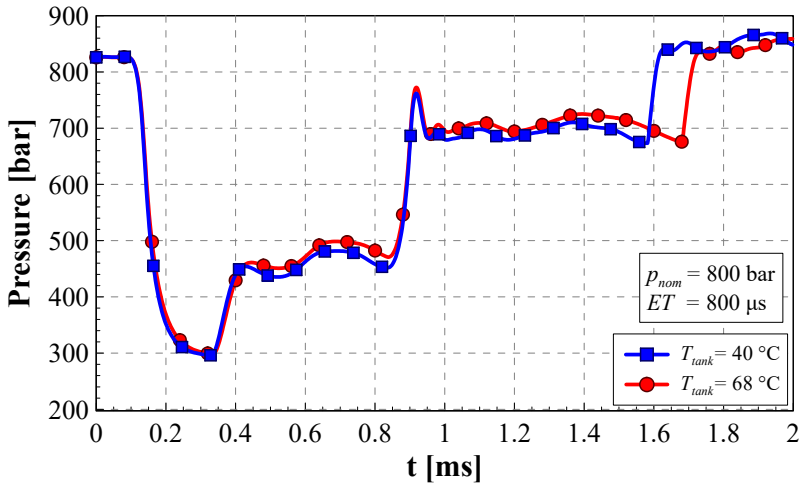

Figure 2.9: Pressure traces inside the control chamber for $T_{tank} = 40$ °C and 68 °C ($p_{nom} = 800$ bar, $ET = 800$ µs).

hole experiences cavitation but only a small increase in the CN can be noticed when T_{tank}=40 °C (the vapour pressure p_v decreases with the temperature), this results in a slight increase in the C_d value. On the contrary, the Z hole never reaches the cavitation condition and the flow is turbulent for both the T_{tank} values.

In Fig. 2.10 the numerical needle lift trace together with the pressure traces detected inside the delivery chamber (p_{dc}), the injector sac (p_{sac}) and the upstream-sac chamber ($p_{up,s}$) (cf. Fig. 2.6) are represented, related to $p_{nom} = 800$ bar, $ET = 1000$ µs and $T_{tank} = 40$ °C. The temperature at the injector inlet, applied to the chamber labelled as $V_{inj,in}$ in Fig. 2.6 has been evaluated by means of Eq. (2.3). Pertaining to the other injector chambers, starting from the latter temperature, the instantaneous pressure difference between two adjacent chambers (namely $\Delta p_{dc \to up,s}$, $\Delta p_{up,s \to sac}$ and $\Delta p_{sac \to cyl}$ in Fig. 2.10) is calculated and used to evaluate the temperature rise by means of the isenthalpic hypothesis and, by using the correlation reported in Fig. 2.4, the real fuel temperature is estimated. If the isenthalpic temperature is not inside the range reported in Fig. 2.4, a linear extrapolation has been performed. In fact, based on a wide range of fuel temperature measured at the injector tip for different p_{nom} values [135], the correlation shown in Fig. 2.4 has been extended for both the T_{tank} fuel temperatures.

At the beginning and at the end of the injection event, the pressure drop $\Delta p_{sac \to cyl}$ is smaller than $\Delta p_{up,s \to sac}$ (cf. Fig. 2.10) because in those phases

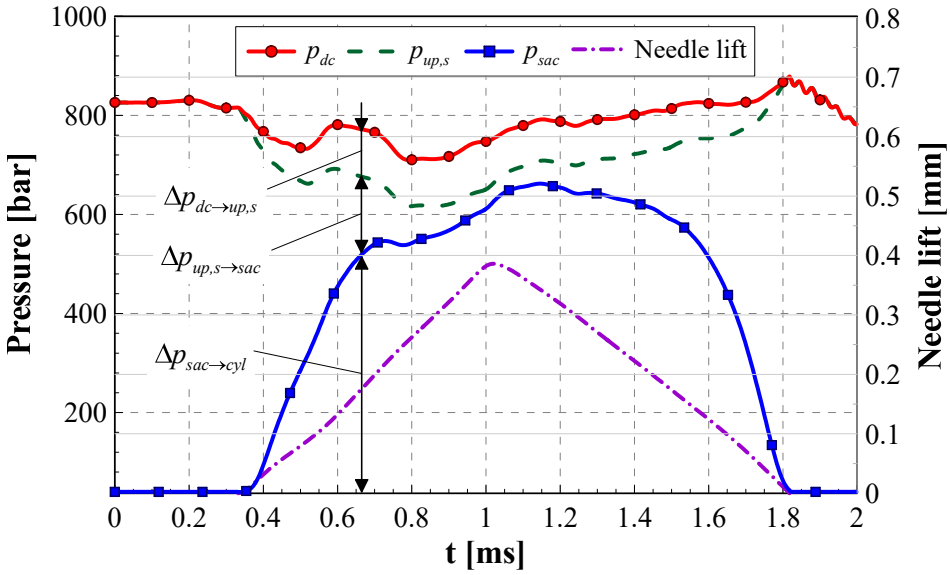

Figure 2.10: Pressure traces inside the injector and needle lift ($p_{nom} = 800$ bar, $ET = 1000$ µs and $T_{tank} = 40$ °C).

the restricted flow area is represented by the needle-seat passage. Therefore, the fuel temperature rise mainly occurs when the flow goes through the passage between the needle and its seat. If the time interval where the needle lift is sufficiently high is considered, the flow-rate results to be controlled by the nozzle holes. In this case, $\Delta p_{sac\rightarrow cyl}$ is much larger than $\Delta p_{up,s\rightarrow sac}$, hence the fuel temperature rise mainly occurs when the flow passes across the nozzle holes.

In Figs. 2.11 and 2.12, the numerical needle lift and injected flow-rate time histories are represented, for both the considered T_{tank} values, referring to $p_{nom} = 800$ bar, $ET = 800$ µs and to $p_{nom} = 1700$ bar, $ET = 600$ µs, respectively.

In general, when the fuel temperature rises the viscous force acting on the needle reduces due to the diminished fuel viscosity (the trend is exponential in Fig. 2.2). A reduced friction force leads to an augmented needle velocity in the opening phase when T_{tank} increases, hence an higher needle lift peak value for a fixed ET is reached. When the electrical current to the solenoid is switched off, the needle closure phase starts and the needle downstroke required to close the injector nozzle increases with the fuel temperature. This leads to a delayed nozzle closure and, consequently, an increased injection duration.

The fuel temperature effect results to be less obvious when a small ET value is considered, as is evident from Figs. 2.13 and 2.14. In fact, a short-ET

injection occurs with a small needle lift peak value and its absolute variation with respect to T_{tank} is slight. In conclusion, the fuel temperature effect becomes more evident when an injection with an high needle lift peak value is considered.

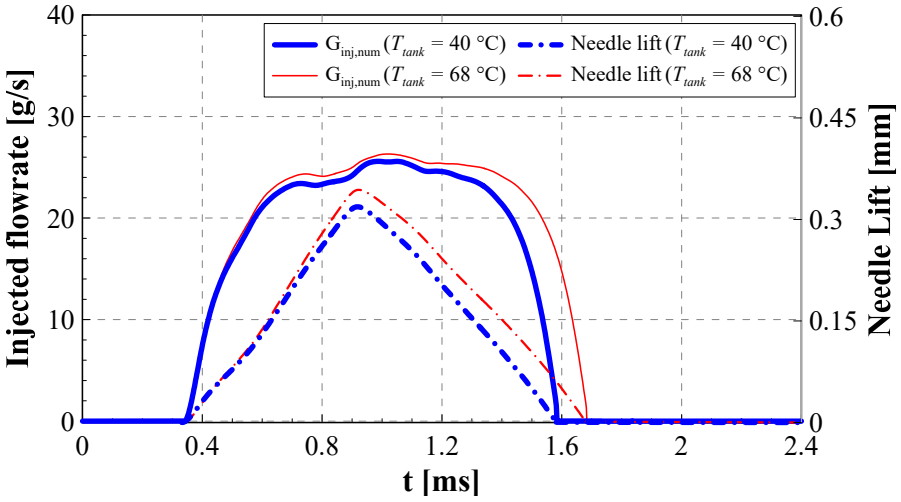

Figure 2.11: Injected flow-rate and needle lift numerical traces, with $T_{tank} = 40$ °C and $T_{tank} = 68$ °C ($p_{nom} = 800$ bar, $ET = 800$ µs).

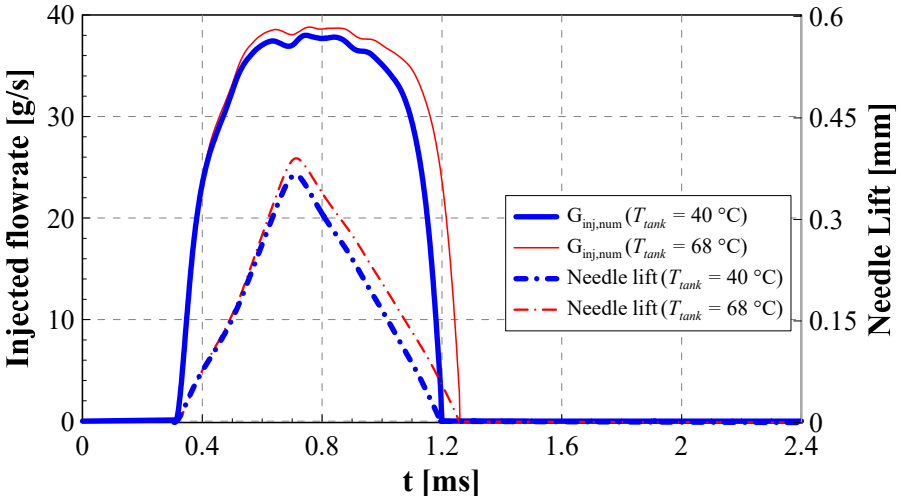

Figure 2.12: Injected flow-rate and needle lift numerical traces, with $T_{tank} = 40$ °C and $T_{tank} = 68$ °C ($p_{nom} = 1700$ bar, $ET = 600$ µs).

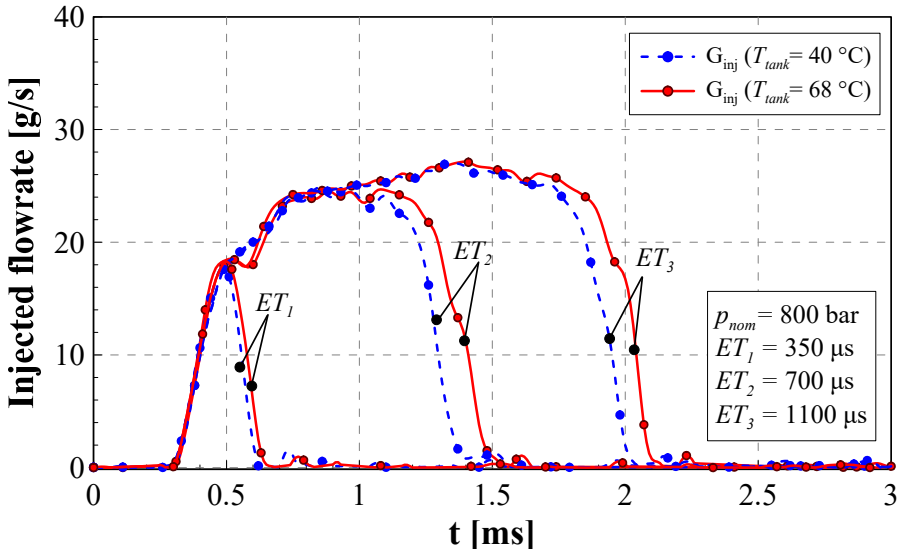

Figure 2.13: Injected flow-rate for different ET values, with $T_{tank} = 40$ °C and $T_{tank} = 68$ °C ($p_{nom} = 800$ bar).

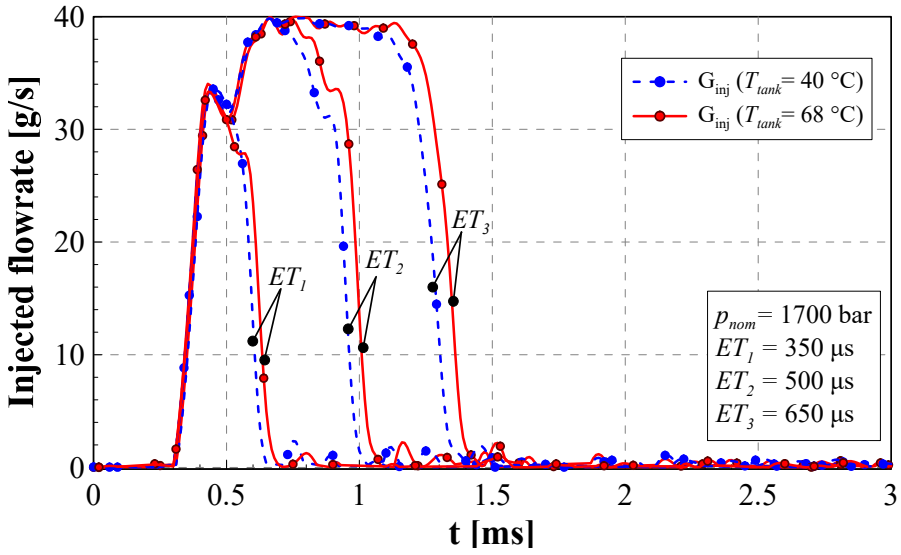

Figure 2.14: Injected flow-rate for different ET values, with $T_{tank} = 40$ °C and $T_{tank} = 68$ °C ($p_{nom} = 1700$ bar).

Chapter 3

Application of an innovative high-pressure flowmeter

3.1 Experimental setup

The experimental campaign has been carried out on an external gear pump installed on the hydraulic rig of the Fluid Power Research Laboratory of the Politecnico di Torino. A variable-speed electric motor has been adopted to drive the pump, that is inserted in a closed circuit. A photo of the pump is reported in Fig. 3.1.

The innovative high-pressure flow meter has been installed on the delivery pipe, a straight steel pipe with an internal diameter $d = 10$ mm. The flowmeter

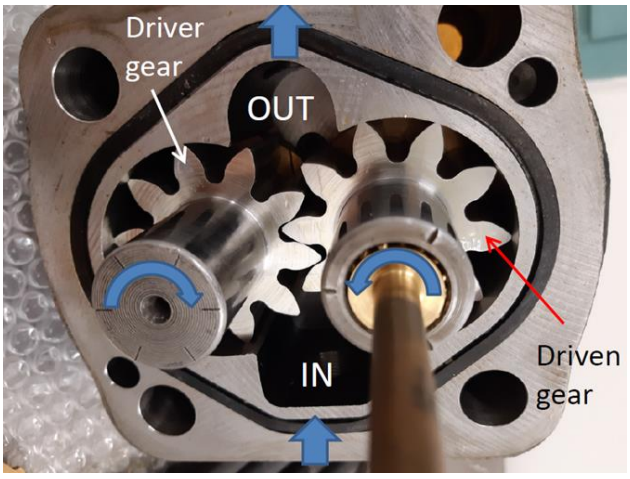

Figure 3.1: Photo of the considered gear pump.

consists in two GS XPM5 pressure transducers, labelled as P_1 and P_2 in Fig. 3.2. The distance between the two pressure transducers is $L = 450$ mm.

The transducers measure the pressure in the $0 - 200$ bar range, they are temperature-compensated between 0 °C and 60 °C. Their sensitivity is of 100 mV and the linearity error is lower than $\pm 0.25\%$ of the full scale. The GS XPM5 sensing element is a Wheatstone bridge with strain gauges. Before every test, when the system is not in pressure, the zero offset of the transducers has been adjusted in order to measure 0 bar. Therefore, it has been assumed that the only uncertainty contribution consists in the linearity error, that is lower than ± 0.5 bar.

The load in the delivery line has been generated by means of a calibrated orifice with 4 mm of diameter, drilled into a plate fixed between two flanges and mounted at the end of the steel pipe, downstream the transducer P_2 (cf. Fig. 3.2). A scheme of the delivery line (without the abovementioned load) is reported in Fig. 3.3.

A GS XPM5 pressure transducer has been mounted onto the pump casing to monitor the inlet volume pressure.

The ISO VG46 Mobil DTW 25 hydraulic oil has been used as the fluid in the circuit. All the tests have been performed with an oil temperature at the pump inlet of about 30 °C.

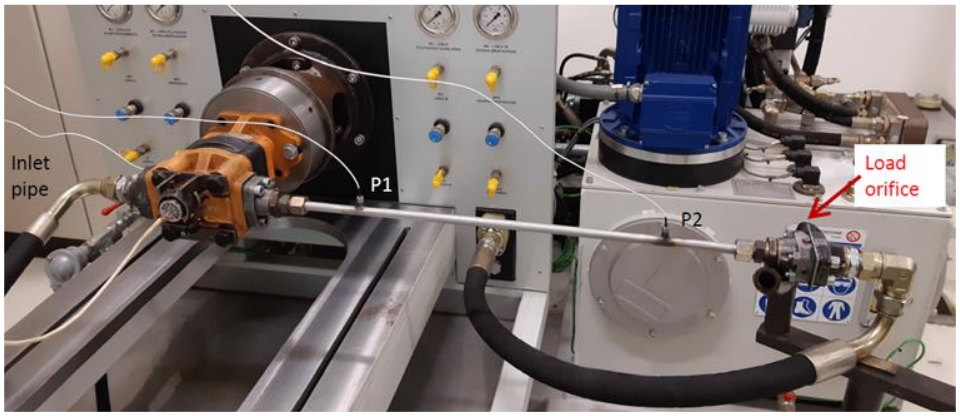

Figure 3.2: Photo of the test rig hydraulic circuit where the pump is mounted.

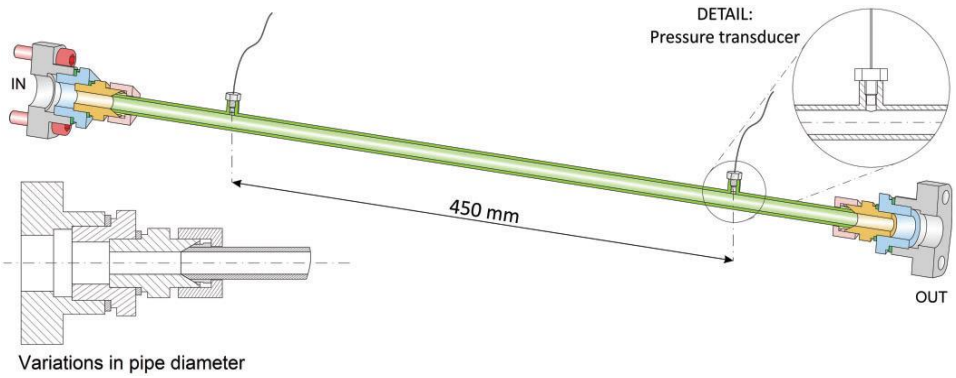

Figure 3.3: Schematic view of the pump delivery line.

3.2 Flowmeter algorithm

The flowmeter algorithm [92] is based on the mass conservation and momentum balance partial differential equations, written in one-dimensional form [43, 136]:

$$\begin{cases} \dfrac{d\rho}{dt} + \rho \dfrac{\partial u}{\partial x} = 0 \\ \dfrac{\partial u}{\partial t} + u \dfrac{\partial u}{\partial x} + \dfrac{1}{\rho} \dfrac{\partial p}{\partial x} = -\dfrac{4\tau_w}{\rho d} \end{cases} \tag{3.1}$$

where u represents the flow speed (averaged with respect to the pipe cross-section area), t is the time, x is the spatial coordinate (oriented along the pipe axis), ρ is the flow density, p the flow pressure and τ_w is the wall shear stress. By means of the incompressible flow assumption, one has that $d\rho/dt \approx 0$ and $\partial\rho/\partial x \approx 0$, hence, the system in Eq. (3.1) becomes:

$$\begin{cases} \dfrac{\partial u}{\partial x} = 0 \\ \dfrac{\partial u}{\partial t} + \dfrac{1}{\rho} \dfrac{\partial p}{\partial x} = -\dfrac{4\tau_w}{\rho d} \end{cases} \tag{3.2}$$

by multiplying the second relation in Eq. (3.2) by ρA (where $A = \pi d^2/4$ represents the pipe cross-section area) and by integrating over the length L and, finally, by dividing the results by the same length L, one has:

$$\frac{d\overline{G}}{dt} = \frac{A}{L}\Delta p - \pi d\overline{\tau}_w \tag{3.3}$$

where $\overline{G}$ stands for the space averaged mass flow-rate and Δp represents the instantaneous pressure difference measured by means of the transducers P_1 and P_2. The space averaged wall friction shear stress can be expressed by means of the Darcy-Weisbach steady-state stress term:

$$\overline{\tau}_w = \frac{\langle \overline{f} \rangle}{8\rho A^2} |\langle \overline{G} \rangle| \langle \overline{G} \rangle \tag{3.4}$$

where f represent the friction factor. Angular brackets ($\langle\ \rangle$) represent the time-averaged quantities (i.e., $\langle \overline{f} \rangle$ is the space- and time-averaged friction factor). Hence, by combining Eq. (3.3) and Eq. (3.4), one obtains:

$$\frac{d\overline{G}}{dt} = \frac{A}{L}\Delta p - \pi d \frac{\langle \overline{f} \rangle}{8\rho A^2} |\langle \overline{G} \rangle| \langle \overline{G} \rangle \tag{3.5}$$

which represents an ordinary integral-differential equation in terms of $\overline{G}$.

Eq. (3.5) can be integrated over an entire working cycle (characterized by the period T_p) and, by assuming an ideally periodic flow, one has [92]:

$$\frac{A}{L}\langle \Delta p \rangle = \pi d \frac{\langle \overline{f} \rangle}{8\rho A^2} |\langle \overline{G} \rangle| \langle \overline{G} \rangle \tag{3.6}$$

The instantaneous pressure difference is then expressed as a Fourier series [137]:

$$\Delta p(t) \approx \langle \Delta p \rangle + \sum_{k=1}^{N} \left[a_k \cos(\omega_k t) + b_k \sin(\omega_k t) \right] \tag{3.7}$$

where a_k and b_k (with $k \geq 1$) are the kth harmonic term coefficients, referring to the angular frequency $\omega_k = 2k\pi/T_p$, N is the wave number at which the 95% of the energy of Δp Fourier spectrum is included.

By substituting Eq. (3.7) into Eq. (3.5) and by taking into account Eq. (3.6), the instantaneous mass flow-rate fluctuations around the mean value can be obtained [92, 137]:

$$\Delta\overline{G} = \frac{A}{L} \sum_{k=1}^{N} \left\{ \frac{a_k}{\omega_k} \sin(\omega_k t) - \frac{b_k}{\omega_k} \cos(\omega_k t) \right\} \tag{3.8}$$

Obviously, the instantaneous volumetric flow-rate fluctuations are:

$$\Delta\overline{Q} = \frac{A}{\rho L}\sum_{k=1}^{N}\left\{\frac{a_k}{\omega_k}\sin(\omega_k t) - \frac{b_k}{\omega_k}\cos(\omega_k t)\right\} \tag{3.9}$$

In the considered case, the mean volumetric flow rate $\langle\overline{Q}\rangle$ can be measured by means of a low-pressure flowmeter or evaluated by knowing the pump displacement V_p, the selected pump speed n and the volumetric efficiency η_v. Hence, the instantaneous volumetric flow-rate is:

$$\overline{Q}(t) = \langle\overline{Q}\rangle + \Delta\overline{Q}(t) \tag{3.10}$$

3.3 Results

The gear pump and the delivery line were modelled with SimericsMP+v5.0, where the governing equations were discretized by means of a finite volume method. The pressure at the inlet port and downstream the load were selected as boundary conditions. Further details of the pump model can be found in [120].

The pressure time history measured by means of the transducer P_1 (cf. Fig. 3.2) has been compared with the numerical pressure obtained from the 3D numerical model, in correspondence of the sensor location. Three different working conditions have been selected and the corresponding results have been reported in Figs. 3.4-3.6, they refer to $n = 1000$ rpm and 45 bar (cf. Fig. 3.4), $n = 1500$ rpm and 95 bar (cf. Fig. 3.5) and $n = 1750$ rpm and 133 bar (cf. Fig. 3.6), respectively. For all the considered cases, the numerical outcomes match accurately the experimental traces and the model has been considered validated from the pressure point of view.

By means of the presented flowmeter, the high-pressure volumetric flow-rate in the delivery pipe can be measured and compared with the numerical one. The same working condition reported in Figs. 3.4-3.6 have been considered for the flow-rates and the comparisons are reported in Figs. 3.7-3.9. The results appear in satisfactory agreement and the accuracy of the flowmeter device has been further assessed.

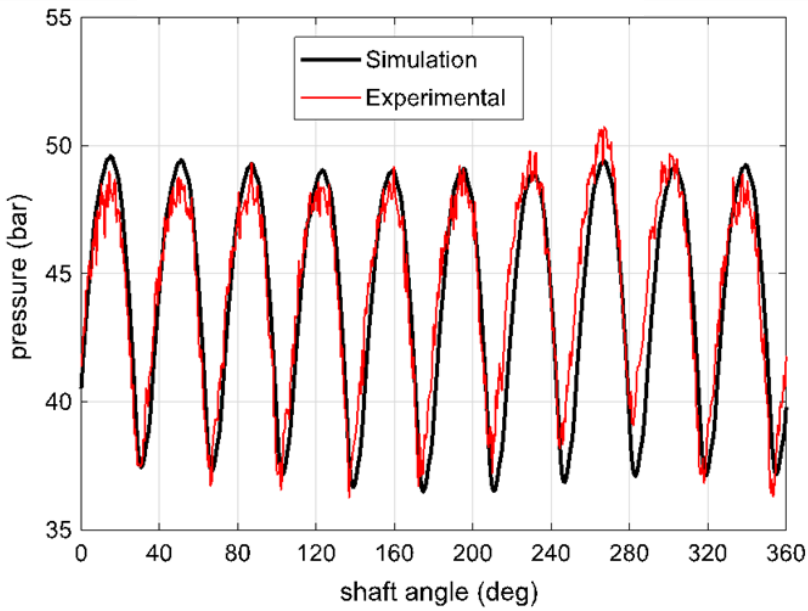

Figure 3.4: Comparison between the numerical and experimental pressure traces ($n = 1000$ rpm, 45 bar).

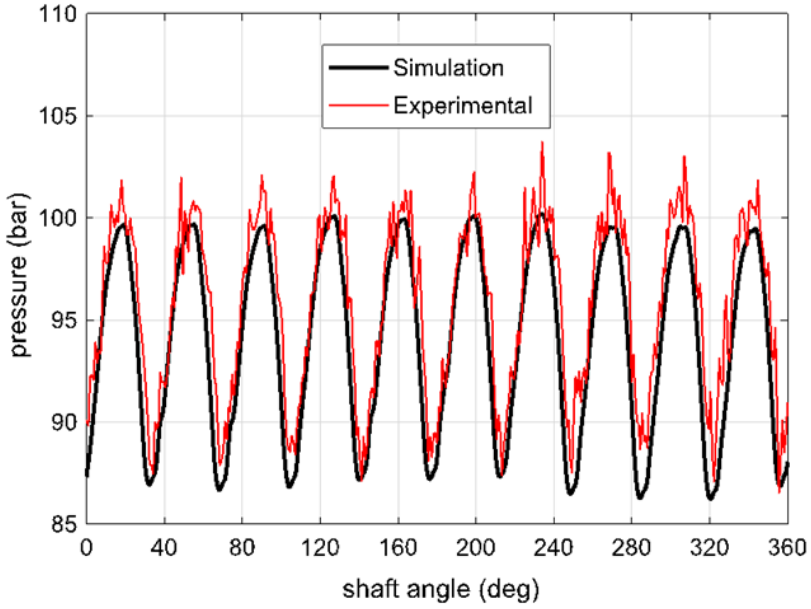

Figure 3.5: Comparison between the numerical and experimental pressure traces ($n = 1500$ rpm, 95 bar).

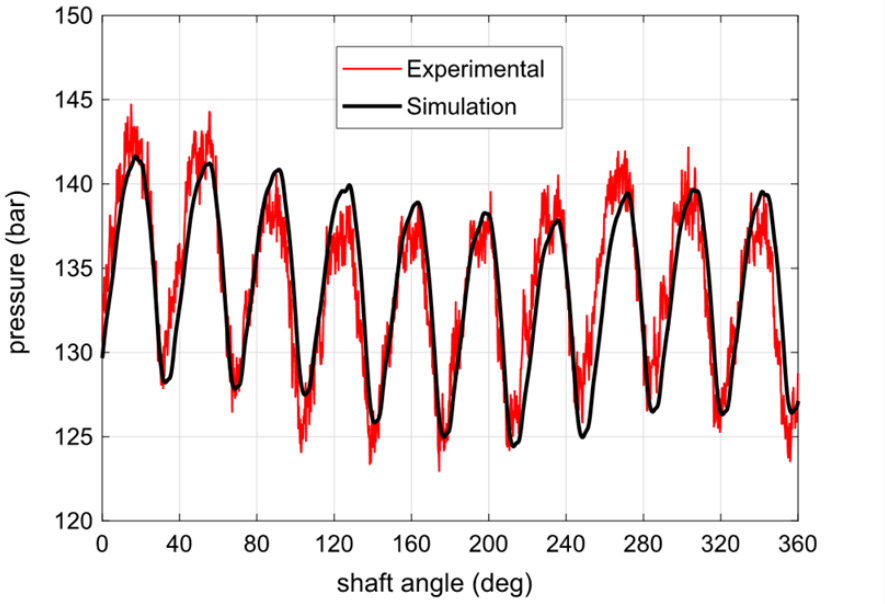

Figure 3.6: Comparison between the numerical and experimental pressure traces ($n = 1750$ rpm, 133 bar).

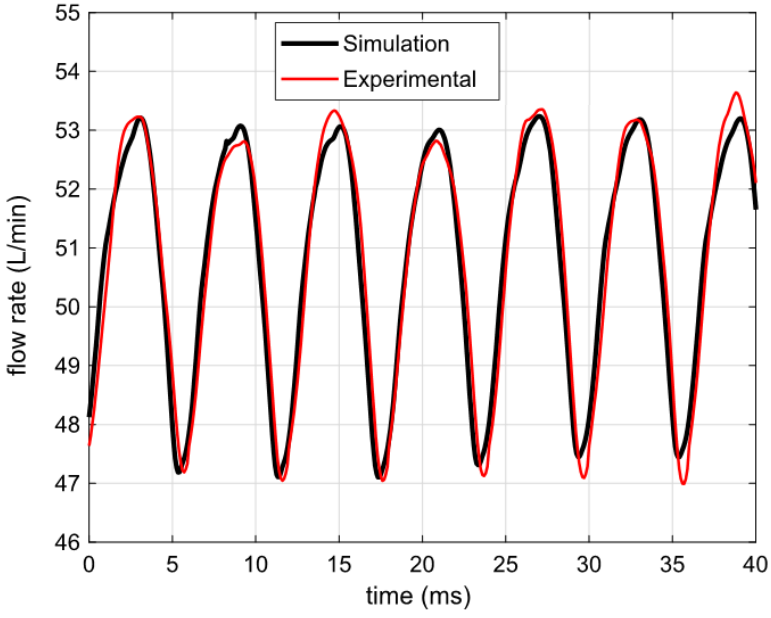

Figure 3.7: Comparison between the numerical and experimental flow-rates ($n = 1000$ rpm, 45 bar).

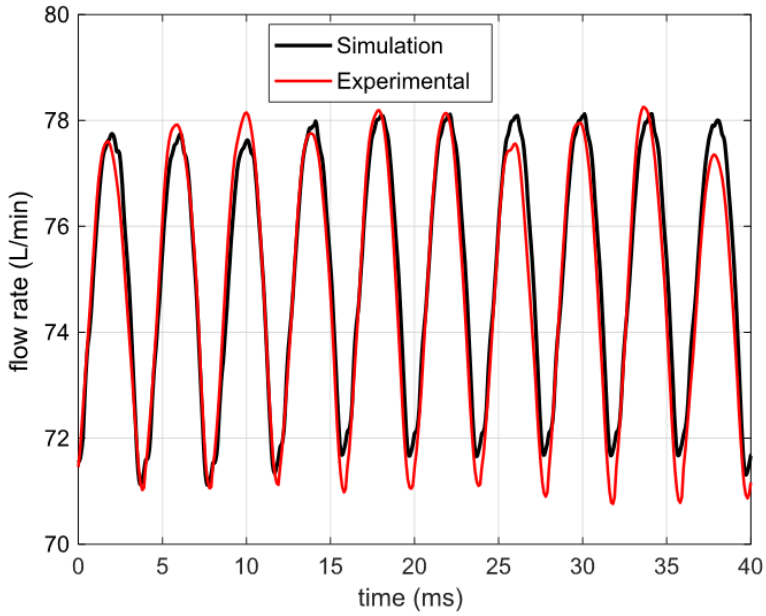

Figure 3.8: Comparison between the numerical and experimental flow-rates ($n = 1500$ rpm, 95 bar).

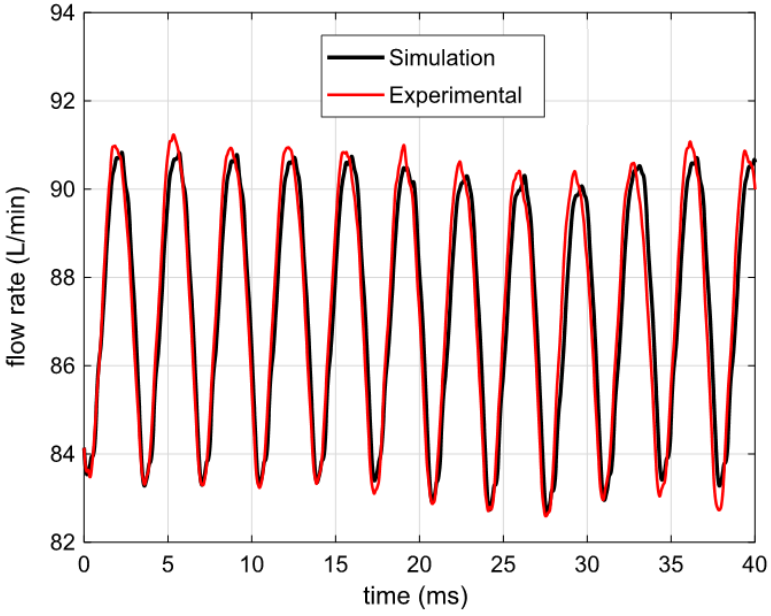

Figure 3.9: Comparison between the numerical and experimental flow-rates ($n = 1750$ rpm, 133 bar).

Chapter 4

Development of a closed-loop control strategy for the injected mass

4.1 Experimental setup

The experimental campaign has been carried out on the same hydraulic test rig already described in Sect. 2.1, Chap. 2, with the identical calibration fluid.

In this Chapter, two different solenoid-actuated injectors have been considered: a CRI 2.20 and a CRI 2.18, the scheme of the former is reported in Fig. 4.1 (cf. Fig. 2.1 for the CRI 2.18 scheme). Both the injectors are equipped with a pressure balanced pilot valve, but the CRI 2.20 injector features the presence of an integrated Minirail, whereas this is not present in the CRI 2.18 injector.

Pertaining to the CRI 2.20 working principle, it results to be very similar to the CRI 2.18 one, the main difference is that the fuel does not fill the delivery chamber, while this has been substituted by a minirail.

In Sect. 4.2, where the physical equations based technique is shown, two piezoresistive pressure transducers are installed along the rail-to-injector pipe and their signals are acquired by means of a PXI (from National Instruments) with a frequency of 500 kHz. Furthermore, the PXI performs necessary computations. The results of the calculations are sent to a FlexibleECU (by ETAS) which controls the injectors energizing currents and the duty cycles of the

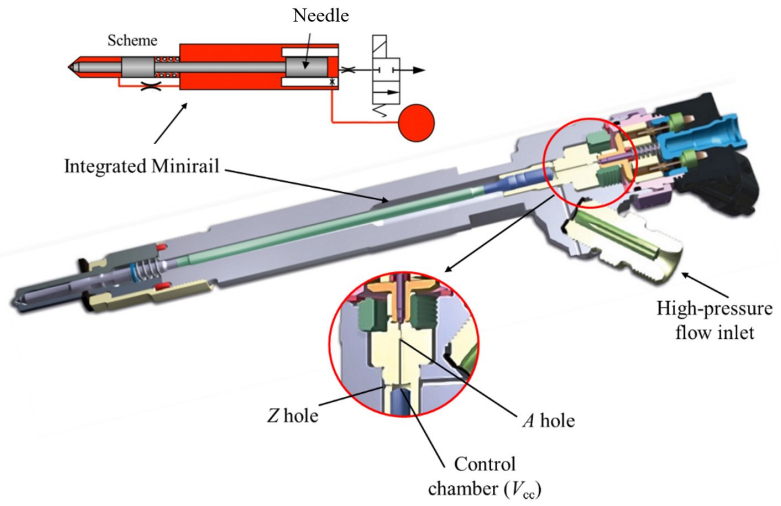

Figure 4.1: CRI 2.20 solenoid injector.

pressure control valve (PCV) and of the fuel metering valve (FMV) in the system. The experimental layout is represented in Fig. 4.2.

On the other hand, in Sect. 4.3, where the TFA-based technique is presented, only one piezoresistive pressure transducer is mounted along the monitored rail-to-injector pipe. The pressure time history is collected by means of the PXI. The correspondent experimental layout is reported in Fig. 4.3.

The whole experimental campaign presented in this Chapter has been performed at a fixed pump speed of 2000 rpm, corresponding to an engine speed of 2000 rpm. Since no obvious effects on the CR performance can be ascribed to the pump speed, the results can be generalized to other engine speeds.

4.2 Physical equations based technique

4.2.1 Control strategy and prototypal hardware

The entire ECU software has been developed by means of Matlab Simulink. It includes the standard control of the nominal rail pressure (p_{nom}) and the innovative control strategy for the ET correction, based on the real-time estimation of the injected mass. The scheme of the rapid prototyping hardware is reported in Fig. 4.4.

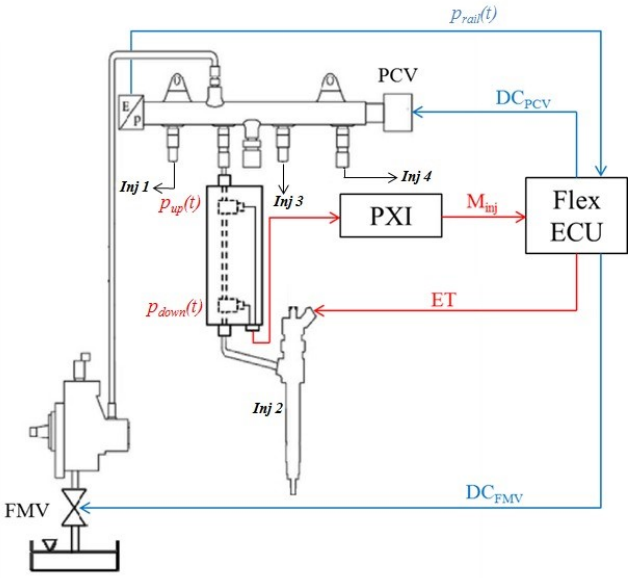

Figure 4.2: Experimental layout of the injection system for testing physical equations based method.

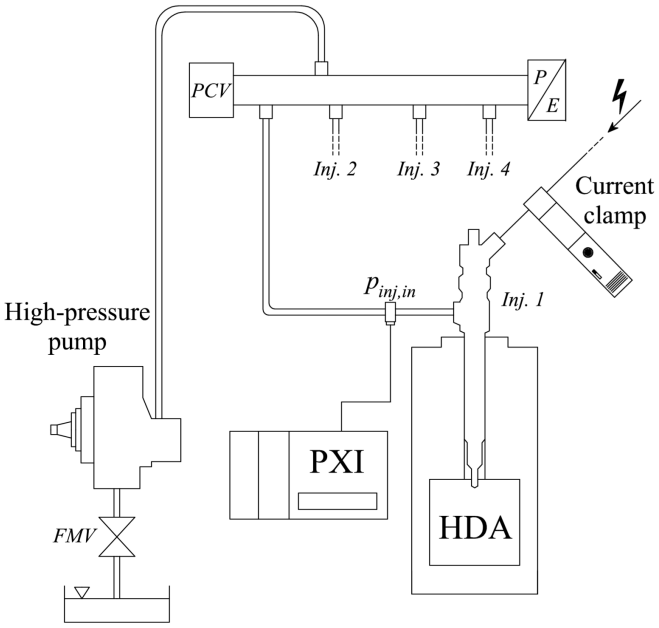

Figure 4.3: Experimental layout of the injection system for testing TFA based method.

The rail pressure level is measured, by means of a sensor, and filtered every 5 ms by the flexECU. The processed signal, namely $p_{filter}(t)$, is generated and compared with the set value of the p_{nom} (cf. H2 in Fig. 4.4). The difference

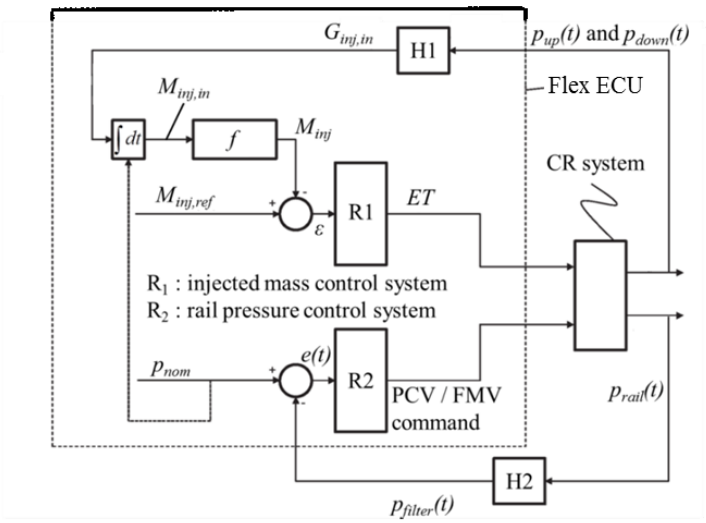

Figure 4.4: Injection system control strategies.

$e(t) = p_{nom} - p_{filter}(t)$ is obtained and used as an input of R2 in Fig. 4.4. This block contains a PID controller used to evaluate the duty cycle of the PCV or the FMV (DC_{PCV} and DC_{FMV} in Fig. 4.2). The former throttles the exceeding pumped fuel with respect to the ECU requirements, the latter modules the sucked up flow-rate in order to reach and mantain the desired pressure level (ideally, no fuel should be throttled at the pump delivery). Therefore, the block R2 represents the standard closed-loop control of the rail pressure level in a CR system.

The innovative control strategy is represented by the closed-loop control of the injected mass. The two pressure time histories measured along the rail-to-injector pipe, namely p_{up} and p_{down} (cf. Fig. 4.2), are used for the estimation of the injected mass (M_{inj}). If the nominal injected mass ($M_{inj,ref}$) required by the ECU is smaller than 5 mg, only the p_{down} pressure time history can be used in the M_{inj} estimation. In this particular case, the mass flow-rate entering the injector can be evaluated by means of the following expression [138]:

$$G_{inj,in} = -A \int_0^t \frac{dp_{down}}{a_s} \tag{4.1}$$

where A is the pipe internal cross-section area in which p_{down} is measured, and a_s represents the sound speed of the fluid.

On the contrary, if the $M_{inj,ref}$ is larger than 5 mg or a pilot-main injection is taken into account, the $G_{inj,in}$ is obtained by means of the following equation, where both p_{up} and p_{down} are used [92]:

$$G_{inj,in} = \frac{A}{L}\int_0^t \Delta p dt - \frac{A}{L}\langle \Delta p \rangle \cdot t \tag{4.2}$$

where $\Delta\, p\, =\, p_{up}\, -\, p_{down}$, L represents the distance between the two pressure sensors and $\langle \Delta p \rangle$ is the time average of Δp over an entire injection cycle. As can be noticed, Eq. (4.2) results to be the working principle of the high-pressure flowmeter described in Chap. 3, Sect. 3.2. Both Eqs. (4.1) and (4.2) refer to the block H1 in Fig. 4.4. In order to obtain the mass at the injector inlet, the obtained instantaneous mass flow-rate $G_{inj,in}$ is integrated over the time between two optimized instants, namely t_i and t_f:

$$M_{inj,in} = \int_{t_i}^{t_f} G_{inj,in} dt \tag{4.3}$$

As reported in Fig. 4.5, in both the cases the t_i corresponds to the time instant at which the energizing current starts to rise ($t_i = 0$), meanwhile t_f virtually coincides with the instant where the maximum of the $G_{inj,in}$ occurs. The pressure waves triggered by the injections travel forth and back along the rail-to-injector pipe and, locally, negative flow-rates can be figured out in Fig. 4.5. These reverse flows do not contribute in the calculation of the integral presented in Eq. (4.3) because they occur after t_f.

It has been seen that the $M_{inj,in}$ is well correlated with the injected mass M_{inj}, on the basis of the mass conservation equation. Figure 4.6 reports M_{inj} as a function of $M_{inj,in}$ for both single and pilot-main injections. The one pertaining to single injections have been divided into small, medium and large injected masses, while for the pilot-main injections only one correlation is considered.

Figure 4.6a represents the piecewise linear interpolating lines for single injections, whereas the one for pilot-main injections is shown in Fig. 4.6b. These lines represent a linear mathematical law $M_{inj} = f(M_{inj,in})$, and their application allow the estimation of M_{inj} by means of $M_{inj,in}$ measurement in the real time system operations.

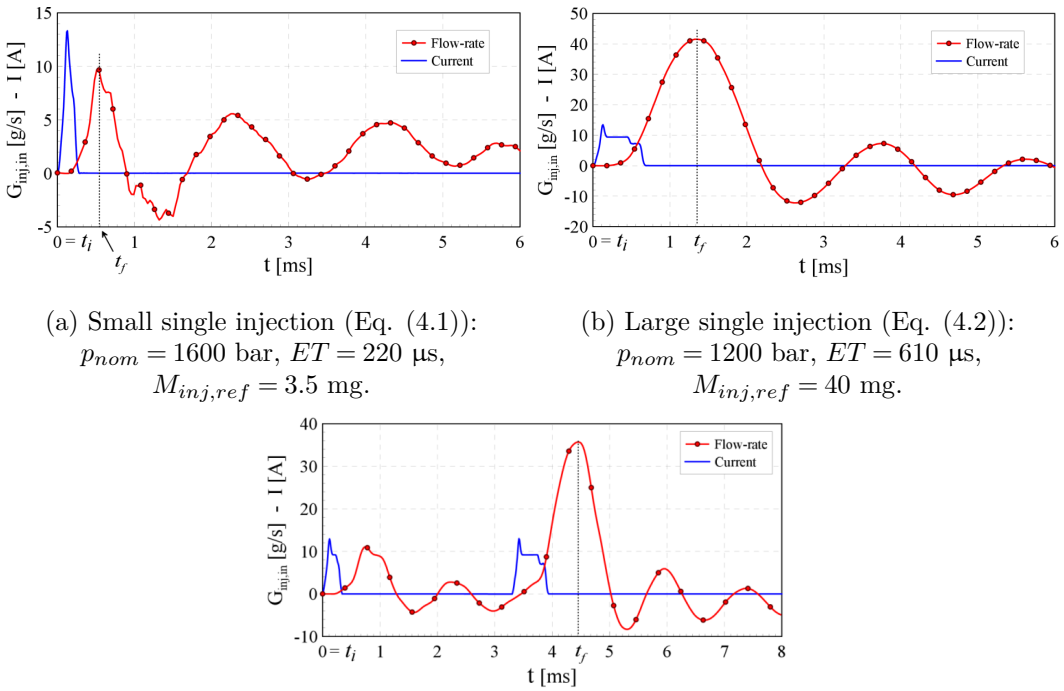

(a) Small single injection (Eq. (4.1)): $p_{nom} = 1600$ bar, $ET = 220$ µs, $M_{inj,ref} = 3.5$ mg.

(b) Large single injection (Eq. (4.2)): $p_{nom} = 1200$ bar, $ET = 610$ µs, $M_{inj,ref} = 40$ mg.

(c) Pilot-main injection (Eq. (4.2)): $p_{nom} = 1600$ bar, $ET_{pil} = 270$ µs, $ET_{main} = 570$ µs, $DT = 3000$ µs.

Figure 4.5: Instantaneous mass flow-rates at the injector inlet.

The difference ε between the desired injected mass $M_{inj,ref}$, stored in the ECU maps, and the estimated injected mass M_{inj}, is evaluated as $\varepsilon = M_{inj,ref} - M_{inj}$ and used as an input for a PID controller implemented in the block R1 in Fig. 4.4. The output from R1 consists in the modified ET supplied to the injector in order to correct the injected mass error during the next engine cycle.

Eqs. (4.1)-(4.3) and the $M_{inj} = f(M_{inj,in})$ correlations have been implemented in the PXI device (cf. Fig. 4.2), which recieves as inputs the p_{up} and the p_{down} signals. The injected mass estimation M_{inj} is delivered through a CAN interface cable from the PXI to the Flexible ECU, and the Flexible ECU generates the corrected energizing time to the injector, based on the ε value.

The control strategy has been implemented in the Flexible ECU by means of the ETAS EHOOKS software. Generally, a CR system software can be divided in two parts: a basic software, normally provided by the injection system manufacturer, in which all the basic variables are defined; the application software, where the p_{nom} and ET control strategies are implemented. The role

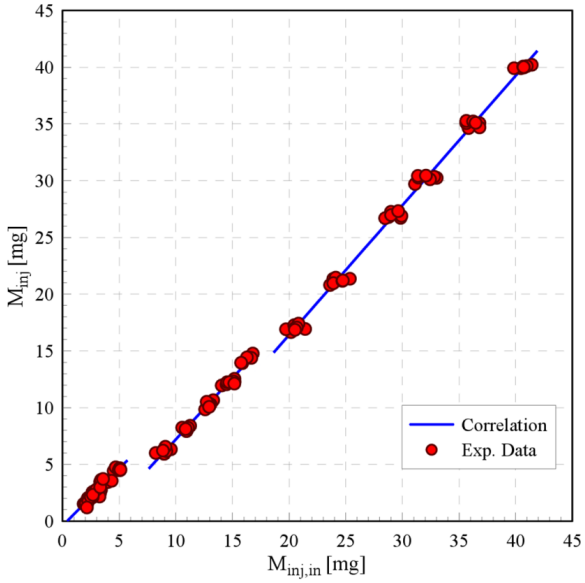

(a) Single injections

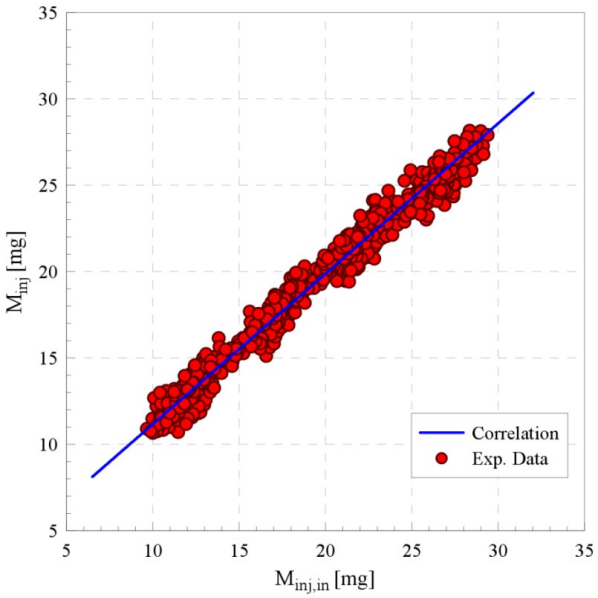

(b) Pilot-main injections

Figure 4.6: Correlation between the $M_{inj,in}$ and the M_{inj}.

of the EHOOKS tool consists in the merging of these two software in order to generate a single software package, which is flashed in the Flexible ECU memory.

4.2.2 Results for single injections

All the results reported in this Section are referred to the CRI 2.20 solenoid injector.

For each working condition, the effective injected fuel mass M_{inj} has been measured, for fixed p_{nom} and $M_{inj,ref}$, by means of the HDA, as an average of 100 consecutive engine cycles. During the tests, the rail pressure was controlled by means of the FMV. The accuracy on the injected mass, defined as $|\Delta M_{inj}| = |M_{inj,ref} - M_{inj}|$, is reported in the 3D diagram in Fig. 4.7 as a function of $M_{inj,ref}$ and p_{nom}. The injected mass M_{inj}, obtained by using both the standard open-loop control strategy and the innovative Polito closed-loop one [139] under the condition of $T_{tank} = 40$ °C, have been reported in Figs. 4.7a and 4.7b, respectively. Furthermore, the same working conditions have been investigated for $T_{tank} = 68$ °C and the results are shown in Fig. 4.8.

As can be seen, the injected mass accuracy improves for both Figs. 4.7 and 4.8 when the new closed-loop control strategy is acting. In this case, the

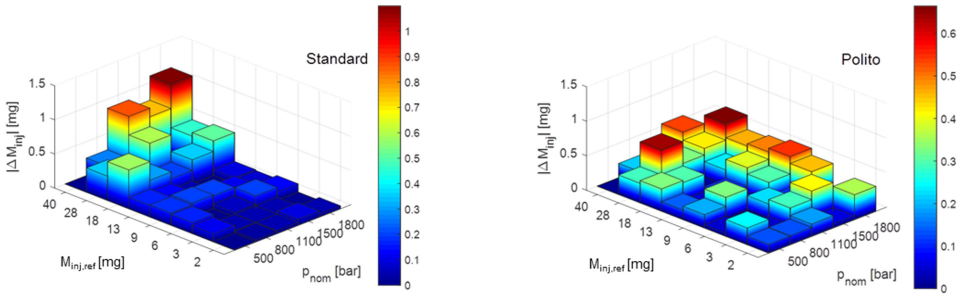

(a) Standard control strategy (b) Polito control strategy

Figure 4.7: Accuracy on M_{inj} related to different control strategies ($T_{tank} = 40$ °C).

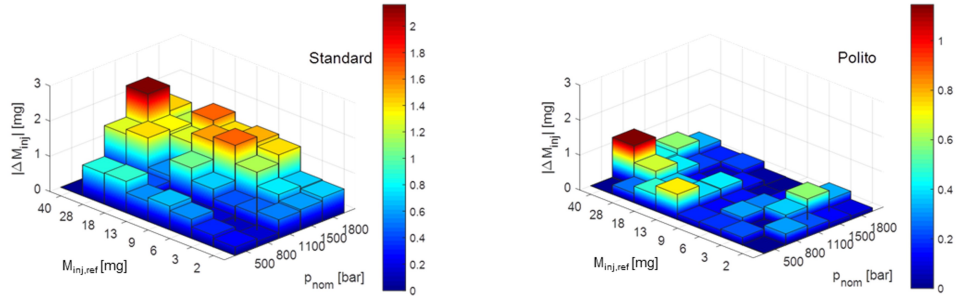

(a) Standard control strategy (b) Polito control strategy

Figure 4.8: Accuracy on M_{inj} related to different control strategies ($T_{tank} = 68$ °C).

maximum error $|\Delta M_{inj}|$ is below 0.55 mg in Fig. 4.7b and is around 1 mg for the higher fuel tank temperature, in Fig. 4.8b. Concerning to the standard open-loop strategy, the maximum error is above 1 mg in Fig. 4.7a and is greater than 2 mg in Fig. 4.8b.

The presented closed-loop control strategy possesses a very satisfactory performance over the complete explored working conditions. Moreover, the improvements are more evident when T_{tank} increases from 40 ℃ to 68 ℃. Furthermore, p_{nom} and $M_{inj,ref}$ exert a more evident effect on $|\Delta M_{inj}|$ in the standard open-loop strategy than in the innovative one. In fact, the standard system exhibits an evident deterioration in the error $|\Delta M_{inj}|$ when the fuel tank temperature, p_{nom} and $M_{inj,ref}$ increase ($|\Delta M_{inj}| \approx 1.5 - 2.2$ mg).

Fig. 4.9 shows $|\Delta M_{inj}|$ values obtained with the two systems for some particular operating conditions included in Figs. 4.7 and 4.8. As can be observed, the CRI 2.20 injector presents higher value of the injected mass when $T_{tank} = 68$ ℃ and the standard control is acting, especially for augmented p_{nom} and $M_{inj,ref}$, in accordance to Chap. 2.

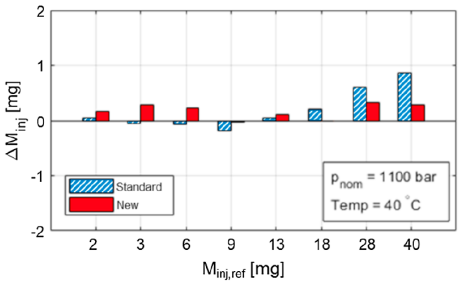

(a) $p_{nom} = 1100$ bar and $T_{tank} = 40$ ℃

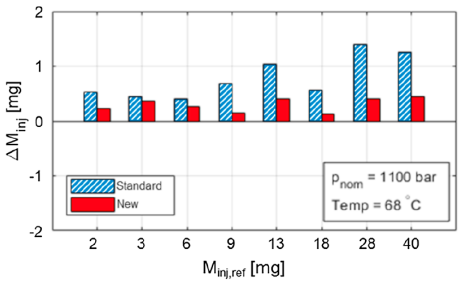

(b) $p_{nom} = 1100$ bar and $T_{tank} = 68$ ℃

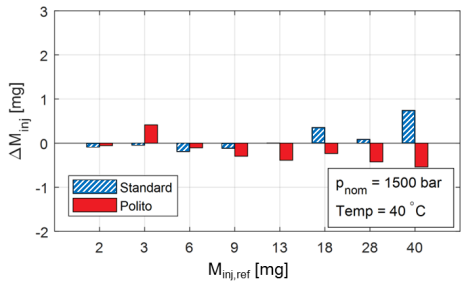

(c) $p_{nom} = 1500$ bar and $T_{tank} = 40$ ℃

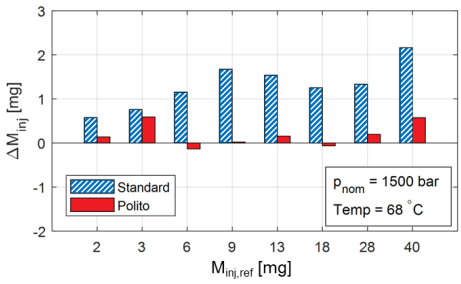

(d) $p_{nom} = 1500$ bar and $T_{tank} = 68$ ℃

Figure 4.9: Comparison of the ΔM_{inj} performance for different p_{nom} and T_{tank} values.

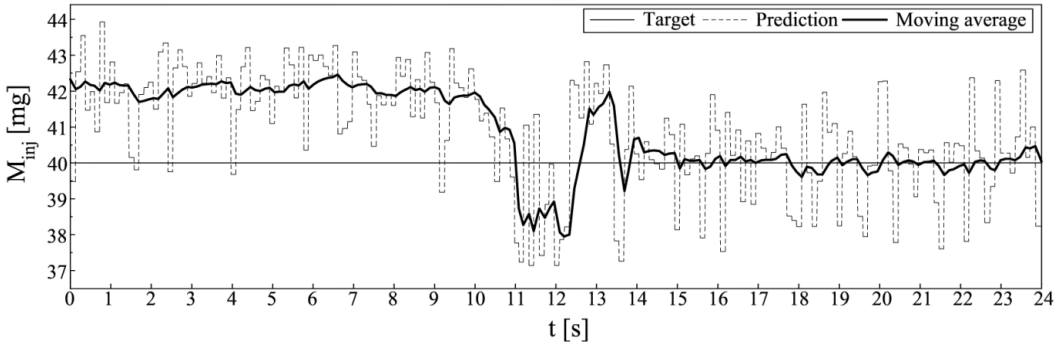

Figure 4.10: Performance of the estimated M_{inj} when the closed-loop strategy is activated ($p_{nom} = 1600$ bar, $T_{tank} = 68$ ℃ and $M_{inj,ref} = 40$ mg).

The dynamic behaviour of the innovative control strategy is shown in Fig. 4.10, where $p_{nom} = 1600$ bar, $T_{tank} = 68$ ℃ and $M_{inj,ref} = 40$ mg. The dashed curve represents the injected quantity estimation per shot as a function of time, while the continuous thick curve refers to the moving average of the dashed curve. Finally, the thin continuous line is the injected mass target. The moving average results to be evidently closer to the target when the Polito system is acting (right part in Fig. 4.10), than for the standard one (left part in Fig. 4.10). When the innovative closed loop control is activated ($t \approx 10$ s), in Fig. 4.10 it is evident that the thick curve approaches the target line, leading to a reduction of the ΔM_{inj} error.

The commercial injector, working with the standard open-loop control, is designed to reach optimum performance for a certain T_{tank} value and with an injected mass of low to medium value. In fact, for $T_{tank} = 40$ ℃ and $M_{inj,ref} \leq 15$ mg, the accuracy reported in Figs. 4.7a, 4.8a and 4.9 for the standard control is very satisfactory.

The CRI 2.20 accuracy on M_{inj}, without the innovative control strategy, generally worsen as the fuel temperature at the nozzle (obviously related to the T_{tank} value) increases with respect to the working condition assumed as the "design" one, as has been explained in Sect. 2.5, Chapt. 2. Furthermore, an augmented final temperature of the injected fuel is experienced for higher p_{nom} or $M_{inj,ref}$, due to the increased intensity or the fuel amount throttled along the injector. The new developed control strategy results to be sensitive to the fuel temperature effect inside the injector. As this temperature rises, leading to an increased injected mass compared to the nominal fuel temperature case,

the mass at the injector inlet $M_{inj,in}$ also grows and this phenomena can be detected by the ECU. The presented correlation $M_{inj,in} - M_{inj}$ in Fig. 4.6 results to be independent of the fuel temperature over 28 ℃ $< T_{tank} <$ 68 ℃.

The disturbance caused by the fuel temperature variations on the injection performance is a well-known problem for the engine calibration, taken into account by means of different calibration maps used at the engine dynamometer cell with respect to the one used at the hydraulic rig. These maps represent ECU lookup tables that provide a relation between $M_{inj,ref}$, ET and p_{nom}.

Table 4.1 shows the injected mass measured at the hydraulic test bench ($T_{tank} = 40$ ℃) with the open-loop control strategy based on the $M_{inj,ref} = f(p_{nom}, ET)$ lookup table calibrated at the dynamometer cell. It can be seen that the error between the target value (first row of the table) and the measured injected quantity increases with either p_{nom} or $M_{inj,ref}$, reaching approximately 9.5 mg. The injection system equipped with the standard control strategy has been observed, under such condition, to inject less fuel than the target. In fact, for a fixed couple of ET and p_{nom}, the injected mass augments with the fuel temperature in the nozzle and the selected calibration is adjusted to reach the best performance (in terms of accuracy of the injected mass) at the dynamometer cell, where higher temperatures than the ones at the hydraulic rig can be experienced. The data presented in Tab. 4.1 are in line with the results of Fig. 4.9 with $T_{tank} = 68$ ℃. Even though, values of $|\Delta M_{inj}|$ result to be bigger in Tab. 4.1 than the ones in Fig. 4.9 and it can be ascribed to the more higher nozzle temperature at the dynamometer cell than the one that occurs at the hydraulic rig with the maximum T_{tank}. Hence, it is expected that an implementation of the closed-loop control strategy of the injected mass

Table 4.1: Injected mass measured at the hydraulic test bench with the lookup table calibrated at the dynamometer cell.

p_{nom} [bar]	2 mg	3 mg	6 mg	9 mg	13 mg	18 mg	28 mg	40 mg
500	1	1.9	4.3	6.5	10.3	14.5	23.6	35.5
800	0.8	1.4	4.4	6.8	9.9	13.9	23.6	34.7
1100	0.7	1.3	3.3	5.3	9.2	13	22.1	33.8
1500	0.5	1.2	2.6	3.9	6.5	11.6	20.8	32.3
1800	0.3	1	2.8	4.1	5.7	10.1	20.7	31.4

acting on an engine provides more significant benefits than those observed at the hydraulic test rig.

It must be noticed that it is difficult to obtain an accurate open-loop compensation of the injected mass as a function of the engine thermal regime, in fact the fuel temperature at the nozzle is also affected by the recent history of the load and speed of the engine. Such a history results to be variable and a precise compensative open-loop strategy is problematic to be built on the basis of the engine working point and on the engine cooling water temperature.

Fig. 4.11 reports the standard deviation of the injected mass evaluated by means of the HDA flowmeter over 100 consecutive engine cycles at a fixed working condition in terms of p_{nom}, $M_{inj,ref}$ and engine speed n (p_{nom} = 1100 bar or p_{nom} = 1500 bar and n=2000 rpm) for both T_{tank} = 40 °C and T_{tank} = 68 °C. As can be seen, the closed-loop control for the injected mass (Polito system) guarantees a repeatability comparable with the standard system for the CRI 2.20 injector. In fact, severe tolerances are adopted in the manufacturing of the CRI 2.20 injector, where the presence of the Minirail provides an enhanced stability of the injected mass by reducing the cycle-to-cycle dispersion. Therefore, it is very challenging to improve such results and, as can be inferred

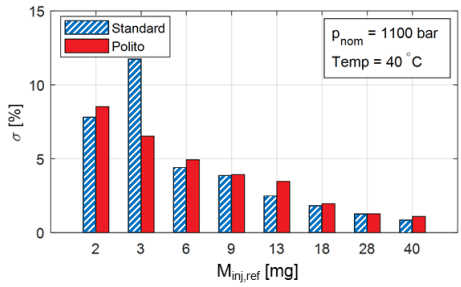

(a) p_{nom} = 1100 bar and T_{tank} = 40 °C

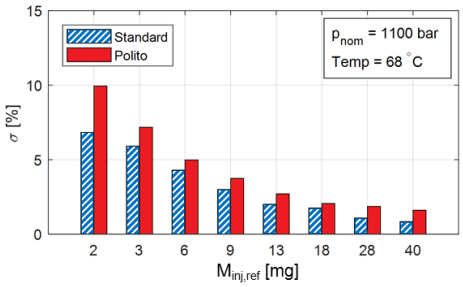

(b) p_{nom} = 1100 bar and T_{tank} = 68 °C

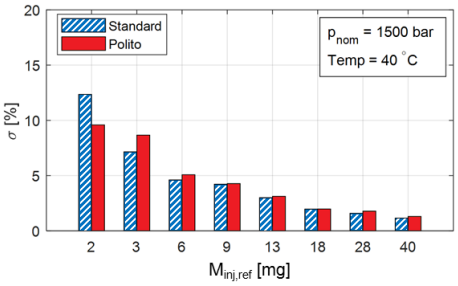

(c) p_{nom} = 1500 bar and T_{tank} = 40 °C

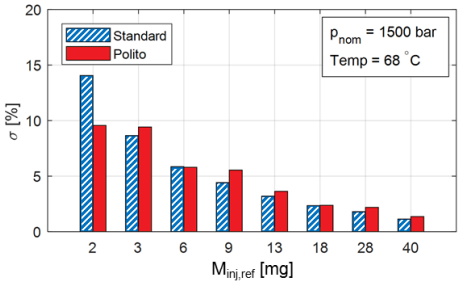

(d) p_{nom} = 1500 bar and T_{tank} = 68 °C

Figure 4.11: Standard deviation in the M_{inj} for different p_{nom} and T_{tank} values.

in Fig. 4.11, no evident enhancement in the injected mass precision are obtained with the closed-loop control strategy.

Further tests have been performed to assess the dynamic response of the developed control. In Fig. 4.12 is reported the results pertaining to a step-change in terms of $M_{inj,ref}$ and p_{nom}, for both $T_{tank} = 40$ °C and $T_{tank} = 68$ °C, at constant speed. As can be observed, the closed-loop control strategy is able to achieve a better dynamic performance with respect to the standard one. Both the systems reach the new target of injected mass, however, the Polito control strategy achieves an enhanced accuracy. Furthermore, Fig. 4.13 shows results in accordance to the ones presented in Fig. 4.12 also when ramps in $M_{inj,ref}$ and p_{nom} are performed.

From the results in Figs. 4.12 and 4.13 can be inferred that the innovative control strategy is able to manage variable targets in terms of pressure and

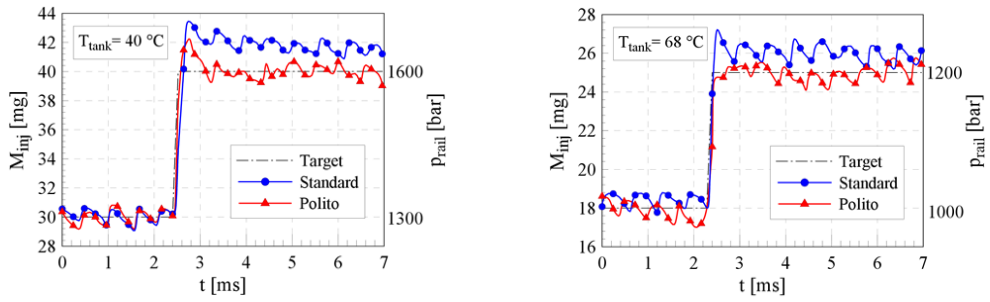

(a) $T_{tank} = 40$ °C (b) $T_{tank} = 68$ °C

Figure 4.12: Dynamic response to steps in p_{nom} and $M_{inj,ref}$ values.

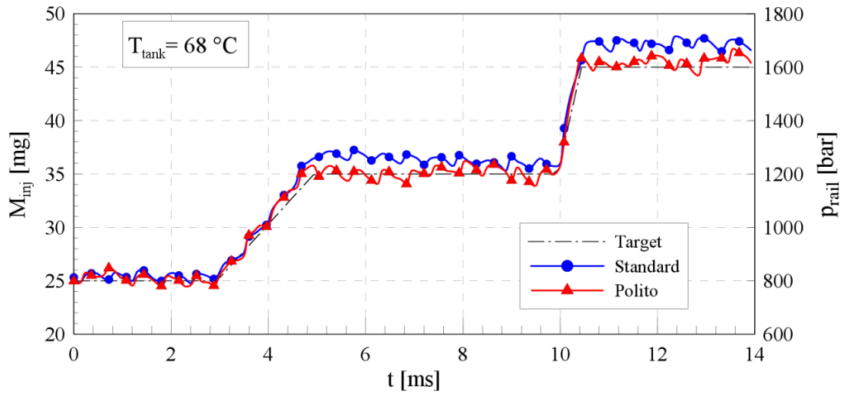

Figure 4.13: Dynamic response to ramps in p_{nom} and $M_{inj,ref}$ values.

target mass with an augmented accuracy. This characteristic may lead to an improvement in the engine performance during emission cycles featuring significant transient phases.

4.2.3 Results for pilot-main injections

As far as the pilot-main injections are concerned, the CRI 2.18 injector has been applied. Curves reported in Fig. 4.14 shows the overall injected mass as a function of the dwell time (DT) obtained with the standard control strategy. Hence, ET_{pil} and ET_{main} are fixed for each pressure level (they are established by setting $DT = 3000$ µs to fulfil the $M_{inj,ref}$ requirement and kept constant for the entire DT sweep). It can be observed that $M_{inj} = M_{pil} + M_{main}$ monotonically grows as the DT is reduced below 400 µs. This anomalous increment in the injected mass, compared to the target mass $M_{inj,ref} = M_{pil,ref} + M_{main,ref}$ (dashed-dotted lines in Fig. 4.14), is due to the hydraulic interference caused by the pilot injection on the main one [140]. A similar trend can also be obtained for the CRI 2.20 injectors, not reported for conciseness reasons.

The pilot interfering action exerted on the main injection is not only indirect, namely the triggered pressure waves (these are the main cause of the fluctuation of the injected mass around the target for medium and high values of DT), in fact it directly affects the internal hydraulic and the mechanical transients experienced by the injector [46, 141]. This direct interference culminates with

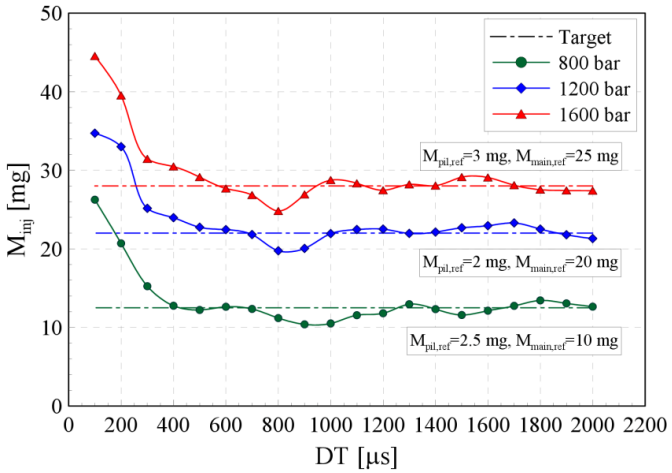

Figure 4.14: Pilot-main injected mass as a function of p_{nom} and DT with the standard system.

the fusion of the two injection events for DT smaller than the injection fusion threshold.

The M_{inj} results to be very sensitive to small changes in DT, due to the needle lift cycle-to-cycle dispersion pertaining to a pilot-main injection. Even though this effect on the injected mass can be still acceptable at the hydraulic test bench [46], consequences get dramatic on the engine, where an anomalous variation on the indicated mean effective pressure can be noticed.

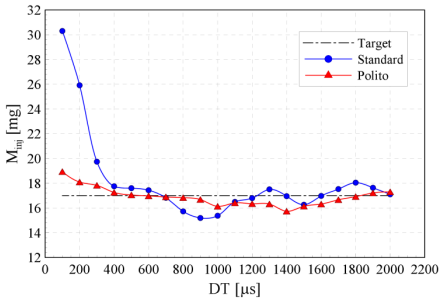

(a) $p_{nom} = 800$ bar, $M_{pil,ref} = 2$ mg, $M_{main,ref} = 15$ mg

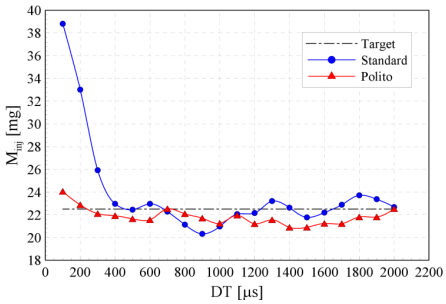

(b) $p_{nom} = 800$ bar, $M_{pil,ref} = 2.5$ mg, $M_{main,ref} = 20$ mg

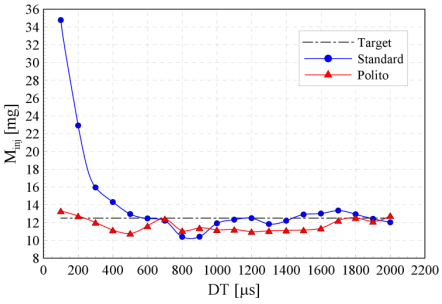

(c) $p_{nom} = 1200$ bar, $M_{pil,ref} = 2.5$ mg, $M_{main,ref} = 10$ mg

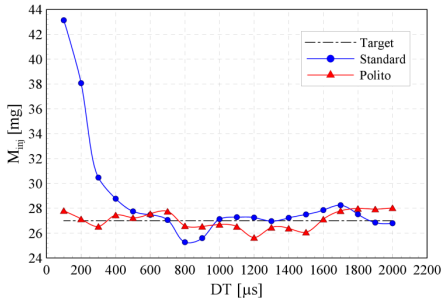

(d) $p_{nom} = 1200$ bar, $M_{pil,ref} = 2$ mg, $M_{main,ref} = 25$ mg

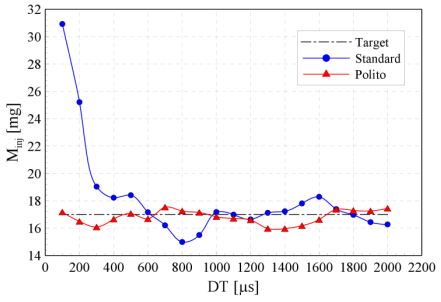

(e) $p_{nom} = 1600$ bar, $M_{pil,ref} = 2$ mg, $M_{main,ref} = 15$ mg

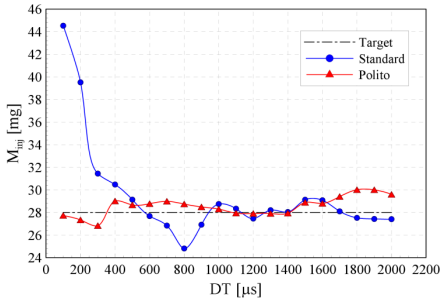

(f) $p_{nom} = 1600$ bar, $M_{pil,ref} = 3$ mg, $M_{main,ref} = 25$ mg

Figure 4.15: Pilot-main injections DT sweeps.

A part of the DT sweeps from the full investigation (in terms of $M_{pil,ref}$, $M_{main,ref}$ and p_{nom} values) is reported in Fig. 4.15, under the condition of $T_{tank} = 40$ ℃. The injected fuel quantity M_{inj} has been measured as an average of 100 consecutive cycles by means of the HDA flowmeter, the rail pressure level was controlled, for all the test, through the FMV.

The closed-loop control is able to significantly improve the injected mass accuracy (the error with respect to the target is below 2 mg) over the whole DT range. Furthermore, the anomalous increment of the injected mass for $DT < 400$ µs vanishes, while it is evident in all the cases where the standard open-loop strategy for the injected mass is acting. In conclusion, the innovative closed-loop strategy could be used on a commercial CR system to drastically reduced the indicated mean effective pressure dispersion occurring in engine tests characterized by small values of DT.

4.3 TFA based technique

4.3.1 Time-frequency analysis

The TFA allows to study a signal in both the time and the frequency domain in order to show the frequency spectrum variations of the considered signal $f(t)$. In this Section, one focuses on the time instants pertaining to the nozzle opening and closure. A high number of fast Fourier transforms (FFT) are carried out over consecutive, overlapping, short-time ranges, and every FFT is referred to the mean time instant of the considered interval. It is assumed that the analysed non-stationary signal refers to a steady-state condition within every time interval, therefore a local frequency spectrum is obtained. In other words, a windowing of the signal $f(t)$ is performed: the signal is multiplied by a certain window function $h_w(t-\eta)$, which is of unit energy and it is higher than zero only around the time instant η. The short-time Fourier transform (STFT) is then evaluated as follows:

$$F(\nu,\tau) = \int_{-\infty}^{+\infty} f(t) \cdot h_w(t-\eta) e^{-j2\pi\nu t} dt \tag{4.4}$$

Since the window function does not affect the signal energy, the energy density spectrum P_f can be evaluated:

$$P_f(\nu,t) = |F(\nu,t)|^2 \tag{4.5}$$

Hence, E_f, namely the energy of signal f, is obtained by means of the following relation:

$$E_f = \int_{-\infty}^{+\infty} \int_{-\infty}^{+\infty} P_f(\nu,t)\, dt d\nu \tag{4.6}$$

Finally, the P_f can be treated as a probability density function, therefore the mean instantaneous frequency (MIF) can be evaluated:

$$\bar{\nu}(t) = \frac{1}{\int_{-\infty}^{+\infty} P_f(\nu,t)\, d\nu} \int_{-\infty}^{+\infty} \nu \cdot P_f(\nu,t)\, d\nu \tag{4.7}$$

By analysing the MIF trace of the injector inlet pressure signal, namely $p_{inj,in}$ (cf. Fig. 4.3), the main events pertaining to the injection, including the start and the end of the injection, can be detected. In fact, the MIF trace results to be sensitive to the needle movements, and both the beginning of the upstroke phase (when the injection starts) and the end of the downstroke phase (when the injection is terminated and a water hammer is triggered by the nozzle closure) related time instants can be identified. By means of a large learning phase based on the MIF traces, the injection temporal length ITL can be estimated.

4.3.2 Injector characteristics

Fig. 4.16 reports the injected mass (measured by means of the HDA as an average over 100 consecutive engine cycles) for different ET and p_{nom}. The fuel temperature in the tank (T_{tank}) has been set either at 40 ℃ (cf. the dashed lines and circle symbols in Fig. 4.16) and 68 ℃ (cf. the continuous lines and square symbols in Fig. 4.16). Diesel fuel injection system manufacturers generally use 40 ℃ as a reference temperature for hydraulic tests. Meanwhile 68 ℃ represent the maximum temperature that can be reached on the used bench.

The M_{inj} vs. ET curves, for fixed T_{tank} and p_{nom}, are fixed by means of a third-order polynomial. The injected mass increases with T_{tank} under fixed

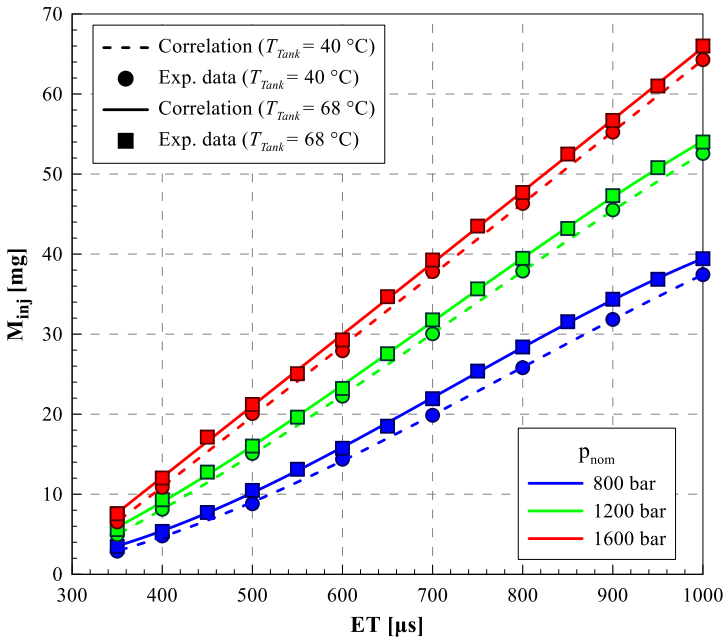

Figure 4.16: Injector characteristics $ET - M_{inj}$ for different p_{nom} and T_{tank}.

values of p_{nom} and ET (in accordance with Chap. 2). In addition, the higher differences between the injected mass when T_{tank} varies occur for lower pressure levels.

Figs. 4.17a and 4.17b report the injected flow-rate patterns (G_{inj}) for different ET values referring to p_{nom}=800 bar and p_{nom}=1600 bar, respectively. In both the cases the flow-rates pertaining to 40 ℃ and 68 ℃ of T_{tank} are shown. As can be inferred from Fig. 4.17a, the injected flow-rate at $p_{nom} = 800$ bar is mostly controlled by the needle seat passage, in fact the higher the ET, the higher the maximum needle lift reached and the higher the maximum value of injected flow-rate. This phenomena does not occur at $p_{nom} = 1600$ bar (cf. Fig. 4.17b), where the flow-rate is mostly controlled by the nozzle holes, hence, there is not a dependence between the maximum of G_{inj} and the ET. This justifies a greater impact of the needle lift trace on the injected flow-rate time pattern when $p_{nom} = 800$ bar. Since the main effect of the increased temperature is a reduction in the fuel viscosity (cf. Sect. 2.2 in Chapt. 2) and a subsequent reduction of the friction force acting on the needle, the thermal effect becomes more obvious at $p_{nom} = 800$ bar than at $p_{nom} = 1200$ bar or $p_{nom} = 1600$ bar. Data presented in Figs. 4.17a and 4.17b are in accordance whit Chapt. 2.

As can be observed from Fig. 4.16, when $p_{nom} = 800$ bar and $ET = 800$ µs, the difference on the injected mass with respect to the case with $T_{tank} = 40$ ℃ and with $T_{tank} = 68$ ℃ can reach a value close to 3 mg. Moreover, the temperature variation experienced by the injection system can generally be more important when it is installed on the engine than the one considered

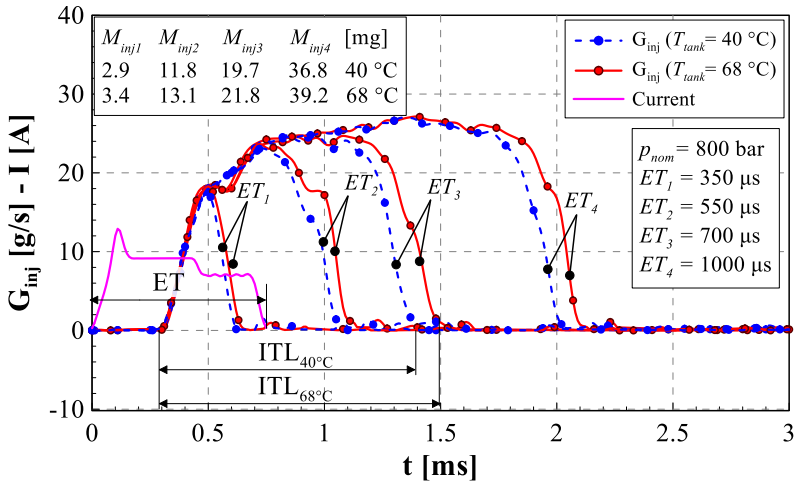

(a) p_{nom}=800 bar.

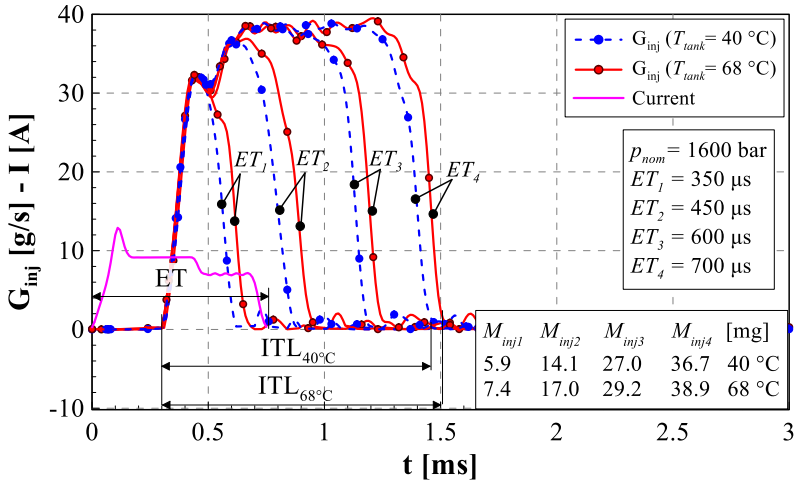

(b) p_{nom}=1600 bar.

Figure 4.17: Injected flow-rates for different values of ET and T_{tank}.

in these experiments at the hydraulic rig. The determination of the thermal regimes in the injector nozzle during an engine cycle is a complex procedure [142]: the fuel temperature at the injector inlet results to grow of about 1 ℃ for every 100 bar of pump compression and the biggest contribution on the temperature rise is given by the fuel passage through the injector and the injection holes. Nevertheless, pertaining to the analysis presented in this Section, it is sufficient to characterize the thermal regime by means of T_{tank}, which represents an easy controllable temperature. The start of injection (SOI) does not vary with T_{tank} (cf. Figs. 4.17a and 4.17b), but the flow-rate time histories pertaining to $T_{tank} = 40$ ℃ start to decrease in advance, hence the end of injection (EOI) will be reduced. ITL can be expressed as:

$$ITL = EOI - SOI \tag{4.8}$$

and it increases with T_{tank}. Consequently, for a fixed p_{nom} value, the M_{inj} versus ET correlation results to be shifted if T_{tank} varies, as shown in Fig. 4.16. The ITL-M_{inj} data have been fitted by means of third-order polynomial for each p_{nom} and the obtained correlations are reported in Fig. 4.18. As can be noticed, the correlation between ITL and M_{inj} is the same for the two considered T_{tank}, for a fixed p_{nom}. Thus, the ITL-M_{inj} correlation results to

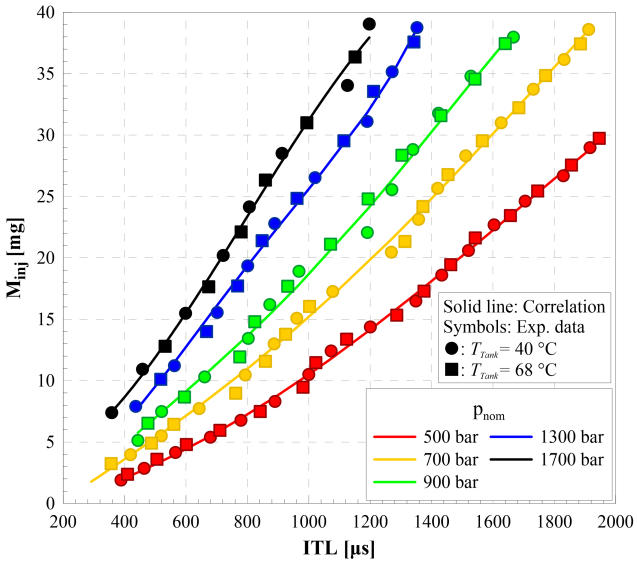

Figure 4.18: $ITL - M_{inj}$ correlations for different p_{nom} and T_{tank}.

be independent with respect to the fuel temperature. From this, the M_{inj} can be estimated by means of p_{nom} and ITL values, independently of T_{tank}.

4.3.3 Implementation of the *ITL* TFA-based sensor

Fig. 4.19 reports the G_{inj}, the $p_{inj,in}$ and the energizing current time histories pertaining to $p_{nom} = 1200$ bar and $ET = 600$ µs, as an average of 100 consecutive engine cycles. Before the start of the injection the pressure trace is almost horizontal, due to the absence of residual pressure waves. When the energizing current starts, a slight reduction in $p_{inj,in}$ can be noticed, as a consequence of the pilot-valve opening. At the effective beginning of the injection (SOI) an expansion wave propagates from the nozzle to the rail-to-injector pipe, and it is marked as "1" in Fig. 4.19. The triggered waves are reflected by the rail and they propagate back and forth along the injector feeding pipe, letting the $p_{inj,in}$ fluctuate with respect to the time. Oscillations amplitude is remarkable over the entire injection, nevertheless they are gradually damped by concentrated losses and wall friction along the rail-to-injector pipe. At the end of the injection (EOI), the nozzle closure produces a water hammer which let the $p_{inj,in}$ to sharply rise (the event is marked with "2" in Fig. 4.19).

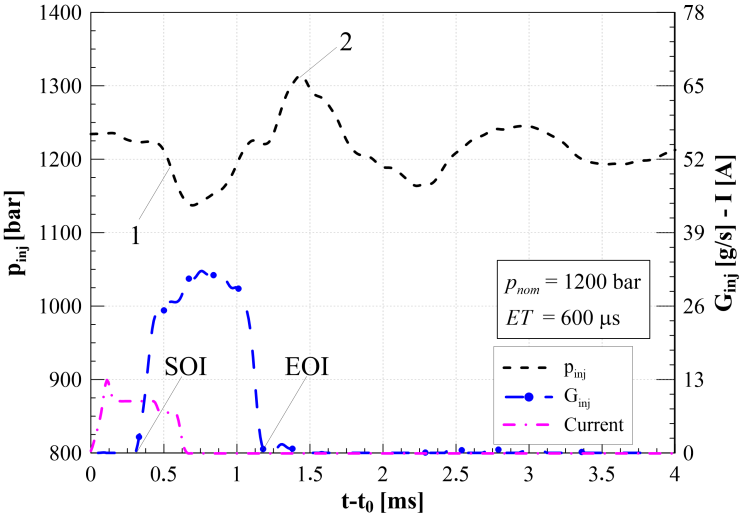

Figure 4.19: G_{inj}, $p_{inj,in}$ and the current referring to $p_{nom} = 1200$ bar and $ET = 600$ µs.

As has been clarified, the main events involving changes in $p_{inj,in}$ trace (cf. "1" and "2" in Fig. 4.19) are strongly linked to SOI and EOI. However, it is not easy to exactly determine these time instants from the $p_{inj,in}$ pattern, due to the disturbances produced by the triggered and the reflected pressure waves. TFA can represent a useful tool to be applied to $p_{inj,in}$ in order to easily determine SOI and EOI used in the injected mass estimation. Generally, the SOI and EOI time instants occur within a time span of 4 ms. In order to correctly locate those time instant by means of the TFA and to avoid the presence of leakage errors due to the non-periodic nature of the $p_{inj,in}$ signal, only 8 ms of the pressure trace is considered for the MIF evaluation. The measured $p_{inj,in}$ is filtered by means of a Butterworth low-pass filter of the fourth order (cut-off frequency of 50 kHz) and the processed signal, namely $p_{inj,in_{fil}}$, is used as the $f(t)$ signal in Eq. (4.4). A Hanning window has been chosen as the window function in Eq. (4.4):

$$h_w(n) = 0.5 \cdot \left[1 - \cos\left(2\pi \frac{n}{N}\right)\right],\ 0 \leq n \leq N \tag{4.9}$$

where n refers to a discretized time instant in the window and $N+1$ represents the window duration in terms of number of samples. In this work, a window length of 502 µs has been selected. By considering that the sample frequency of $p_{inj,in}$ is 500 kHz, N will be equal to 251. By taking into account these variables, the STFT referred to $p_{inj,in}$ can be evaluated with Eq. (4.4) and, consequently, the MIF is then calculated by means of Eqs. (4.5) and (4.7).

4.3.4 Results

Figs. 4.20-4.22 show the electrical current, G_{inj}, $p_{inj,in}$ and MIF time histories for three different working conditions in terms of p_{nom} and ET, with $T_{tank} = 40$ °C. The MIF time history in the figures has a constant value before the electrical current rises, but at the very beginning it keeps a large value (not visible in the graphs) due to the leakage error. The first local maximum in the MIF is related to the nozzle opening (marked with "1" in Figs. 4.20-4.22) and it is assumed as the hydraulic start of the injection (SOI), and it is located around 0.1 ms after the effective start of the injection, when G_{inj} becomes higher than zero (cf. Fig. 4.20-4.22). This delay is linked to the time necessary for the rarefaction wave triggered by the start of the injection to propagate

and reach the pressure transducer [143]. Similarly, the time instant where the absolute maximum value of the MIF is present (associated to the water hammer triggered by the nozzle closure) occurs about 0.1 ms after the effective end of the injections and it is assumed as the EOI. From the experimental campaign it has been seed that this criterion can be applied for all the considered points for both $T_{tank} = 40$ °C and $T_{tank} = 68$ °C.

The injection duration estimated by means of the MIF (ITL_{est}) and the real one, i.e. ITL, have been obtained with Eq. (4.8) by using the experimental data corresponding to the MIF and the injected flow-rate, respectively. If delays at the start and at the end are similar for ITL_{est}, this can be considered coincident with ITL. This occurs for Figs. 4.20 and 4.21, as is reported in their legends, the errors between ITL and ITL_{est} is 1.49 µs and 5.71 µs, respectively (the percentage error is below 1%).

In Fig. 4.22 the same quantities of Figs. 4.20 and 4.21 are reported, for the working condition with $p_{nom} = 600$ bar and $ET = 1000$ µs. The delay between the MIF-estimated SOI and EOI is around 0.18 ms with respect to the real ones. However, the error between the ITL and ITL_{est} is 90.74 µs, that is much higher than the cases presented in Figs. 4.20 and 4.21. A similar problem occurs when a very large ET is considered and the cause may be the superposition of the water hammer and the waves reflected by the rail, travelling back and

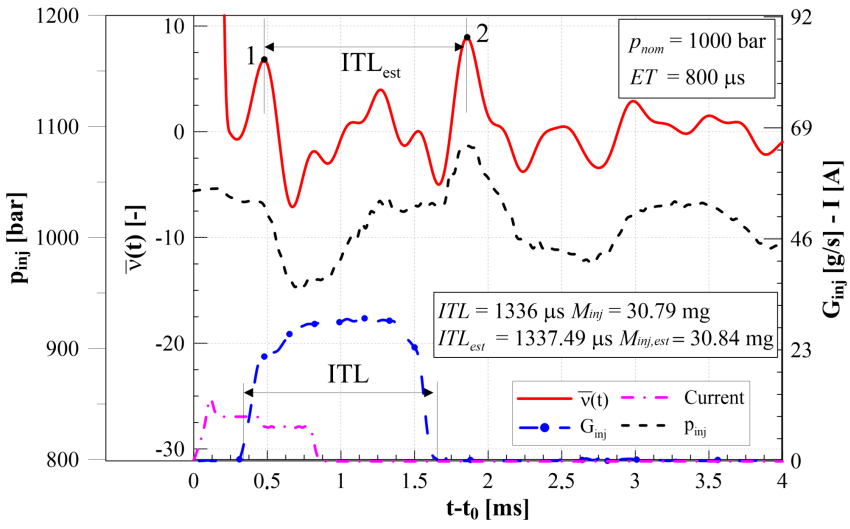

Figure 4.20: The normalized MIF, G_{inj} and $p_{inj,in}$ time histories ($p_{nom} = 1000$ bar and $ET = 800$ µs).

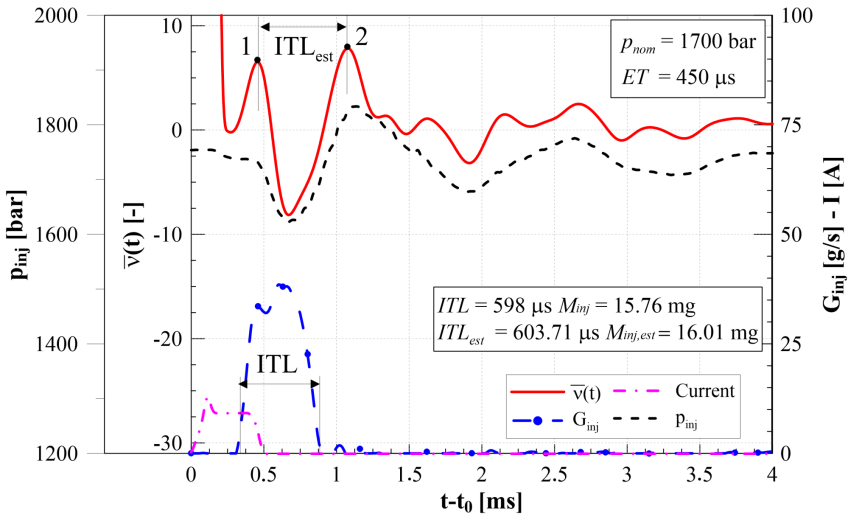

Figure 4.21: The normalized MIF, G_{inj} and $p_{inj,in}$ time histories ($p_{nom} = 1700$ bar and $ET = 450$ µs).

forth along the injector feeding pipe (nevertheless, $ET = 1000$ µs is not usually applied in modern injector systems).

The evaluated ITL_{est} data reported in Figs. 4.20 and 4.21 have been applied to the correlation reported in Fig. 4.18 and the estimations of the injected mass ($M_{inj,est}$) have been obtained (30.84 mg and 16.01 mg, respectively). By

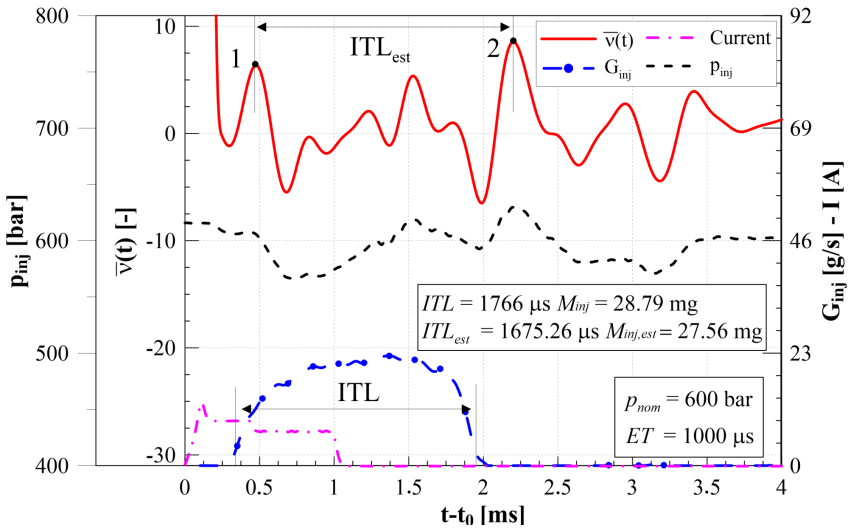

Figure 4.22: The normalized MIF, G_{inj} and $p_{inj,in}$ time histories ($p_{nom} = 600$ bar and $ET = 1000$ µs).

comparing the estimated injected mass with the corresponding one measured by means of the HDA flowmeter, the error in the prediction results to be below 0.5 mg, which is a very satisfactory result. Regarding the case in Fig. 4.22, it results that $M_{inj,est} = 27.56$ mg and the difference with respect to the measured one is around 1.2 mg. The $M_{inj,est}$ has been evaluated for different working points in terms of p_{nom} and ET, by determine the ITL_{est} and by applying it to the correlation in Fig. 4.18. The absolute value of the difference between M_{inj} and $M_{inj,est}$, namely the prediction accuracy $|\Delta M_{inj}|$, is reported in the vertical coordinate of the 3D graphs in Fig. 4.23, as a function of p_{nom} and ET. In Fig. 4.23a one has $T_{tank} = 40$ ℃, while in Fig. 4.23b one has $T_{tank} = 68$ ℃.

As can be observed from Fig. 4.23, the error is generally lower than 1 mg for over 80% of the considered working conditions (the maximum injected mass per engine cycle is below 45 mg for the considered application). However, $|\Delta M_{inj}|$ can become higher than 1.5 mg for either 500 bar$\leq p_{nom} \leq$600 bar and medium and high ET values for T_{tank} equals to both 40 ℃ and 68 ℃ or for 350 µs $\leq ET \leq$450 µs and high values of p_{nom} for $T_{tank} = 40$ ℃. It has been observed that two different contributions can be recognized in the $|\Delta M_{inj}|$ error. The first is represented by the correlation; even if the fitting is satisfactory, with an accuracy within 0.5 mg (cf. Fig. 4.18), this contribution cannot be considered as negligible for a state-of-the-art fuel injection system. The second, that is the predominant one, regards the inaccuracy in the ITL estimation due to the pressure waves superposition. In fact, the injected flow rate is a function of both the p_{rail} (controlled by the ECU) and the needle dynamics (cf. Sect. 2.5 in Chapt. 2). The latter aspect is only roughly taken into account in the standard engine calibration, by means of the ET that, as has been shown, can be significantly different from the effective injection duration. By means of the ITL-M_{inj} correlation implementation on the engine ECU the M_{inj} interpolation model would improve due to the stronger link between the ITL and the needle lift, if compared with the ET one. Moreover, the ITL-based correlation results to be independent with respect to the injector thermal regime: this is a key point in the injected mass prediction, since the fuel temperature strongly influences the injected mass, for fixed ET and p_{nom} (cf. Fig. 4.16).

Preliminary tests have been performed involving pilot-main injections. In this case, it is not possible to evaluate the ITL with a satisfactory accuracy,

due to the numerous disturbances affecting $p_{inj,in}$, especially in the short dwell time range. However, the presented methodology may be applied to the pilot injection control, leading to a reduction in terms of soot and NO_x engine out emissions and a diminished combustion noise.

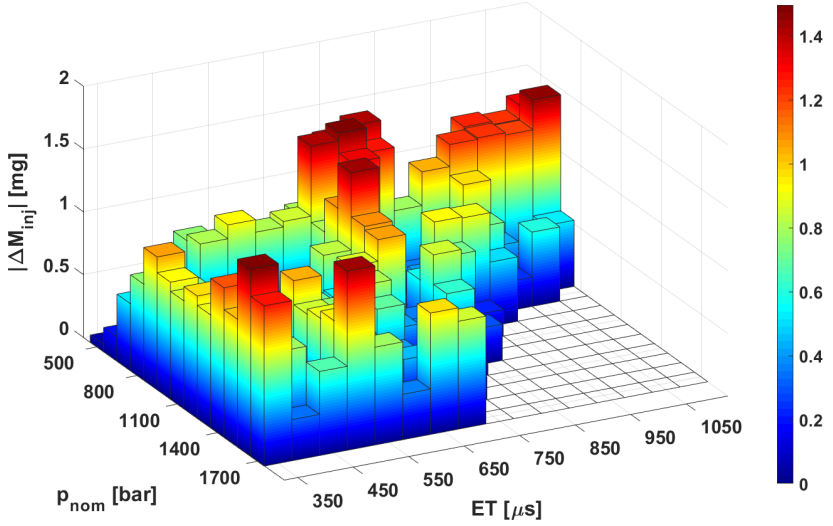

(a) T_{tank}=40 °C.

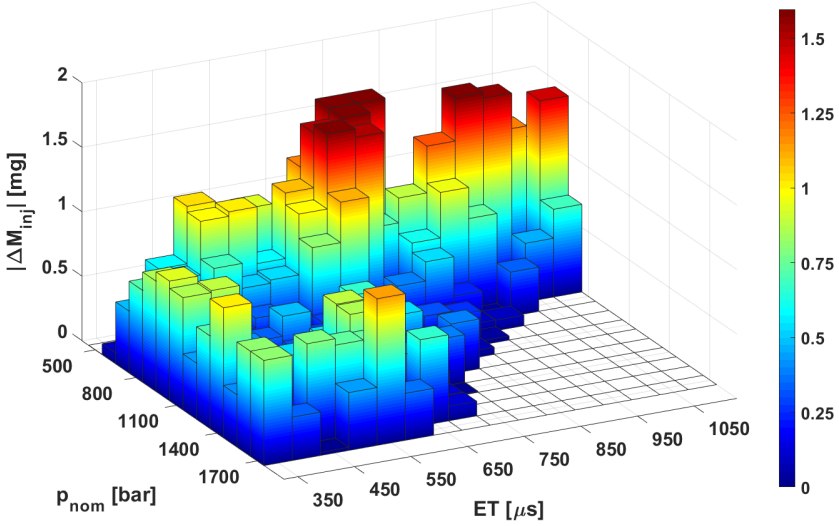

(b) T_{tank}=68 °C.

Figure 4.23: Injected mass estimation accuracy for different p_{nom} and ET.

Chapter 5

Numerical and experimental analysis of the Common Feeding injection system

5.1 Experimental setup

The CR and CF systems have been experimentally characterized at the same hydraulic test bench already described in Sect. 2.1, with the identical calibration fluid. The HDA flowmeter is used to evaluated the injected flow-rate. By means of the KMM flowmeters the injectors recirculated flow-rates are detected. The pressure at the injector inlet is measured, for both the CR and CF systems, by means of piezoresistive pressure sensors. Furthermore, the rail pressure signal in the CR system is detected by means of another piezoresistive transducer. As far as the CF system is concerned, it was not possible to measure the pressure inside the chamber downstream the pump. Finally, the current signal to the injector pilot stage has been measured by means of a current clamp.

A CPU, equipped with low-pass filters with an adjustable cut-off frequency, processes the pressure traces from the pressure transducers, the instantaneous injected flow-rate from the HDA and the current from the clamp. Signals are then cleaned from spurious oscillations. An oscilloscope, installed at the conditioner output, is used to synchronize the time distributions. As far as the

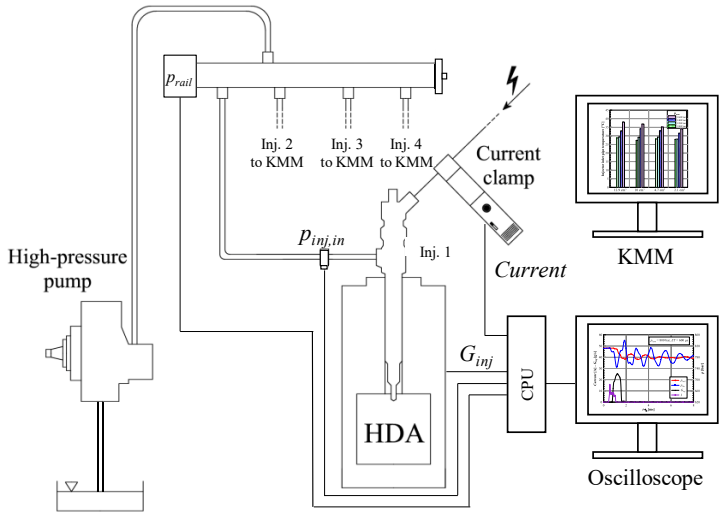

Figure 5.1: Scheme of the acquisition system.

KMM outcomes, the system itself is able to display the flowed fuel quantity for an engine cycle. Figure 5.1 reports a scheme of the acquisition system.

All the experimental campaign has been performed at a constant pump speed, i.e. $n = 1000$ rpm, corresponding to 2000 rpm of engine speed. Since n does not produce any evident influence on the injection systems performance, the presented results can be generalized to other speeds [95].

5.2 Comparison between the CR and CF systems

Figures 5.2a and 5.2b show the schematic and the picture of the hydraulic layout of the CR and CF injection systems, respectively. In the CR system, the high-pressure pump delivers the fuel to an accumulator (the rail), whose volume is $V_{rail} = 12.9$ cm^3 for the standard system, by means of a pipe with an internal diameter of 2.7 mm. The effect of the rail size in the system performance has been analysed with a series of rail prototypes featuring a volume of 10 cm^3, 4.7 cm^3 and 2.1 cm^3, realized by maintaining the length and by varying the internal cylinder diameter.

As far as the CF system is concerned [43], reported in Figs. 5.2b and 5.3, a chamber C (item 4 in Fig. 5.3), featuring a cross-shape internal volume

$V_C = 10$ cm^3, has been manufactured. Three different prototypes, with the same volume and shape, have been prepared: two of them feature an additional set of gauged orifices, whit a diameter of either $d_{or} = 1.2$ mm or 1.6 mm, at the connection ports of the chamber with the chamber-to-injector pipe, in order to reduce the pressure waves amplitude. The rail pressure sensor, used to measure the pressure signal in the rail, has been installed in the chamber C (cf. item 5 in Fig. 5.3). With this layout, a reduction in terms of cost and an easier installation have been achieved. Furthermore, if the injection system patent is owned, only the manufacturing cost must be incurred, which usually represents just a part of the final price of a product.

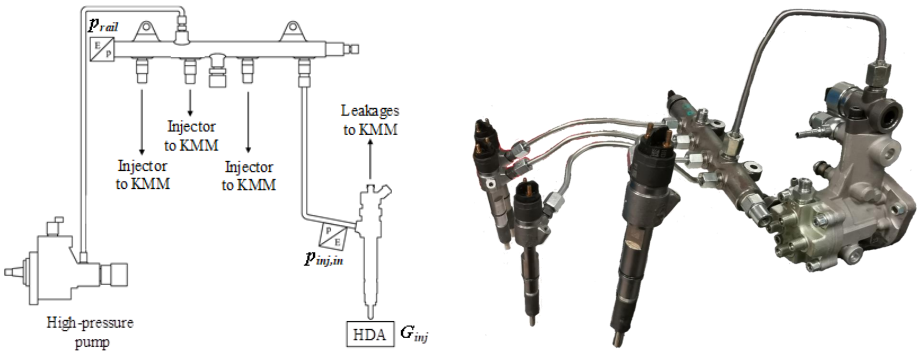

(a) CR system

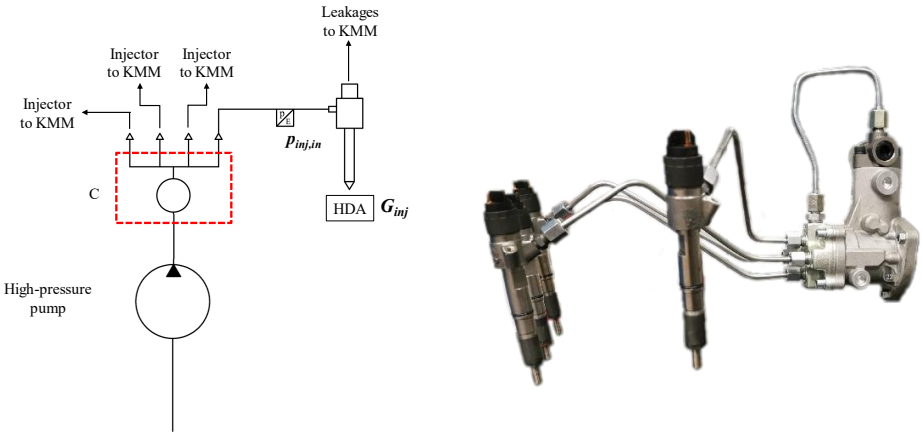

(b) CF system

Figure 5.2: The schematic and the picture of the high-pressure circuit of the CR and the CF systems.

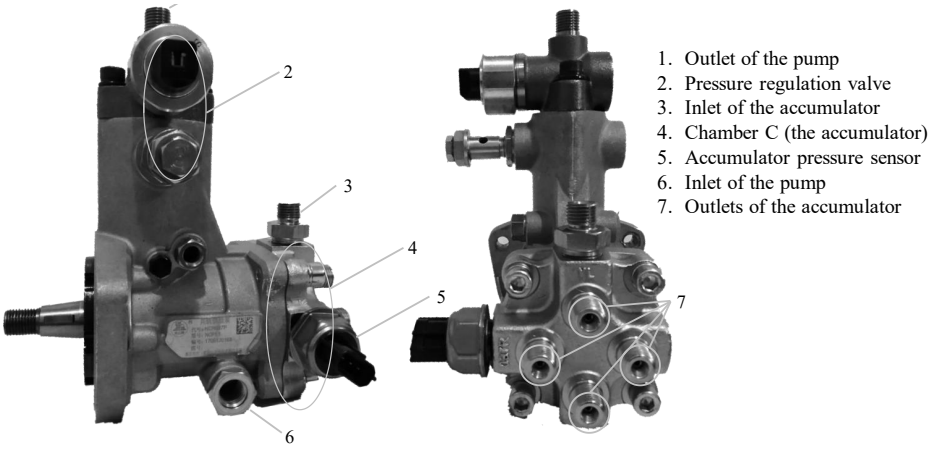

Figure 5.3: The high-pressure pump with the integrated accumulator.

For both the CR and CF systems, a single cylinder double-acting hydraulic pump is used. At the pump outlet a solenoid valve (cf. item 2 in Fig. 5.3) is employed to control the fuel pressure in the high-pressure line by draining the excess pumped fuel. All the high-pressure pipes (for both the CF and CR systems) have a length $l = 300$ mm and an internal diameter $d = 2.7$ mm. Each injector has 6 nozzle holes with a diameter of 0.135 mm. The designed fuel injected quantity per engine cycle is in the 0.5 mg - 60 mg range, in order to fulfil the requirements of a light duty commercial vehicle engines application. The pump, injectors and different rails have been manufactured by Nanyue Fuel Injection Systems Co., Ltd.

All the tests reported have been evaluated during steady state working conditions, by considering a fixed p_{nom} and ET values and an average over 100 consecutive engine cycles.

Figure 5.4 shows the pressure at the injector inlet ($p_{inj,in}$), the injected mass flow-rates (G_{inj}) and the electrical current signal time histories for the CR layout pertaining to the different rail volumes (V_{rail}) concerning two working conditions ($p_{nom} = 1600$ bar, $ET = 180$ μs and $p_{nom} = 1100$ bar, $ET = 800$ μs). Before the rise of the current signal ($0 \text{ ms} < t - t_0 < 0.5$ ms), the $p_{inj,in}$ pressure traces are almost horizontal, for all the V_{rail}, therefore no evident effects on the subsequent injections can be observed. Minor perturbations before the current signal is switched on are ascribed to pressure waves triggered by the previous injection events transmitted to the considered rail-to-injector pipe.

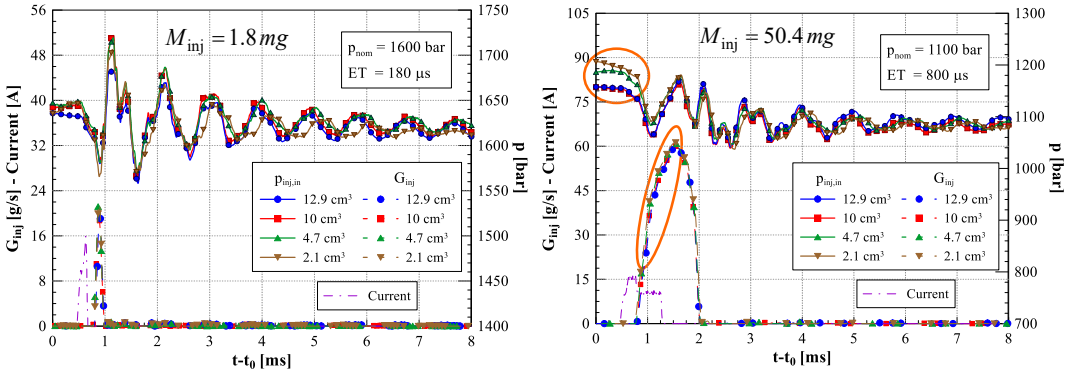

(a) $p_{nom} = 1600$ bar, $ET = 180$ µs (b) $p_{nom} = 1100$ bar, $ET = 800$ µs

Figure 5.4: Comparison of the G_{inj} and the $p_{inj,in}$ between the CR systems with different rail volumes.

If a small injection ($M_{inj} = 1.8$ mg) is considered, as in Fig. 5.4a, during the entire injection event time interval ($0\text{ ms} < t - t_0 < 8\text{ ms}$), the $p_{inj,in}$ and the G_{inj} time histories are almost coincident for all the V_{rail} values. Therefore, a change in V_{rail} has only minor effects on injections involving small fuel quantities.

As far as a large fuel injected quantity is concerned ($M_{inj} = 50.4$ mg in Fig. 5.4b), the initial part of the $p_{inj,in}$ signals, circled with a continuous line, results to be augmented as the accumulator size is reduced. This phenomenon can cause a faster needle lifting process at the injection start for the reduced accumulation volume, leading to a slightly increased injected flow-rate (cf. the circled part of G_{inj} in Fig. 5.4b), this modifies the injected quantity for a fixed ET value. In Fig. 5.4b, for all the V_{rail}, the stat of the injection triggers a depression wave travelling along the pipeline from the injector nozzle to the rail, reaching the $p_{inj,in}$ pressure sensor at $t - t_0 \approx 0.8$ ms. The fuel arriving in the nozzle from the feeding pipe passes across a restriction passage between the needle and its seat and cannot be entirely expelled through the injector orifices [137]. Therefore, a compression wave is formed at $t - t_0 \approx 1$ ms. In the meanwhile, the abovementioned depression wave has reached the rail and is here reflected as a compression wave, starting to propagates towards the injector nozzle. At the end of the hydraulic injection ($t - t_0 \approx 2$ ms) due to the needle closure, a water hammer can be observed in the $p_{inj,in}$ traces and subsequent free oscillations can be detected.

If the mass conservation equation is applied to the rail, one obtains:

$$\frac{V_{acc}}{a^2} \cdot \frac{dp_{acc}}{dt} = G_{pump} - G_{inj} - G_{leak} \tag{5.1}$$

where V_{acc} is the accumulator volume (the rail one, in this case), p_{acc} represents the mean pressure in the accumulator, a is the fluid speed of sound, and G_{pump}, G_{inj} and G_{leak} indicate respectively the fuel pumped, injected and leakage mass flow-rates. If Eq. (5.1) is integrated over a complete injection cycle (T_{inj}), it is obtained:

$$\frac{V_{acc}}{a^2} \cdot \int_{t_0}^{t_0+T_{inj}} \frac{dp_{acc}}{dt} = M_{pump} - M_{inj} - M_{leak} \tag{5.2}$$

where t_0 is a reference time instant. If a similar mass of expelled fuel ($M_{inj} + M_{leak}$) from the injector is considered independently of the V_{rail} and by considering that the pumped fuel M_{pump} is almost the same, it can be seen that $p_{inj,in}$ pertaining to a smaller V_{acc} starts with higher values. This is purposely made by the ECU to maintain the averaged value of the rail pressure close to the nominal value. The initial difference in the $p_{inj,in}$ is then compensated by the injection. In fact, from $t - t_0 \approx 1.6$ ms on, the pressure traces become almost overlapped in Fig. 5.4b.

In Fig. 5.5 the same quantities of Fig. 5.4 are reported, for a different working condition ($M_{inj} = 61.4$ mg) pertaining also to the CF system layout with $V_C = 10$ mm^3, without additional orifices. The initial value of $p_{inj,in}$ of the CF system is between that of $V_{rail} = 12$ cm^3 and 2.1 cm^3 and, consequently, the injected flow-rate related to the CF system is between those of the two considered configurations. Therefore, these features result to be mainly determined by the accumulator volume size.

The free pressure waves frequencies triggered by the injection events of the CR systems are affected by the rail size: the smaller the rail volume, the smaller the frequency of the free pressure waves. However, although the CF system features a capacitance with $V_C = 10$ cm^3, it is characterized by a pressure wave natural frequency around 30% smaller than those of the other rail sizes. This difference can be ascribed to the different accumulator shape.

In Fig. 5.6 the injector characteristics pertaining to the CR and CF systems are reported. As far as the CR systems are concerned, the two extreme values of V_{rail} have been selected, meanwhile, for the CF system, the chamber does

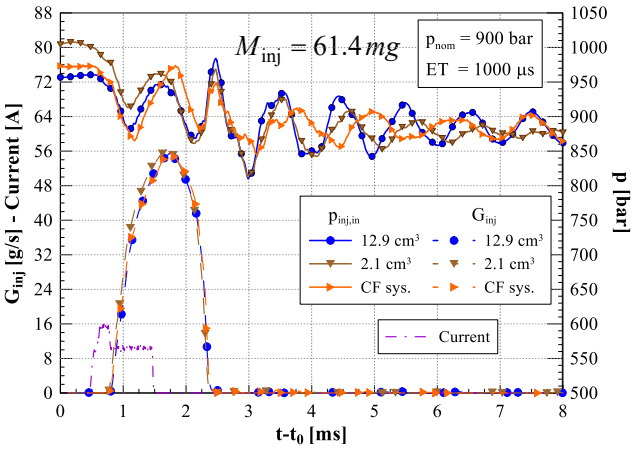

Figure 5.5: Comparison of the G_{inj} and the $p_{inj,in}$ between the CR and the CF systems.

not feature gauged orifices. It is evident that the CR system with the minimum V_{rail} has the greatest slope upon the $M_{inj} - ET$ curves, for all the p_{nom}, and the maximum difference in terms of injected mass between the two CR system is approximately 5.5 mg. Pertaining to the CF system, its characteristic results to be analogous to the one of the standard CR system, in fact, $V_C = 10$ cm^3, that is comparable to $V_{rail} = 12.9$ cm^3. Therefore, it can be confirmed that the characteristics slope increases as the accumulator volume is reduced, while there is not a dependency of the accumulator shape. Furthermore, the presented trends are also in agreement with the difference in the initial levels of $p_{inj,in}$ as the rail size changes (cf. Fig. 5.4b).

Static leakage represents the amount of fuel discharged from the injector to the tank when the pilot stage is closed. It has been measured during steady state conditions by maintaining a certain pressure level (p_{nom}) and by keeping the ET equals to zero within one engine cycle (at the present engine speed, 60 ms). Fig. 5.7a shows the static leakage regarding the CR system. If $p_{nom} > 1200$ bar it can be seen that the higher the accumulation volume is, the greater the leakage is. Generally, the static leakage can be modelled as a stationary volumetric flow-rate by following the Hagen-Pouseille formula:

$$Q_{leak} = K\frac{\bar{p}}{\bar{\mu}} \tag{5.3}$$

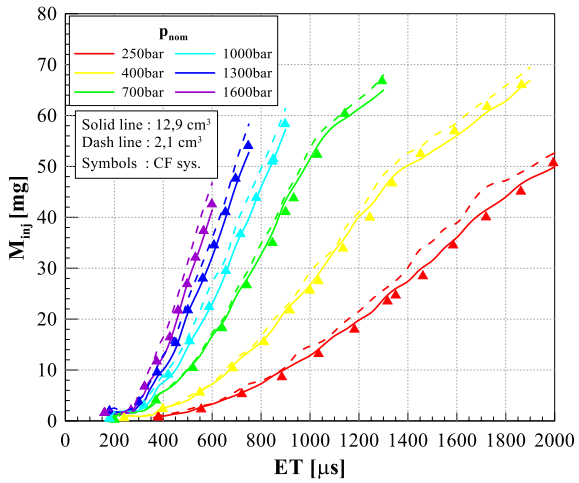

Figure 5.6: Comparison of the injector characteristics between the CR (V_{rail} = 12.9 cm^3 and 2.1 cm^3) and the CF (without gauged orifices) systems.

where K stands for a geometrical parameter depending on the pilot stage layout and on the other possible clearance passages, $\bar{\mu}$ represents the fuel dynamic viscosity, a function of the time averaged injection pressure $\bar{p}$ and temperature $\bar{T}$. The pressure $\bar{p}$, controlled by the ECU, keeps virtually constant for the same p_{nom} when V_{rail} changes. While the temperature inside the injector results to be impossible to be measured, the temperature $T_{inj,in}$ is measured along the rail-to-injector pipe (close to the injector inlet) and reported in Fig. 5.7b. If it is assumed that the $T_{inj,in}$ tendency reproduces the $\bar{T}$ one and by considering

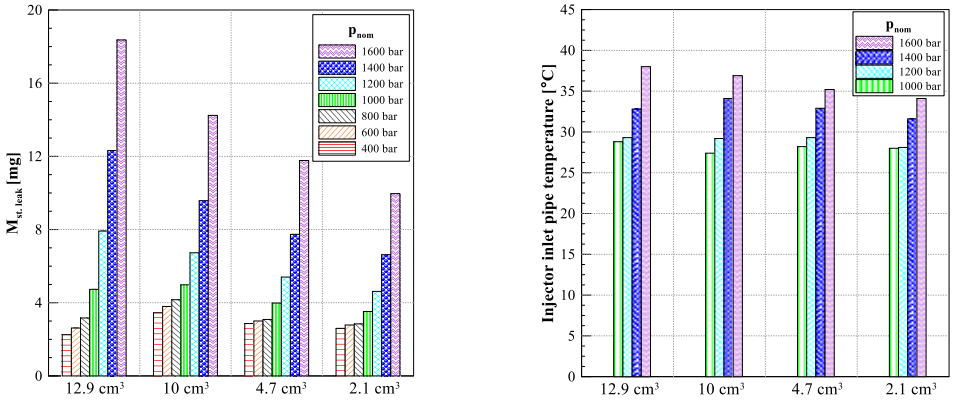

(a) Static leakage (b) Injector inlet temperature

Figure 5.7: Comparison of the $M_{st,leak}$ and the $T_{inj,in}$ between the CR systems with varied V_{rail}.

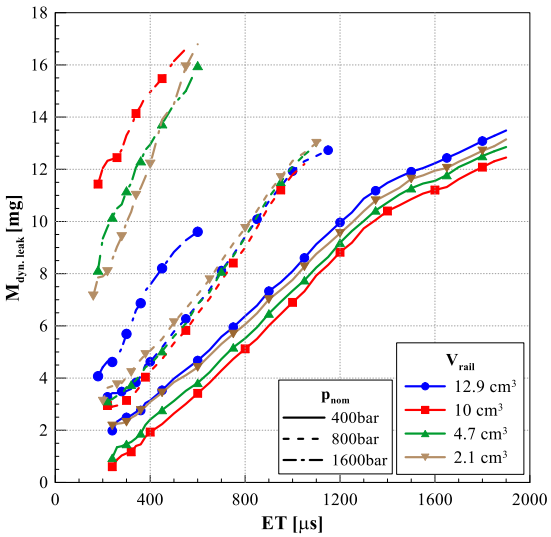

Figure 5.8: Comparison of the $M_{dyn,leak}$ between the CR systems with varied V_{rail}.

that $\bar{\mu}$ is sensitive to $\bar{T}$, the difference in the static leakages can be ascribed to a thermal effect.

Pertaining to the dynamic leakage, it represents the fuel quantity flowed through the opened pilot valve during an injection event within one engine cycle. It is evaluated by subtracting from the total leakage the static one, for the considered pressure level. This quantity is represented in Fig. 5.8, for the CR system. When ET increases, i.e. the opening time of the pilot stage, the dynamic leakage rises. Furthermore, it can be observed that the higher is the pressure level, the more pronounced the dynamic leakage is. No evident trend can be inferred regarding to the V_{rail}.

In Fig. 5.9 it is reported the injected mass coefficient of variation for the CR system. It has been evaluated by the HDA flowmeter over 100 consecutive engine cycles. As a reference, an injection should at least feature a coefficient of variation smaller than 10% [62]. As can be inferred from Fig. 5.9, almost all the points fulfil this criterion, only some points under $p_{nom} = 250$ bar and small ET for the $V_{rail} = 2.1$ cm^3 are slightly over from the reference threshold (cf. Fig. 5.9b). Generally, the higher σ values are obtained at either low values of p_{nom} or ET. Furthermore, the higher the ET, the more reduced the coefficient of variation.

If the entire working conditions zone of Fig. 5.9 is considered, generally the coefficient increases when the accumulation volume is reduced. For conciseness

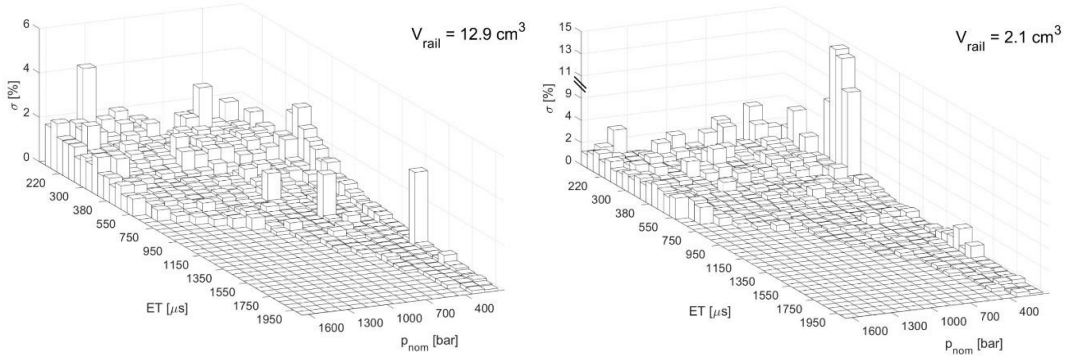

(a) $V_{rail} = 12.9$ cm^3 (b) $V_{rail} = 2.1$ cm^3

Figure 5.9: Comparison of the σ between the CR systems with different V_{rail}.

reasons, data pertaining to $V_{rail} = 10$ cm^3 and 4.7 cm^3, which follow this trend, are not reported. In Fig. 5.10 the nozzle opening delay (NOD) and the nozzle closure delay (NCD) are schematically represented. The former is defined as the time interval between the beginning of the current signal and the effective hydraulic start of injection, the latter represents the time interval from the end of the current signal to the hydraulic end of the injection. An injector with a reduced NOD is characterized by an improved dynamic response. Figures 5.11a and 5.11b show the NOD pertaining to the CR systems for the cases $V_{rail} = 12.9$ cm^3 and $V_{rail} = 2.1$ cm^3, respectively. For a fixed p_{nom}, for each configuration, NOD values have been interpolated by means of a straight line.

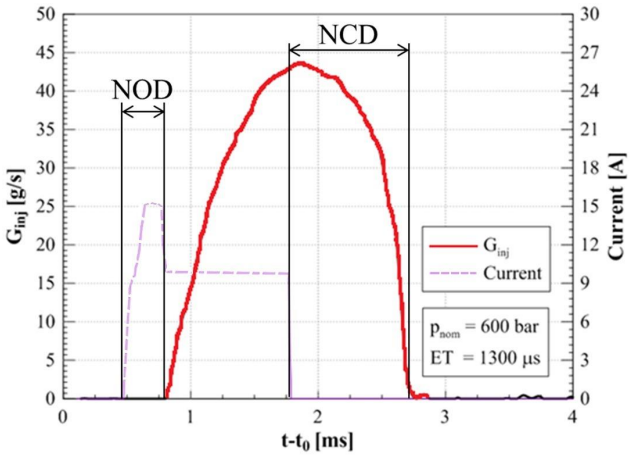

Figure 5.10: Definitions of NOD and NCD.

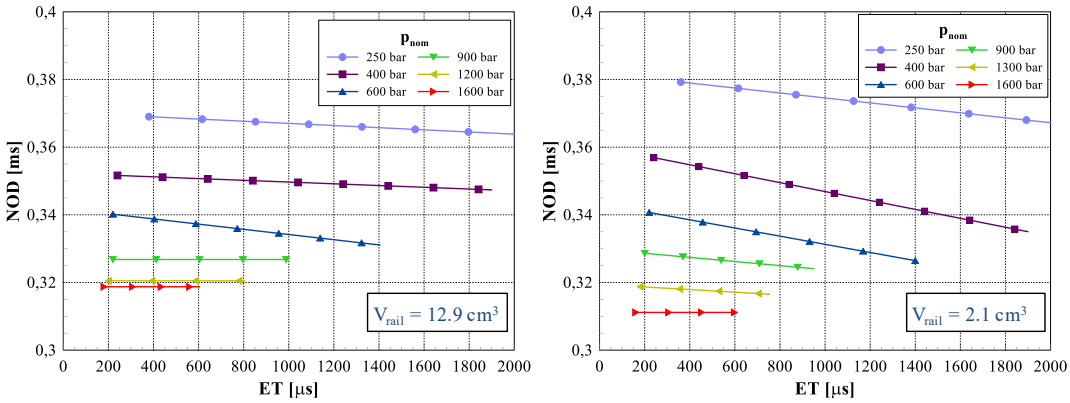

(a) $V_{rail} = 12.9$ cm^3 (b) $V_{rail} = 2.1$ cm^3

Figure 5.11: NOD of the CR systems with different V_{rail}.

In general, NOD decreases as p_{nom} increases, in fact the higher pressure level leads to a larger dynamic leakage flow-rate, reducing the time interval to empty the control chamber [144].

The NCD values, reported in Fig 5.12, result to be not affected by the rail size and they increase with ET. Furthermore, the higher p_{nom}, the greater the slopes. When the needle reaches its stroke end, for large enough ET values, NCD becomes constant with respect to ET [144]. It is obvious that the curve pertaining to a reduced p_{nom} features the maximum NCD value, in fact the needle closure force is reduced for lower level of p_{nom}.

The experimental campaign has been extended to pilot-main and main-after injections. Fig. 5.13 reports the same variables as Fig. 5.4, but pertaining to

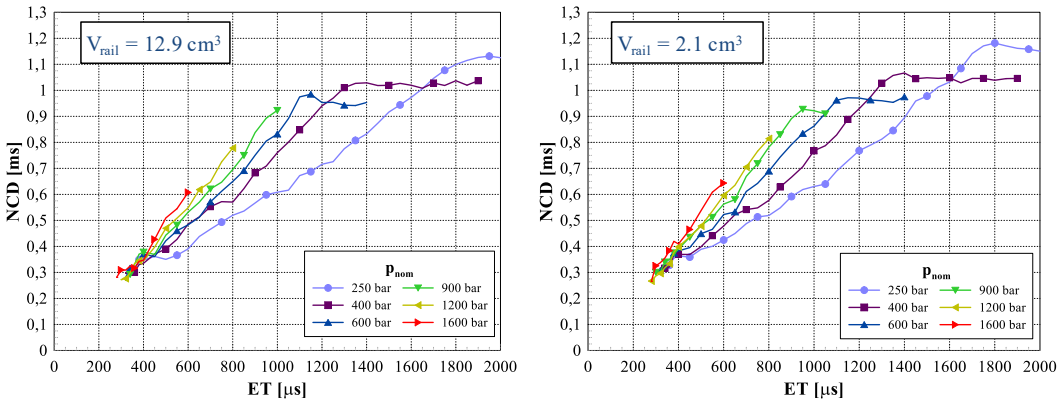

(a) $V_{rail} = 12.9$ cm^3 (b) $V_{rail} = 2.1$ cm^3

Figure 5.12: NCD of the CR systems with different V_{rail}.

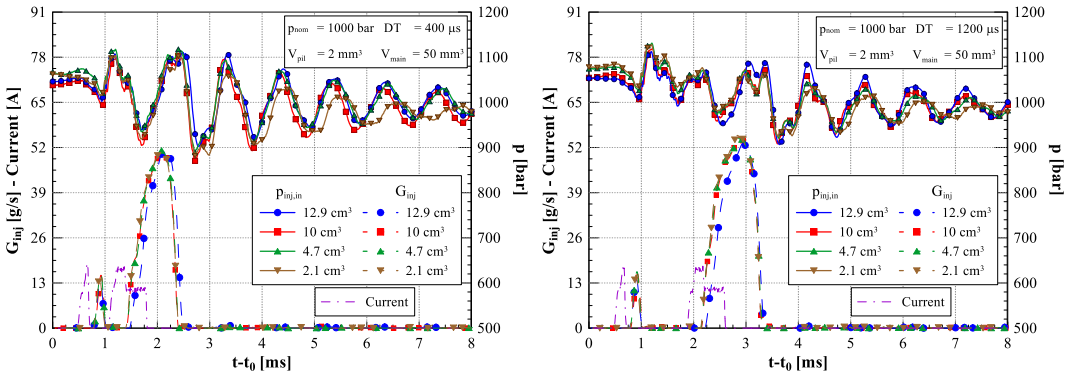

(a) $p_{nom} = 1000$ bar, $V_{pil} = 2$ mm^3, $V_{main} = 50$ mm^3 and $DT = 400$ µs

(b) $p_{nom} = 1000$ bar, $V_{pil} = 2$ mm^3, $V_{main} = 50$ mm^3 and $DT = 1200$ µs

Figure 5.13: Comparison of the G_{inj} and the $p_{inj,in}$ between the CR systems with different V_{rail} for pilot-main injections.

pilot-main injections. For each accumulation volume, the ETs have been fixed in order to realize the same injection in terms of fuel injected volume when the DT was equal to 3000 µs. Only one current time history, pertaining to $V_{rail} = 12.9$ cm^3, is represented.

Before the injection starts, the $p_{inj,in}$ is almost horizontal for all the V_{rail}. A depression wave is generated by the pilot injection and it is followed by a compression wave. The needle returning to its seat induces a water hammer which propagates along the injector feeding pipe: the triggered oscillations have an amplitude up to 200 bar and a frequency of around 1 kHz.

Figure 5.13a shows a case where the main injection starts in phase with a depression wave in the nozzle; on the contrary, Fig. 5.13b represents a case in which, for each V_{rail} value, the ETs are the same with respect to the ones of Fig. 5.13a, but the main injection occurs when a compression wave has reached the nozzle. The main injection needle lift can be strongly affected by the injector internal pressure waves, in fact the effective hydraulic injection duration can vary [145]. As a consequence, the flow-rate patterns pertaining to the main injection result to be longer in Fig. 5.13b than in Fig. 5.13a, therefore, the overall injected volume is augmented. This effect is evident in Fig. 5.14, where the pilot and main V_{inj} values, plotted with respect to the DT, in a range from 100 µs to 2000 µs, are shown. Below the injection fusion threshold the two injection events become fused, the consequent rise in the injected volume is highlighted by the circled zone in Fig. 5.14 (in this case,

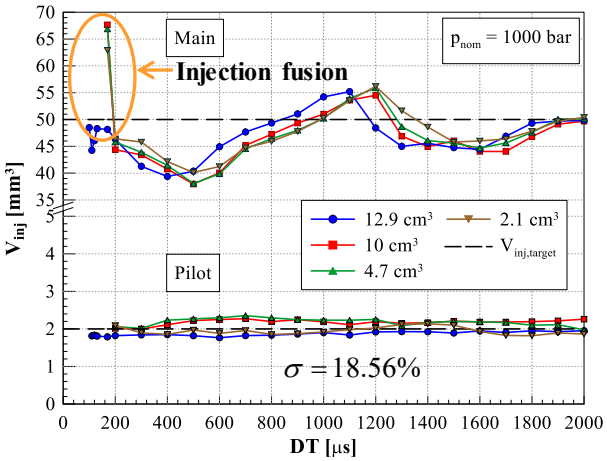

Figure 5.14: Comparison of the V_{inj} between the CR systems for pilot-main injections ($p_{nom} = 1000$ bar).

the corresponding pilot injected volume data have been removed). Over the injection fusion threshold, the pilot injected volume ($V_{inj,pil}$) is almost constant, while the main injected volume ($V_{inj,main}$) oscillates with respect to DT and its variation can be described by evaluating the percentage deviation as follows:

$$\sigma = \left| \frac{V_{main}(DT) - \bar{V}_{main}}{\bar{V}_{main}} \right| \tag{5.4}$$

where $V_{main}(DT)$ stands for the main injected volume for a certain DT and $\bar{V}_{main}$ is the averaged value with respect to DT. As can be inferred from Fig. 5.14, the σ can reaches values up to 20% for small DTs. Furthermore, it can be noticed that the $V_{inj,main}$ oscillation with respect to DT features a frequency of 1 kHz, that is the same of the free pressure waves represented in Fig. 5.13. This confirms that the pressure waves triggered by the pilot injection, travelling back and forth along the injector feeding pipe, strongly affect the main injected quantity [146].

As far as the main-after injections are concerned, also in this case the ETs have been fixed in order to obtain, for all the V_{rail}, the same injected volumes when $DT = 3000$ μs. Same quantities reported in Fig. 5.13 are shown, for the main-after schedules, in Fig. 5.15. In this case, pressure waves triggered by the main injection strongly affect the after injection fuel quantity. In Fig. 5.15a, the water hammer triggered by the needle closure pertaining to the main injection is reflected by the rail as a depression wave; this wave reaches the

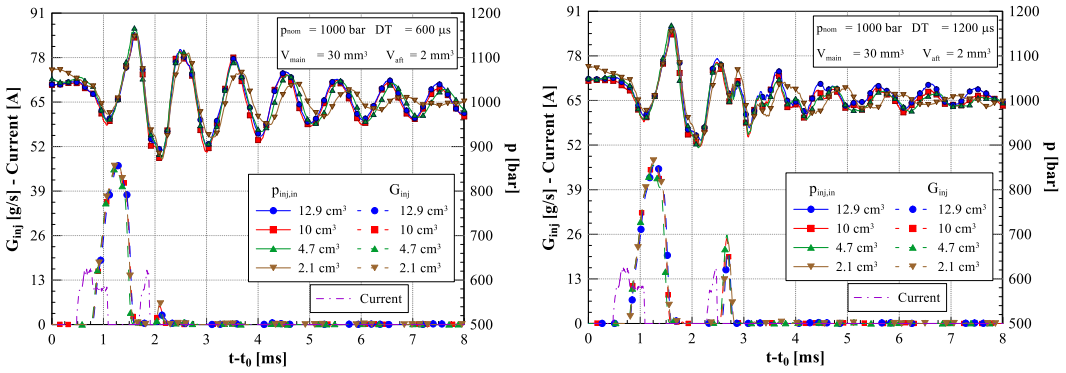

(a) $p_{nom} = 1000$ bar, $V_{main} = 30$ mm^3, $V_{aft} = 2$ mm^3 and $DT = 600$ µs

(b) $p_{nom} = 1000$ bar, $V_{main} = 30$ mm^3, $V_{aft} = 2$ mm^3 and $DT = 1200$ µs

Figure 5.15: Comparison of the G_{inj} and the $p_{inj,in}$ between the CR systems with different V_{rail} for main-after injections.

nozzle at the beginning of the after injection. Therefore, the after injected quantity results to be reduced with respect to the target. On the contrary, in Fig. 5.15b, the after injection begins when a compression wave has reached the nozzle, leading to an augmented after injected volume. Fig. 5.16 presents the injected volumes pertaining to the main and after injection schedules ($V_{inj,main}$ and $V_{inj,aft}$, respectively). Similarly to Fig. 5.14, also in Fig. 5.16 an evidet oscillation of the after injected volume can be inferred, with the same frequency of the free pressure waves, around 1 kHz, triggered by the main injection.

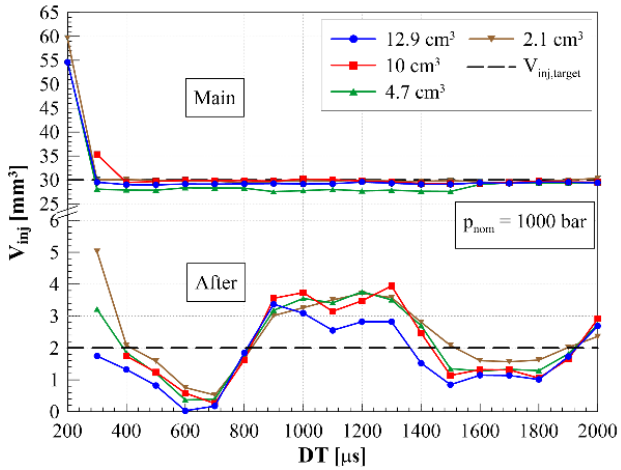

Figure 5.16: Comparison on the V_{inj} between the CR systems for main-after injections ($p_{nom} = 1000$ bar).

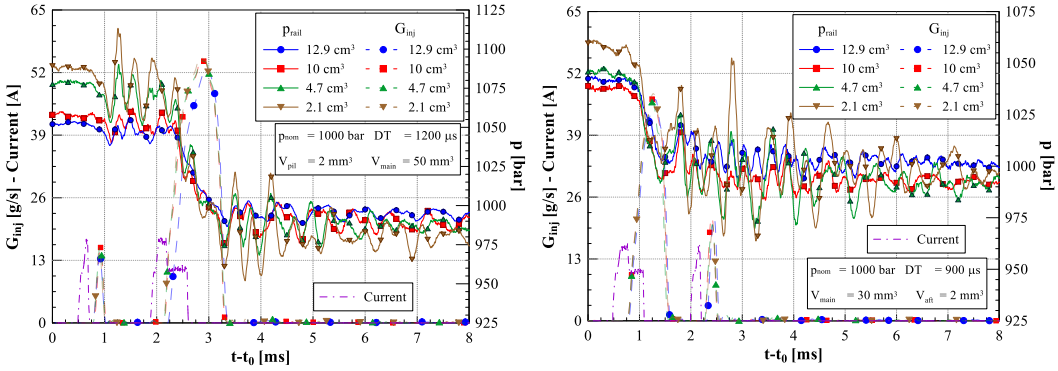

(a) $p_{nom} = 1000$ bar, $V_{pil} = 2$ mm^3, $V_{main} = 50$ mm^3 and $DT = 1200$ µs

(b) $p_{nom} = 1000$ bar, $V_{main} = 30$ mm^3, $V_{aft} = 2$ mm^3 and $DT = 900$ µs

Figure 5.17: Comparison of the G_{inj} and the p_{rail} between the CR systems with different V_{rail} for pilot-main and main-after injections.

Figure 5.17 reports the flow-rate and rail pressure time histories for the different rail sizes for a pilot-main injection (cf. Fig. 5.17a) and a main-after injection (cf. Fig. 5.17b). As has been already discussed for the $p_{inj,in}$ traces, the smaller is the accumulator, the more pronounced the p_{rail} reduction caused by the injection is (for a fixed fuel injected volume). Furthermore, when the rail size is reduced, the pressure level at the beginning of the injection increases in order to maintain the p_{nom} average value, and the needle closure water hammer induces a pressure rise more evident as the rail volume reduces. However, the differences in the rail pressure dynamics, for the different V_{rail}, do not affect the global performance of the injection system.

Figure 5.18 exhibits the $V_{inj,main}$ fluctuation with respect to DT for the CF systems for the identical working condition presented in Fig. 5.14. As can be inferred, the presence of gouged orifices is able to damp the pressure waves [95] and therefore the $V_{inj,main}$ oscillation amplitude is attenuated. The more d_{or} is reduced, the more evident the damping effect is. Furthermore, it can be seen that the passive damping increases the free pressure waves period and thus that of the oscillations presented in Fig. 5.18. For sake of conciseness, the injected flow-rate time histories pertaining to this system layout are omitted. In previous works it has been obtained that this passive damp method for the pressure wave can reduce the injected volume, for fixed ET and p_{nom}, up to 8% [145].

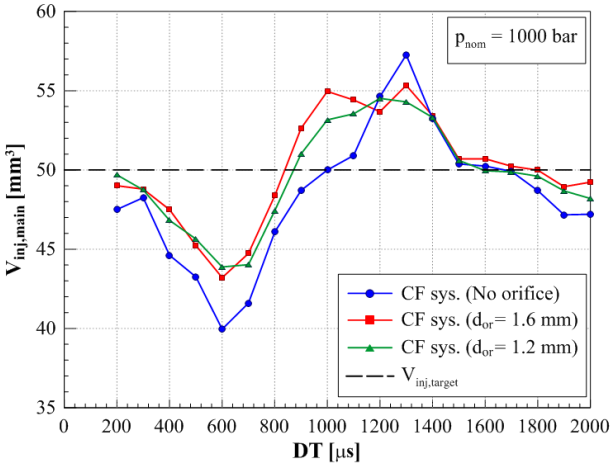

Figure 5.18: Comparison of the V_{inj} fluctuations with DT between the CF systems for pilot-main injections ($p_{nom} = 1000$ bar).

5.3 Results of the numerical simulations

In order to explore the internal dynamics performance of the CR injection system for different V_{rail}, a 1D numerical diagnostic model has been developed and validated [28]. A scheme of the 1D model is reported in Fig. 5.19. The main characteristics are the same ones described in Sect. 2.4. Boundary conditions provided to the model consist on the rail pressure trace and the electrical current signal. By means of the isothermal process assumption, the energy equation is reduced into a state equation. Therefore, the governing equations pertaining to the pipe model are based on the generalized Euler partial differential equations:

$$\frac{\partial}{\partial t}\begin{bmatrix}\rho\\ \rho u\end{bmatrix}+\frac{\partial}{\partial x}\begin{bmatrix}\rho u\\ \rho u^2+p\end{bmatrix}=\begin{bmatrix}0\\ -4\tau_w/D\end{bmatrix} \tag{5.5}$$

where x stands for the spatial coordinate, t is the time, ρ, u, and p represent the density, the velocity and the pressure averaged over the cross-section pipe, respectively, τ_w is the wall shear stress, formed by a steady state term and an unsteady term based on the velocity time history [124].

The model validation consists in the comparison of the numerical traces of the pressure at the injector inlet and of the injected flow-rate with the correspondent experimental ones. In Fig. 5.20 is represented the numerical model validation of a pilot-main injection for the $V_{rail} = 12.9$ cm^3 (cf. Fig. 5.20a)

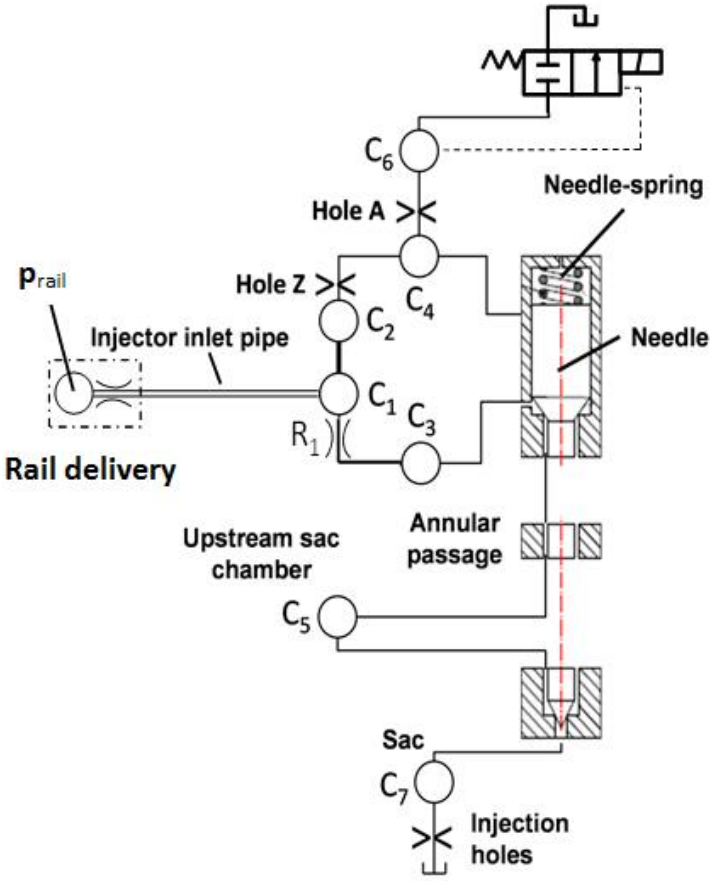

Figure 5.19: Scheme of the CR injection system 1D numerical model.

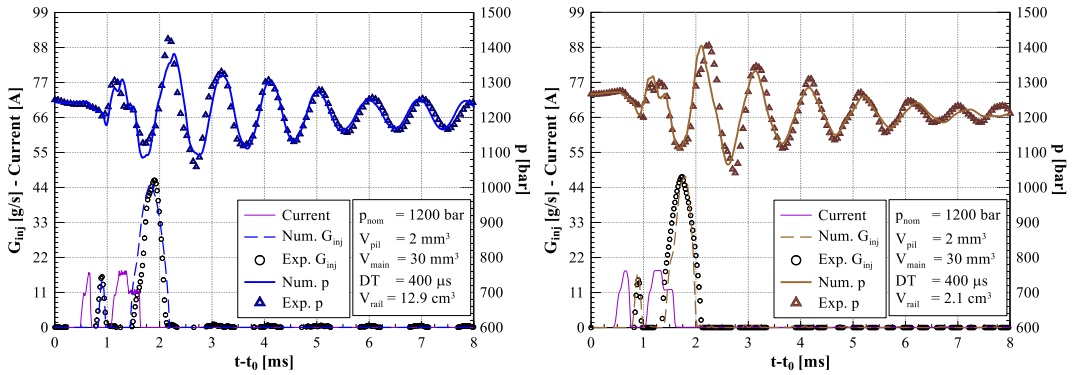

(a) $V_{rail} = 12.9$ cm^3 (b) $V_{rail} = 2.1$ cm^3

Figure 5.20: Validation of the numerical model for a pilot-main injection: $p_{nom} = 1200$ bar, $V_{pil} = 2$ mm^3, $V_{main} = 30$ mm^3 and $DT = 400$ µs.

and the $V_{rail} = 2.1$ cm^3 (cf. Fig. 5.20b) rail sizes. Both the numerical injected flow-rate and the pressure at injector inlet time histories are almost coincident with the experimental traces.

In Fig. 5.21 a single injection is considered and, for different rail sizes, the needle lift and the needle velocity are shown. It can be seen that the smaller is the rail, the augmented the needle lift maximum value and the needle opening velocity are. These two factors determine an increased injection duration and, consequently, an increased injected mass for the reduced rail sizes, for fixed ET and p_{nom}. The augmented needle lift and needle velocity are ascribed to the higher mean pressure in the hydraulic circuit at the injection start featured by a reduced rail size. Therefore, the control chamber discharges faster, leading to a faster injector response to the electric current signal [96]. As far as a pilot-main injection is concerned, if a working condition with fixed p_{nom}, DT and injected volumes is considered, some differences can be noticed in the injected mass when the rail size changes. From the numerical results shown in Fig. 5.22 it can be seen that the needle lift peak value slightly increases even if the main injection duration does not change with V_{rail}. However, the main injection begins when a higher pressure is present in the delivery chamber,

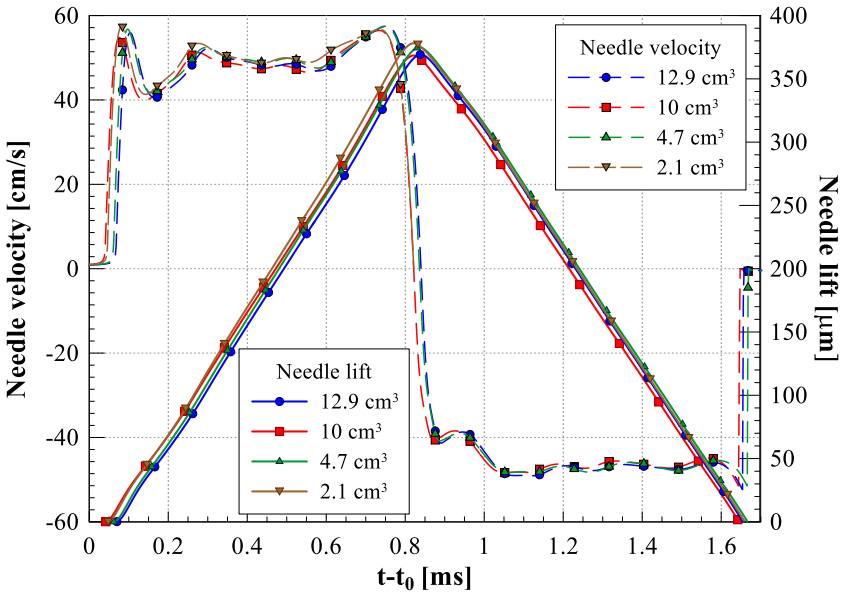

Figure 5.21: Needle lift and needle velocity pertaining to a single injection ($p_{nom} = 900$ bar and $ET = 1000$ μs).

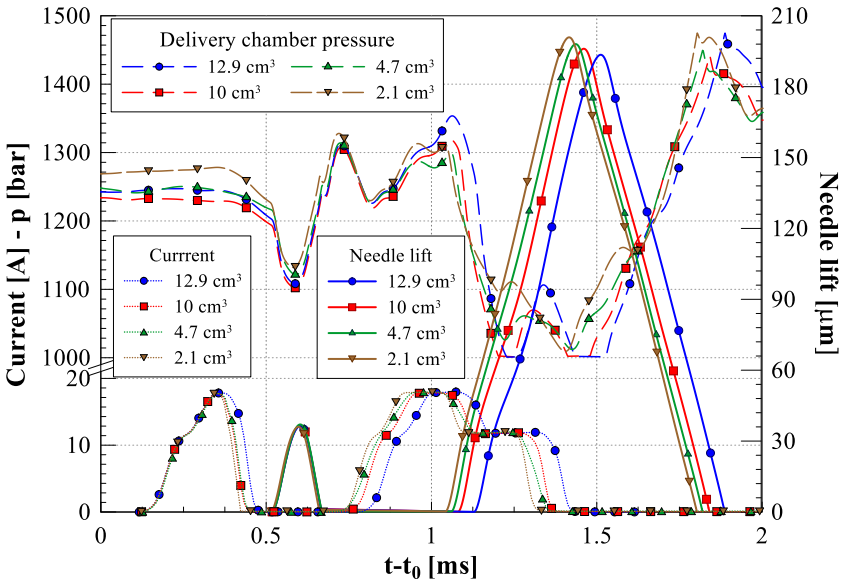

Figure 5.22: Needle lift and pressure in the delivery chamber for a pilot-main injection ($p_{nom} = 900$ bar, $V_{pil} = 2$ mm^3, $V_{main} = 30$ mm^3, $DT = 400$ µs).

when the accumulator volume is reduced. This can be ascribed to the fact that the current signals are different in order to obtain the same injection, when V_{rail} changes. In fact, in order to obtain the same injected quantities, different ET_{pil} and ET_{main} must be selected when the rail size changes (selected at $DT = 3000$ µs). From the experimental campaign it has been observed that the smaller is the rail, the reduced the ET_{pil} required to obtain a fixed pilot injected volume is. Therefore, since the DT is fixed in Fig. 5.22, the current signal pertaining to the main injection will start to rise earlier for a reduced rail size, when a depression wave has still not reached the delivery chamber.

Chapter 6

Assessment of unsteady friction models in high-pressure flows simulation

6.1 Experimental setup

The experimental campaign has been carried out at the same hydraulic test bench already described in Sect. 2.1, with the identical calibration fluid. A Common Rail diesel injection system for passenger cars (1600 bar of maximum pressure) has been used. The high-pressure reciprocating rotary pump features a displacement of 700 mm^3 and the solenoid injector is connected to the rail by means of a purposely-designed 2 m long pipe. The pipe internal diameter is 2.4 mm. Fig. 6.1a reports one of the adopted layouts. The pressure in the rail-to-injector pipe is monitored by means of three piezoresistive transducers in three different locations. The pressure time histories measured by means of Transducers 1 and 3 are provided to a 1D pipe numerical model as boundary conditions, meanwhile the pressure traces obtained from the Transducer 2 are used for the numerical model validation, where different frequency dependent friction models have been implemented. The mechanical vibration of the injection system, due to the presence of such a long injector feeding pipe, have been reduced by adopting a pump rotational speed of 750 rpm.

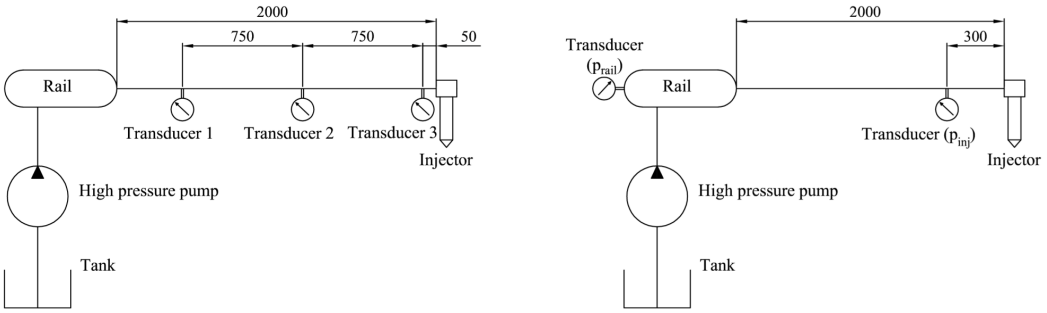

Figure 6.1: Layout of the injection systems.

The experimental campaign involved single injections over the 400-1600 bar of nominal pressure p_{nom} range and the ET has been selected in the range from 0.3 ms to 1.3 ms.

Pertaining to the layout presented in Fig. 6.1b, further tests have been carried out in order to measure the pressure at the injector inlet $p_{inj,in}$ trace and the rail pressure time history $p_{rail}(t)$. The latter, in unison with the current signal to the pilot stage, has been used as boundary condition to a 1D injection system diagnostic model, where the frequency dependent friction is taken into account.

6.2 Governing equations, mathematical and numerical models

The generalized Euler equations, written under the hypothesis of one-dimensional flow, have been applied to the pipe flow and the friction stress has been simulated as a source term. In this analysis, the thermal effects due to the fluid compressibility have been neglected, therefore the flow evolution has been considered as isothermal. The system of equations is composed by the continuity equation, the momentum balance equation and the state equation

of the flow, expressed by means of the speed of sound:

$$\begin{cases} \dfrac{\partial \rho}{\partial t} + \dfrac{\partial (\rho u)}{\partial x} = 0 \\ \dfrac{\partial (\rho u)}{\partial t} + \dfrac{\partial \left(p + \rho u^2\right)}{\partial x} = -\dfrac{4\tau_w}{d} \\ \dfrac{dp}{d\rho} = a_T^2 \end{cases} \tag{6.1}$$

where t stands for the time, x represents the spatial coordinate (along the pipe axis), ρ is the fluid density, u is the fluid velocity along x, p is the pressure, τ_w is the wall shear stress, d is the pipe internal diameter and a_T represents the isothermal speed of sound . The latter is obtained from the $a_T^2 = E_{b,T}/\rho$ formula, where $E_{b,T} = E_{b,T}(p,T)$ represents the isothermal bulk modulus, measured as a function of pressure and temperature for the used calibration fluid. The entrained gas effect on the speed of sound evaluation is considered in the experimental date used in the a_T evaluation. The diameter to wall thickness ratio is around 2.5, hence it is low enough to neglect the effect of the pipe stiffness on the sound speed value [147].

By means of the Riemann decoupling procedure, the continuity and the momentum balance equations can be transformed into the following system [138]:

$$\begin{cases} \dfrac{\partial R_1}{\partial t} + \lambda_1 \dfrac{\partial R_1}{\partial x} = \dfrac{4\tau_w}{d} a_T \\ \dfrac{\partial R_2}{\partial t} + \lambda_2 \dfrac{\partial R_2}{\partial x} = -\dfrac{4\tau_w}{d} a_T \end{cases} \tag{6.2}$$

where R_1 and R_2 represent the Riemann variables, which are defines as :

$$\delta R_1 = \delta p - \rho a \delta u \qquad\qquad \delta R_2 = \delta p + \rho a \delta u \tag{6.3}$$

and λ_1 and λ_2 are the eigenvalues of the Euler equations, given by:

$$\lambda_1 = u - a_T \qquad\qquad \lambda_2 = u + a_T \tag{6.4}$$

The liquid flow can be considered as subsonic ($|u| < a_T$), therefore the first Riemann equation has been discretized by following a downwind scheme ($\lambda_1 < 0$), on the contrary, the second Riemann equation has been discretized by means of an upwind scheme ($\lambda_2 > 0$). The core of the 1D pipe model solves

the two equations presented in Eq. (6.2) by means of the abovementioned downwind/upwind approach, based on the eigenvalues sign:

$$\begin{cases} \dfrac{R_{1i}^{n+1} - R_{1i}^{n}}{\Delta t} + \lambda_{1i}^{n} \dfrac{R_{1i+1}^{n} - R_{1i}^{n}}{\Delta x} = \dfrac{4\tau_{wi}^{n}}{d} a_{Ti}^{n} \\ \dfrac{R_{2i}^{n+1} - R_{2i}^{n}}{\Delta t} + \lambda_{2i}^{n} \dfrac{R_{i}^{n} - R_{2i-1}^{n}}{\Delta x} = -\dfrac{4\tau_{wi}^{n}}{d} a_{Ti}^{n} \end{cases} \tag{6.5}$$

where i and n stand for the space and time indexes of the computational mesh, respectively. The downwind/upwind adopted scheme is of the first order accuracy with respect to both space and time. A second order accuracy scheme has been also applied without any appreciable change, due to the absence of discontinuities in the analysed cases. The numerical grid has been selected by means of the following procedure: the computational time step, namely Δt, is fixed and, consequently, the numerical space step, namely Δx, is obtained by applying the Courant, Friedrichs and Lewy (CFL) condition, by means of $\Delta x = C \cdot max(|\lambda_1|, |\lambda_2|) \cdot \Delta t$ (where C represents the Courant number, that is a positive constant lower than 1). The grid independency of the results has been proved and shown in Sect. 6.5. Furthermore, it has been verified that the biggest Δt value used in the simulations is able to capture all the physical oscillations featured by the pressure signals (it has been verified that the first 250 Hz of the Fourier spectrum contains more than 95% of the energy of pressure oscillations around the average value).

As far as the initial conditions are concerned, they have been defined in terms of velocity (flow at rest) and pressure (a constant pressure value has been set along the pipe, equals to the average value of the experimental trace). The consistent number of boundary conditions has been obtained referring to the theory of the characteristic lines, as is usual for hyperbolic problems involving liquid flows: pertaining to the left boundary, the Riemann variable δR_1, related to the negative eigenvalue λ_1, conveys one information from the internal domain, therefore, only one boundary condition is required, that is the experimental pressure trace measured by means of the Transducer 1 (cf. Fig. 6.1a). Similarly, at the right boundary, the Riemann variable δR_2, related to the positive eigenvalue λ_2, is able to fully define the flow state at the boundary if it is coupled with the pressure time history from the Transducer 3 (cf. Fig. 6.1a). Two pressure signals have been selected as mechanical conditions imposed to

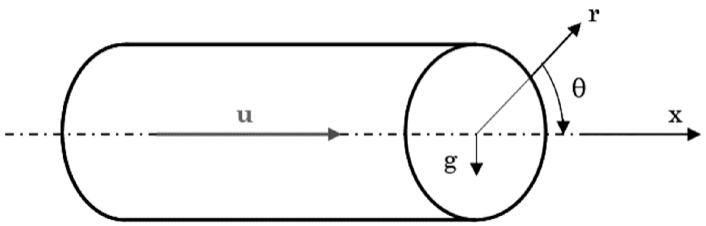

Figure 6.2: Pipe portion analysed for the Zielke model derivation.

the boundaries due to the difficulty to measure instantaneous flow velocities or flow-rates of an high-pressure flow featuring transients [92].

6.3 Review of Zielke's unsteady friction model

The first mathematical model to deal the unsteady friction is Zielke's one [148]. In this model, the steady-state friction term, for example the one obtained by means of the Darcy-Weisbach formula, is summed with an additional unsteady term based on a convolution integral of the velocity time history, properly weighted by means of a weight function. Zielke's experimental campaign was based on a reservoir connected to a quick closing valve by means of a copper tube. The pressure fluctuations triggered by the instantaneous closure of the valve have been measured along the pipe at two different locations, by means of two transducers. These experimental traces have been compared with the numerical results.

In Zielke's approach, the flow is axisymmetric [148], in Fig. 6.2 a portion of the pipe is reported: x represents the axial coordinate along the pipe, θ is the angular coordinate (the pipe axis is orthogonal to the gravity vector direction), g is the gravitational acceleration and r stands for the radial coordinate.

The Navier-Stokes equations for an incompressible laminar flow can be written for the pipe portion reported in Fig. 6.2:

$$\begin{cases} \dfrac{\partial u}{\partial x} = 0 \\ 0 = -\dfrac{\partial p}{\partial r} + \rho g_r \\ 0 = -\dfrac{1}{r}\dfrac{\partial p}{\partial \theta} + \rho g_\theta \\ \rho \dfrac{\partial u}{\partial t} = -\dfrac{\partial p}{\partial x} + \mu \left[\dfrac{1}{r}\dfrac{\partial}{\partial r}\left(r \dfrac{\partial u}{\partial r} \right) \right] \end{cases} \tag{6.6}$$

As can be inferred, the pressure follows an hydrostatic distribution over the pipe section. The flow velocity distribution can be evaluated through the latter equation, where u depends on the radial coordinate r and on the time t. This equation can be expanded and divided by the dynamic viscosity $\mu = \rho\nu$ (where ν stands for the kinematic viscosity), and one obtains:

$$\frac{\partial^2 u}{\partial r^2} + \frac{1}{r}\frac{\partial u}{\partial r} - \frac{1}{\nu}\frac{\partial u}{\partial t} = \frac{1}{\rho\nu}\frac{\partial p}{\partial x} \tag{6.7}$$

By introducing the function F as:

$$F = \frac{1}{\rho}\frac{\partial p}{\partial x} \tag{6.8}$$

Eq. (6.7) can be converted in the Laplace domain, one obtains [148]:

$$\frac{d^2 \hat{u}}{dr^2} + \frac{1}{r}\frac{d\hat{u}}{dr} - \frac{s}{\nu}\hat{u} = \frac{1}{\nu}\hat{F} \tag{6.9}$$

where $\hat{u}$ and $\hat{F}$ represent the Laplace transforms of $u(r,t)$ and $F(t)$, respectively, and s stands for the Laplace complex variable. It has been assumed that $F(t)$ is a continuous piecewise function and that the real part of s is higher than zero. Therefore, the integral $\hat{F}(s) = \int_0^\infty F(t)e^{-st}dt$ exists.

The solution $\hat{u}(r,s)$ to Eq. (6.9) can be expressed as the sum of the particular integral and of the general solution of the related homogeneous equation. The latter, for Eq. (6.9), is defined by means of zero-order Bessel functions of the first and second type, J and Y, respectively [149]. Concerning to the particular integral, this can be obtained by imposing that, at the end of the initial transient, the nature of the solution is the same of the source term one, namely $\hat{F}/\nu$, which is not dependent of r, in the considered case. Finally, the

complete solution of Eq. (6.9) is [148]:

$$\hat{u} = c_1 J_0\left(i\sqrt{\frac{s}{\nu}}r\right) + c_2 Y_0\left(i\sqrt{\frac{s}{\nu}}r\right) - \frac{1}{s}\hat{F} \tag{6.10}$$

where i is the complex variable. Constants c_1 and c_2 are obtained by imposing a finite value of $\hat{u}$ when $r = 0$, leading to $c_2 = 0$ and that $\hat{u} = 0$ when $r = d/2$. Eq. (6.10) becomes:

$$\hat{u}(r,s) = \frac{1}{s}\hat{F}\left[\frac{J_0\left(i\sqrt{\frac{s}{\nu}}r\right)}{J_0\left(i\sqrt{\frac{s}{\nu}}\frac{d}{2}\right)} - 1\right] \tag{6.11}$$

Hence, the wall shear stress can be obtained by means of its definition:

$$\hat{\tau}_w(s) = -\rho\nu\left.\frac{\partial\hat{u}}{\partial r}\right|_{r=\frac{d}{2}} = -\rho\hat{F}\frac{d}{2}\left[\frac{1}{\mathcal{J}_1\left(i\sqrt{\frac{s}{\nu}}\frac{d}{2}\right)}\right] \tag{6.12}$$

where $\mathcal{J}_1 = zJ_0(z)/J_1(z)$ represents the modified ratio of the zero and the first-order Bessel functions of the first type (where z stands for a generic complex number). The ratio between $\hat{\tau}_w$ and the flow velocity (averaged on the section) Laplace transform $\hat{U}$ can be written as:

$$\frac{\hat{\tau}_w}{\hat{U}} = \frac{\rho\frac{d}{2}s}{\mathcal{J}_1\left(i\sqrt{\frac{s}{\nu}}\frac{d}{2}\right) - 2} \tag{6.13}$$

In Eq. (6.13), the Laplace transform $\hat{U}$ can be expressed as:

$$\hat{U}(s) = \frac{2}{\left(\frac{d}{2}\right)^2}\int_0^{d/2} r\hat{u}dr = \frac{\hat{F}}{s}\left[\frac{2}{\mathcal{J}_1\left(i\sqrt{\frac{s}{\nu}}\frac{d}{2}\right)} - 1\right] \tag{6.14}$$

Generally, every Laplace transform must be equal to zero when $s \to \infty$, hence, $\lim_{s\to\infty}\hat{F} = 0$. By considering that, from $\mathcal{J}_1$ definition [149], $\lim_{z\to\infty}\mathcal{J}_1(z) = \lim_{z\to\infty} z = +\infty$, it can be inferred that $\lim_{s\to\infty}\hat{U} = 0$. From Eq. (6.12), one has $\lim_{s\to\infty}\hat{\tau}_w(s) = 0$, but the ratio $\hat{\tau}_w/\hat{U}$ approaches a finite value for $s \to \infty$. In order to guarantee that the Laplace transform $\hat{\tau}_w/\hat{U}$ approaches zero when $s \to \infty$, the Laplace transform of $\partial u/\partial t$, namely $\widehat{\partial U/\partial t} = s \cdot \hat{U}$, where $\hat{U}$ is defined by means of Eq. (6.14), is introduced (for $t = 0$, one has $U = 0$), and

one obtains:

$$\hat{\tau}_w(s) = \frac{\rho\frac{d}{2}}{\mathcal{J}_1\left(i\sqrt{\frac{s}{\nu}}\frac{d}{2}\right) - 2}\widehat{\frac{\partial U}{\partial t}}(s) \tag{6.15}$$

For $s \to \infty$, $\widehat{\partial U/\partial t}$ approaches zero; in addition, $\lim_{s\to\infty} \hat{\tau}_w/(\widehat{\partial U/\partial t}) = 0$. By anti-transforming Eq. (6.15), the Zielke expression to evaluate τ_w is achieved:

$$\tau_w(t) = \frac{8\rho\nu}{d}u(t) + \frac{4\rho\nu}{d}\int_0^t \frac{\partial u}{\partial t}(\eta)W(t-\eta)d\eta \tag{6.16}$$

where W represents a weight function and η is a time variable used in the integration. As can be inferred from Eq. (6.16), two different contributions can be distinguished: the first one is related to the steady-state friction term, the second one is a function of the speed time history of the previous time instants, hence, it can be considered as a flow memory term. If the steady-state contribution is expressed by means of the Darcy-Weisbach expression, Eq. (6.16) can be rewritten as:

$$\tau_w(t) = \lambda\rho|u|\frac{u(t)}{8} + \frac{4\rho\nu}{d}\int_0^t \frac{\partial u}{\partial t}(\eta)W(t-\eta)d\eta \tag{6.17}$$

where λ represents the friction factor evaluated by means of the Colebrook-White formula. Furthermore, for a laminar flow $\lambda = 64/Re$ and Eq. (6.16) can be obtained. Pertaining to the unsteady contribution, Zielke proposed two expression to define $W(\tau)$, where τ represents a dimensionless time ($\tau = (4\nu/d^2)t$):

$$\begin{cases} W(\tau) &= \left(e^{-26.2744\tau} + e^{-70.8493\tau} + e^{-218.9216\tau} + \right. \\ & \left. + e^{-322.5544\tau}\right) \text{ if } \tau > 0.02 \\ W(\tau) &= \left(0.282095\tau - 1.25 + 1.057855\tau^{0.5} + 0.9375\tau + \right. \\ & \left. + 0.396696\tau^{1.5} - 0.351563\tau^2\right) \text{ if } \tau < 0.02 \end{cases} \tag{6.18}$$

The first expression in Eq. (6.18) is obtained by means of the residue theorem [148] and the second one by expanding Eq. (6.13) as a polynomial series for large values of s, in fact when s approaches ∞ means that t approaches zero. In Fig. 6.3 the Zielke weight function is represented as a function of τ, based on Eq. (6.18).

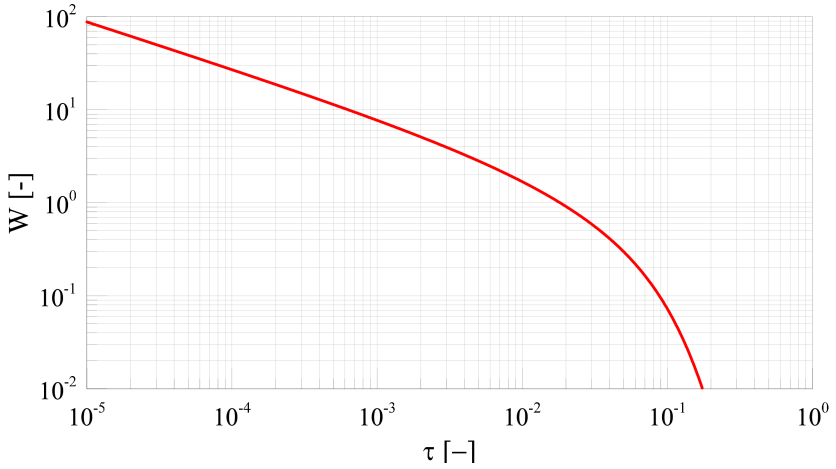

Figure 6.3: Zielke's weight function.

In order to solve the Riemann equation when the implemented friction model is based on Eqs. (6.17) and (6.18), very high computational efforts are required, leading to around 30 hours to carry out one simulation for the layout in Fig. 6.1a. A workstation equipped with a Intel Core i7-4770 CPU (3.40 GHz) featuring 32 GB of RAM memory has been used. Great efforts have been made to mitigate this problem, in fact, different simplified models able to consider both the friction contributions presented in Eq. (6.17) have been developed. The core of these simplified models is a different definition of the weight function and a different approach to solve the convolution integral. An approximated Zielke's weight function, given by three exponential terms obtained through the least square method, has been proposed by Trikha [150]; Kagawa employed ten exponential terms to define an interpolation of the Zielke $W(\tau)$ [151]. Finally, another approximation has been performed by Schohl, using five exponential terms evaluated with a nonlinear least square approach [152]. The abovementioned models take into account a laminar flow.

Different models have been developed in order to take into account the turbulent flow condition into the evaluation of the unsteady friction contribution, by means of the Reynolds number. One of it has been developed by Edge [153]. Vardy and Brown [77, 154] have considered a two-region model to analyse the cylindrical pipe flow: the turbulent viscosity increases with the distance from the pipe walls, reaching an asymptotic value in the inner region, near the pipe axis. All these improvements to the Zielke laminar approach in the

unsteady friction modelling can be considered a result of the notable evolution in computers performances.

6.4 Approximate methods for the evaluation of the unsteady friction

All the simplified methods have been developed to reduce the computational time to evaluate the convolution integral in Eq. (6.17). The approximate weight function W_{app} is defined with a truncated exponential series as:

$$W(\tau) \approx W_{app}(\tau) = \sum_{k=1}^{M} m_k e^{-n_k \tau} \tag{6.19}$$

where m_k and n_k represent the weight function fitting coefficients, while M is an integer number higher than one. The exponential fitting function y_k is then introduced:

$$y_k(t) = \int_0^t \frac{\partial u}{\partial t}(\eta) m_k e^{-n_k (t-\eta)\frac{4\nu}{d^2}} d\eta \tag{6.20}$$

Hence, the unsteady friction component $\tau_{w,u}$ can be written as [150]:

$$\tau_{w,u}(t) = \frac{4\rho\nu}{d} \sum_{k=2}^{M} y_k \tag{6.21}$$

6.4.1 Review of laminar flow models

Trikha's model

In this model, the weight function is defined by means of three exponential terms ($M = 3$). Values of m_k and n_k are obtained by imposing three different conditions [150]:

$$\begin{aligned} &i. \quad \int_0^\infty W_{app}(\tau) d(\tau) = \int_0^\infty W(\tau) d\tau \\ &ii. \quad W_{app}(\tau) = W(\tau) \quad \text{for} \quad \tau \approx 0.0001,\ 0.001,\ 0.01 \\ &iii. \quad \left| \frac{W_{app}(\tau) - W(\tau)}{W(\tau)} \right| < 0.02 \quad \text{for} \quad \tau > 0.1 \end{aligned} \tag{6.22}$$

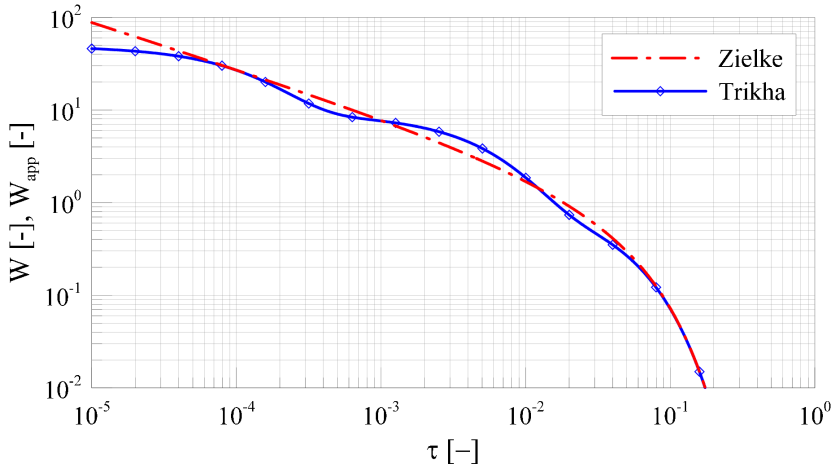

Figure 6.4: Trikha's and Zielke's weight functions.

For the $\tau > 0.02$ case, the condition *iii* results to by satisfied by the first exponential term at the right side of Eq. (6.18), leading to the determination of m_1 an n_1. By means of the conditions *i* and *ii* four other unknowns can be obtained, namely m_2, n_2, m_3 and n_3. The values of Trikha's model coefficients are reported in Table 6.1. The Trikha weight function is compared in Fig. 6.4 with the Zielke $W(\tau)$. Trikha's W_{app} well approximate $W(\tau)$ if $\tau > 5 \cdot 10^{-5}$.

When the W_{app} coefficients have been obtained, the quantity $y_k(t+\Delta t)$, defined by means of Eq. (6.20), can be written:

$$\begin{aligned} y_k(t+\Delta t) = & \int_0^{t+\Delta t} \frac{\partial u}{\partial t}(\eta) m_k e^{-n_k(t+\Delta t-\eta)\frac{4\nu}{d^2}} d\eta = \\ = & \int_0^{t} \frac{\partial u}{\partial t}(\eta) m_k e^{-n_k(t-\eta)\frac{4\nu}{d^2}} + \\ + & \int_0^{t} \frac{\partial u}{\partial t}(\eta) \left[m_k e^{-n_k(t+\Delta t-\eta)\frac{4\nu}{d^2}} - m_k e^{-n_k(t-\eta)\frac{4\nu}{d^2}} \right] d\eta + \\ + & \int_0^{t+\Delta t} \frac{\partial u}{\partial t}(\eta) m_k e^{-n_k(t+\Delta t-\eta)\frac{4\nu}{d^2}} d\eta \end{aligned} \tag{6.23}$$

Table 6.1: Trikha's approximate weight function coefficients.

k	m_k	n_k
1	1	26.4
2	8.1	200
3	40	8000

After some analytical steps, the presented recursive expression can be obtained:

$$y_k(t+\Delta t) = y_k(t)e^{-n_k \Delta t \frac{4\nu}{d^2}} + m_k\left[u(t+\Delta t) - u(t)\right] \tag{6.24}$$

where $y_k(0) = 0$. As can be inferred from Eq. (6.24), in this method it is possible to evaluate the unsteady friction pertaining to the time instant $t+\Delta t$ only by using the information referring to time instant t.

Kagawa's model

In this model, the W_{app} is obtained starting from the prevailing W exponential term for $\tau > 0.02$ in Eq. (6.18), with $m_1 = 1$ and $n_1 = 26.3744$. The function $W_{app,1}(\tau) = m_1 e^{-n_1 \tau}$ results to be accurate in the approximation of the Zielke weight function up to $\tau_1 = 0.062$. By evaluating the difference between $W(\tau)$ and $W_{app,1}(\tau)$ a straight line in a semi-logarithmic plot, till $\tau_2 = 0.028 < \tau_1$, is obtained; therefore, a new exponential term can be obtained by means of an exponential regression and added to $W_{app,1}(\tau)$ in order to obtain a good approximation $W_{app,2}$ of $W(\tau)$ till the τ_2 value. This general criterion is applied:

$$\left|\frac{W_{app,k}(\tau) - W(\tau)}{W(\tau)}\right| < 0.01 \quad \text{for } \tau > \tau_k \tag{6.25}$$

Kagawa's weight function is composed by ten exponential terms, which values of m_k and n_k are reported in Table 6.2. Kagawa's approximated weight function is reported in Fig. 6.5, it results to be a good estimation of $W(\tau)$ if $\tau > 7 \cdot 10^{-6}$ (to improve the accuracy, more exponential terms can be added).

Table 6.2: Kagawa's approximate weight function coefficients.

k	m_k	n_k	k	m_k	n_k
1	26.3744	1	**6**	$4.6181 \cdot 10^3$	11.6761
2	72.8033	1.16725	**7**	$1.36011 \cdot 10^4$	20.0612
3	$1.87424 \cdot 10^2$	2.20064	**8**	$4.00825 \cdot 10^4$	34.4541
4	$5.36626 \cdot 10^2$	3.92861	**9**	$1.18153 \cdot 10^5$	59.1642
5	$1.57060 \cdot 10^3$	6.78788	**10**	$3.48316 \cdot 10^5$	$1.01590 \cdot 10^2$

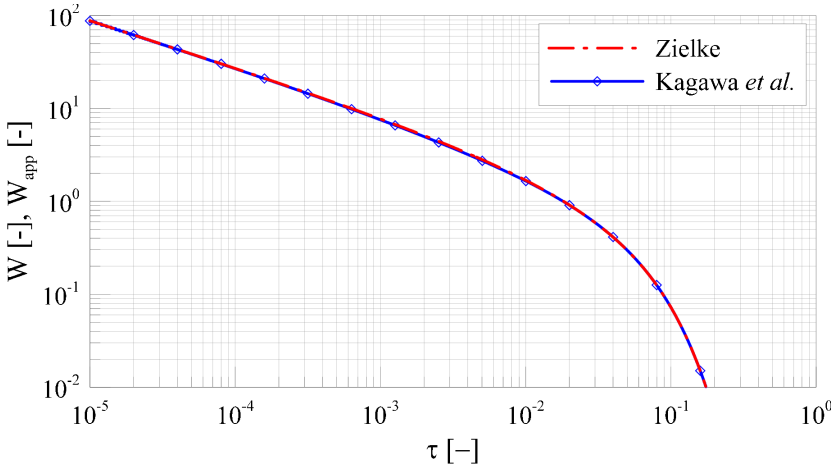

Figure 6.5: Kagawa's and Zielke's weight functions.

Pertaining to the quantity $y_k(t+\Delta t)$, it is developed as follows:

$$\begin{aligned} y_k(t+\Delta t) = & \int_0^{t+\Delta t} \frac{\partial u}{\partial t}(\eta) m_k e^{-n_k(t+\Delta t-\eta)\frac{4\nu}{d^2}} d\eta = \\ = & \int_0^{t} \frac{\partial u}{\partial t}(\eta) m_k e^{-n_k(t+\Delta t-\eta)\frac{4\nu}{d^2}} + \\ + & \int_t^{t+\Delta t} \frac{\partial u}{\partial t}(\eta) m_k e^{-n_k(t+\Delta t-\eta)\frac{4\nu}{d^2}} d\eta \end{aligned} \tag{6.26}$$

by rearranging the right side of Eq. (6.26), one has :

$$y_k(t+\Delta t) = y_k(t) e^{-n_k \Delta t \frac{4\nu}{d^2}} + [u(t+\Delta t) - u(t)]\, m_k e^{-n_k \frac{4\nu}{d^2}\Delta t/2} \tag{6.27}$$

with $y_k(0) = 0$.

Schohl's method

This method [152] involves five exponential terms, obtained by fitting $W(\tau)$. A least square technique has been employed to minimize the following function, that is a sum of percentage errors:

$$\sum_{m=1}^{N} \left(\frac{W_{app}(\tau_m) - W(\tau_m)}{W(\tau_m)} \right)^2 \tag{6.28}$$

where $N = 143$ and all the points are in the range $10^{-5} \leq \tau \leq 0.20$ [152]. The obtained W_{app} is reported in Fig. 6.6, in comparison with Zielke's weight

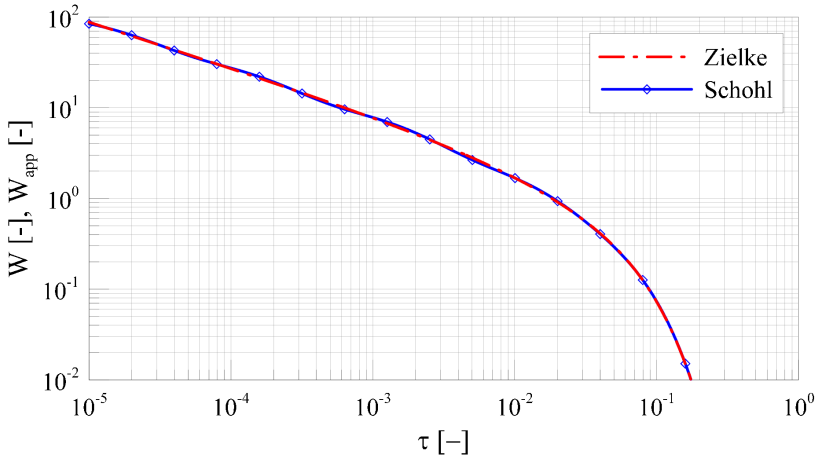

Figure 6.6: Schohl's and Zielke's weight functions.

function. As can be seen, the approximation holds for $\tau > 1 \cdot 10^{-5}$. Values of m_k and n_k are reported in Table 6.3.

The convolution integral is managed as follows:

$$\begin{aligned} y_k(t+\Delta t) = & \int_0^{t+\Delta t} \frac{\partial u}{\partial t}(\eta) m_k e^{-n_k(t+\Delta t-\eta)\frac{4\nu}{d^2}} d\eta = \\ = & \; e^{-n_k \Delta t \frac{4\nu}{d^2}} \int_0^t \frac{\partial u}{\partial t}(\eta) m_k e^{-n_k(t-\eta)\frac{4\nu}{d^2}} + \\ + & \; m_k e^{-n_k(t+\Delta t)\frac{4\nu}{d^2}} \int_t^{t+\Delta t} \frac{\partial u}{\partial t}(\eta) e^{n_k \eta \frac{4\nu}{d^2}} d\eta \\ = & \; e^{-n_k \Delta t \frac{4\nu}{d^2}} y_k(t) + \Delta y_k(t) \end{aligned} \tag{6.29}$$

Table 6.3: Schohl's approximate weight function coefficients.

k	m_k	n_k
1	1.051	26.65
2	2.358	100
3	9.021	669.6
4	29.47	6497
5	79.75	57990

From which, one has:

$$y_k(t+\Delta t) = e^{-n_k \Delta t \frac{4\nu}{d^2}} y_k(t) + \frac{1 - e^{-n_k \Delta t \frac{4\nu}{d^2}}}{n_k \Delta t \frac{4\nu}{d^2}} [u(t+\Delta t) - u(t)] \tag{6.30}$$

with $y_k(0) = 0$.

6.4.2 Review of turbulent flow models

Edge's model

In order to consider the effect of turbulence on the unsteady friction term, the dependence of the Reynolds number on the friction factor λ is taken into account. Preliminarily, Eq. (6.16) is rearranged as:

$$\tau_w(t) = \frac{8\rho\nu}{d} u(t) + \frac{1}{2} \int_0^t \frac{\partial}{\partial t} \left(\frac{8\rho\nu}{d} u(\eta) \right) W(t-\eta) d\eta \tag{6.31}$$

then, the following formula, based on the Darcy-Weisbach friction coefficient, has been proposed in order to obtain a formulation of Eq. (6.31) extended to turbulent flows:

$$\tau_w(t) = \lambda\rho|u(t)|\frac{u(t)}{8} + \frac{1}{2} \int_0^t \frac{\partial}{\partial t} \left(\lambda\rho|u(t)|\frac{u(t)}{8} \right) W(t-\eta) d\eta \tag{6.32}$$

By introducing the steady-state friction term $\tau_{w,st}$, Eq. (6.32) is rearranged as [153]:

$$\tau_w(t) = \tau_{w,st} + \frac{1}{2} \int_0^t \frac{\partial \tau_{w,st}}{\partial t}(\eta) W(t-\eta) d\eta \tag{6.33}$$

In this approach, the second term is discretized by using the same procedure presented in [151]:

$$\tau_{w,u}(t) = \frac{1}{2} \sum_{k=1}^{M} z_k \tag{6.34}$$

where $z_k(t+\Delta t)$ is expressed similarly to Eq. (6.27) for $y_k(t+\Delta t)$ [153]:

$$z_k(t+\Delta t) = z_k(t) e^{-n_k \Delta t \frac{4\nu}{d^2}} + [\tau_{w,st}(t+\Delta t) + \tau_{w,st}(t)] m_k e^{-n_k \Delta t/2 \frac{4\nu}{d^2}} \tag{6.35}$$

with $z_k(0) = 0$. Coefficients to define W_{app} are the same as those in Table 6.2.

A modified version of the Kagawa model

In this model, the flow regime dependence of the frequency dependent friction on the Reynolds number Re is considered by means of a coefficient δ, defined as [31]:

$$\delta = \frac{\lambda}{\lambda_{lam}} \tag{6.36}$$

The coefficient δ, as can be inferred from Eq. (6.36), is defined as the ratio of the Darcy-Weysbach friction coefficient λ to the one referred to a laminar flow λ_{lam}, evaluated with the same Reynolds number. For a turbulent flow ($Re > 2000$), λ_{lam} is calculated by extrapolating the laminar law $\lambda = 64/Re$. Therefore, the frequency dependent friction shear stress contribution can be calculated as:

$$\tau_{w,u}(t) = \delta \frac{4\rho\nu}{d} \int_0^t \frac{\partial u}{\partial t}(\eta) W(t-\eta) d\eta \tag{6.37}$$

In other words, the frequency dependent friction term, holds for a laminar flow, is scaled to a turbulent flow by means of the coefficient δ. This empirical approach, that represents a variant of the Edge method, results to be valid only in the first part of the transition region, in fact δ loses its physical meaning when Re becomes too large.

Vardy and Brown's model

In this model [77, 154], the weigh function is evaluated as a function of Re. In detail, the model is based on the turbulent kinematic viscosity, namely the eddy viscosity, a flow property introduced to solve the Reynolds Averaged Navier-Stokes equations for turbulence, in accordance to the Boussinesq approach. Basic hypotheses of this model are the following, with reference to Fig. 6.7: the sum ν_{tot} of the molecular viscosity and eddy viscosity is distributed along the radial coordinate of the pipe y by following a piecewise linear trend inside the outer zone of the cross section, namely the annulus region; whereas, ν_{tot} keeps a constant value equals to ν_{core} in the inner zone, namely the core. Furthermore, ν_{tot} is not a function of the time.

As can be inferred, ν_{tot} varies linearly from the viscosity value at the wall, namely $\nu(y=0)$, to v_{core} in the core region [154]:

$$\begin{cases} \text{annulus region}: & \nu_{tot} = \nu(1+\alpha y) \quad \text{when } 0 < y < 0.1d \equiv b \\ \text{core region}: & \nu_{tot} = \nu_{core} = 0.065\sqrt{\frac{\tau_w}{\rho}}\frac{d}{2} \end{cases} \tag{6.38}$$

where b represents the annulus thickness and α is a variable defined as follows:

$$\alpha = \frac{\nu_{core} - \nu}{b\nu} \tag{6.39}$$

The Navier-Stokes equation along the component u, inside the core region, can be written as:

$$\frac{\partial u}{\partial t} = -\frac{1}{\rho}\frac{\partial p}{\partial x} + \nu_{core}\left[\frac{1}{r}\frac{\partial}{\partial r}\left(r\frac{\partial u}{\partial r}\right)\right] \tag{6.40}$$

while the expression holds in the annular region ($y = d/2 - r$) is:

$$\frac{\partial u}{\partial t} = -\frac{1}{\rho}\frac{\partial p}{\partial x} + \frac{\partial}{\partial y}\left[\nu(1+\alpha y)\frac{\partial u}{\partial y}\right] \tag{6.41}$$

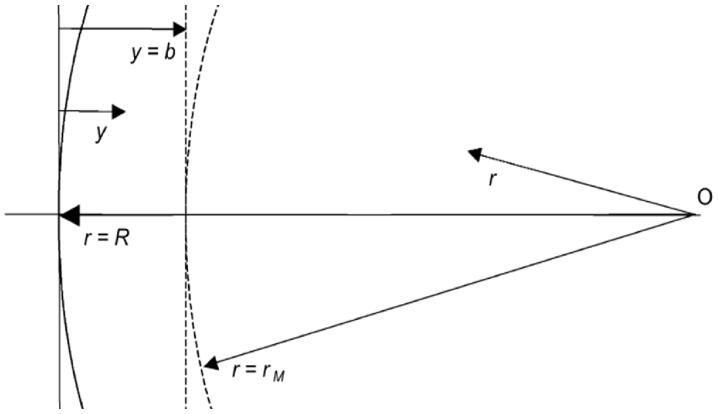

Figure 6.7: Pipe geometrical description in Vardy and Brown's model.

The Laplace transform of Eqs. (6.40) and (6.41) can be expressed as:

$$\begin{cases} \hat{u}(\eta,s) = & [c_1 I_0(\eta) + c_2 K_0(\eta) - 1]\,\dfrac{1}{s\rho}\left(\dfrac{\partial \hat{p}}{\partial x}\right) & \text{(annulus)} \\ \hat{u}(\eta,s) = & \left(\dfrac{(1+H) I_0\left(r\sqrt{s/\nu_{core}}\right)}{I_0\left(r_M\sqrt{s/\nu_{core}}\right)}\right)\dfrac{1}{s\rho}\left(\dfrac{\partial \hat{p}}{\partial x}\right) & \text{(core)} \end{cases} \tag{6.42}$$

where a new variable $\eta(y,s) = 2\sqrt{s[1+\alpha y]/\nu}/\alpha$ has been introduced for the annular region. The solutions reported in Eq. (6.42) are obtained by means of a modified Bessel equation and by imposing that the value of the shear stress is equal at the boundary between the core and annulus regions. I_0 and K_0 represent the modified zero order Bessel functions of the first and second kinds [149], c_1 and c_2 are constants of integration, and H is a parameter which correlates the pressure gradient to the velocity at the interface between the two considered zones. Generally, the unsteady term of the wall shear stress can be written as:

$$\tau_{w,u} = \tau_w - \tau_{w,st} \tag{6.43}$$

where τ_w is expressed as:

$$\tau_w = \rho\nu\left(\frac{\partial u}{\partial y}\right)_w \tag{6.44}$$

The Laplace transform of τ_w can be obtained by the differentiation of the first expression in Eq. (6.42), while the Laplace transform of the steady-state friction term contribution $\hat{\tau}_{w,st}$ is obtained by evaluating $\lim_{s\to 0}\hat{\tau}_w$. Therefore, based on Eq. (6.43) and by introducing the section-averaged velocity $\hat{U}$, the Laplace transform of the unsteady friction term can be expressed as $\hat{\tau}_{w,u} = \hat{\tau}_w - \hat{\tau}_{w,st}$, and one obtains [31]:

$$\hat{\tau}_{w,u}(s) = \rho\nu\Phi_u\hat{U}(s) = \rho\nu\frac{\Phi_u}{s}\cdot s\cdot\hat{U}(s) = \rho\nu\Phi_u\widehat{\frac{\partial U}{\partial t}}(s) \tag{6.45}$$

$\Phi_u(s)$ represents, except for the quantity $\rho\nu$, a transfer function [154] between the Laplace transforms $\hat{\tau}_{w,u}$ and $\hat{U}$ or $\widehat{\partial U/\partial t}$. In addition, the Laplace transform of $\hat{\tau}_{w,u}$ can be expressed in terms of the Eq. (6.17):

$$\hat{\tau}_{w,u}(s) = \frac{4\rho\nu}{d}\widehat{W}\widehat{\frac{\partial U}{\partial t}}(s) \tag{6.46}$$

By comparing Eqs. (6.45) and (6.46), one has:

$$\widehat{W} = \frac{d}{4}\frac{\Phi_u}{s} \tag{6.47}$$

Finally, $\widehat{W}$ is substituted by means of the following approximation:

$$\widehat{W}_{app} = \frac{A}{\sqrt{s+B}} \tag{6.48}$$

where the dimensional coefficients A and B are obtained in order to let Φ_u/s have the correct asymptotic behaviour for $s \to 0$ and $s \to \infty$. By anti-transforming Eq. (6.48) in the time domain, one has [77]:

$$W_{app} = \frac{A^* e^{-\tau B^*}}{\sqrt{\tau}} \tag{6.49}$$

where the dimensionless coefficients A^* and B^* values, for a smooth-wall flow, are given by:

$$A^* = \frac{1}{2\sqrt{\pi}} \quad B^* = \frac{Re^k}{12.86} \quad k = \log_{10}\left(\frac{15.29}{Re^{0.0567}}\right) \tag{6.50}$$

When the characteristic roughness is not negligible, it can be seen that A^* and B^* coefficients are also a function of ε/d, where ε is the roughness size [77]. The B^* Reynolds function presented in Eq. (6.50) has been obtained by means of a regression analysis on a set of data of B^* determined for different Reynolds number in the $4000 < Re < 10^8$ range, for a smooth wall flow.

If W_{app}, defined by Eq. (6.49), is divided by its numerator (where is included the Re dependency of W_{app}), the scaled W^*_{app} function is obtained, which is expressed as a sum of different exponential term, in accordance to Eq. (6.19):

$$W^*_{app} = \frac{W_{app}}{A^* e^{-B^*\tau}} = \frac{1}{\sqrt{\tau}} \approx \sum_{k=1}^{M} \frac{m_k}{A^*} e^{-(n_k - B^*)\tau} = \sum k = 1^M m^*_k e^{-n^*_k \tau} \tag{6.51}$$

In order to guarantee the matching between the scaled W^*_{app} and the series of exponential terms, the ratio of consecutive values of τ where the comparison between W^*_{app} and the series is made, is $10^{0.5}$. Values of m^*_k and n^*_k, reported in Table 6.4, can be considered universal, in fact they are not dependent of Re. On the contrary, coefficients m_k and n_k are a function of Re and the relations

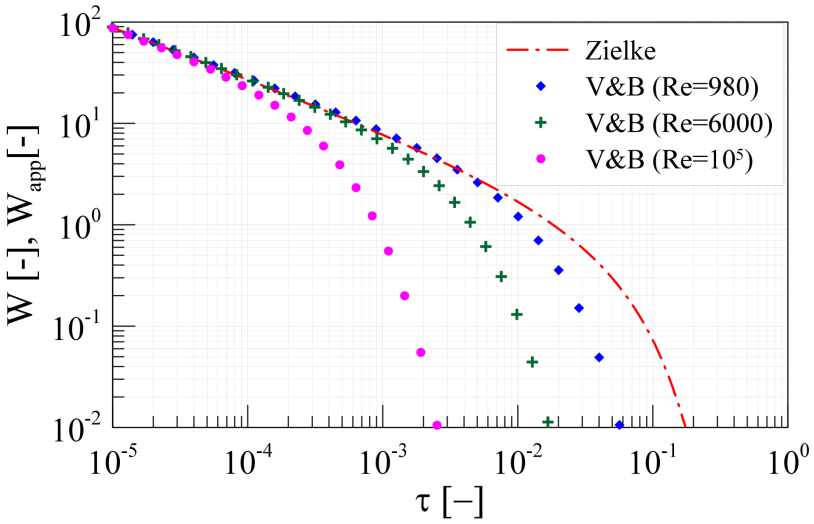

Figure 6.8: Vardy and Brown's weight functions for different Re values, compared with Zielke's $W(\tau)$.

to evaluate them are $m_k = A^* \cdot m_k^*$ and $n_k = n_k^* + B^*$. The abovementioned coefficients m_k and n_k are used in Eq. (6.19) to evaluate W_{app}, hence, the frequency dependent friction shear stress can be estimated for a turbulent flow through Eqs. (6.20) and (6.21). It has been observed that coefficients reported in Table 6.4 were verified in the Colebrook-White formula domain ($4000 < Re < 10^8$), but, by means of them, it is possible to obtain a satisfactory approximation of the Zielke function for $Re \approx 1000$ [77]. In Fig. 6.8 three different W_{app} evaluated by considering three different Re values have been reported and compared with Zielke's weight function. As can be inferred from Fig. 6.8, the higher the Reynolds number is, the shorter is the flow memory of the past events employed in the evaluation of $\tau_{w,u}$ at a certain time t (when Re augments, W crosses earlier the abscissa axis, cf. Fig. 6.8).

6.5 Comparison of the different unsteady friction models

Figures 6.9 and 6.10, referring to the layout shown in Fig. 6.1a, report the comparison between the experimental pressure traces (measured by means of the Transducer 2) and the numerical results pertaining to the different unsteady

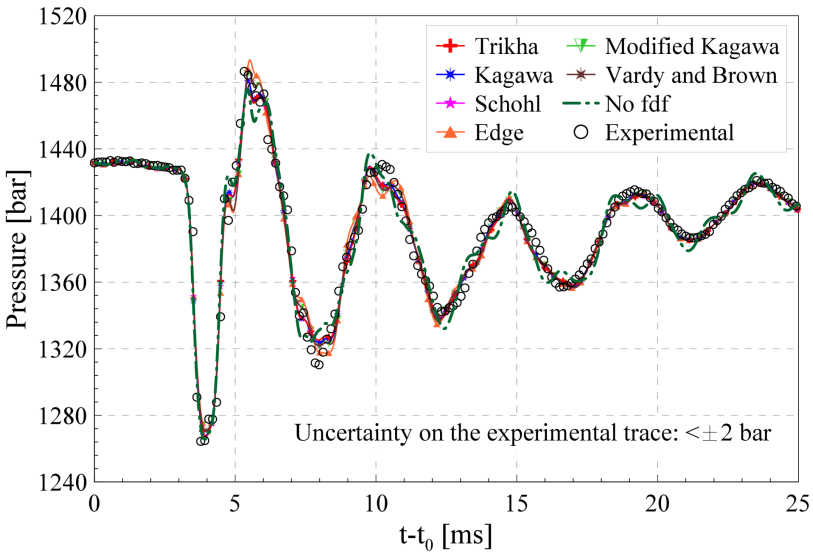

Figure 6.9: Pressure numerical results ($p_{nom} = 1400$ bar and $ET = 600$ μs).

friction models (both the laminar methods and the ones suitable for turbulent flows).

Figure 6.9 refers to $p_{nom} = 1400$ bar and $ET = 600$ μs, while Fig. 6.10 refers to $p_{nom} = 800$ bar and $ET = 1000$ μs, at which correspond a maximum Reynolds number of 6000 and 8500, respectively.

In Table 6.5 the computational times required for the different simulations are reported. As can be inferred, this time depends on the selected mesh size and obviously the higher the Δt is, the reduced is the time needed to complete a simulation. It must be taken into account that by halving the Δt, the computational time results to be fourfold, in fact both the time and space sizes of the mesh result to be doubled. The usual choice to face this

Table 6.4: Vardy and Brown's approximate weight function coefficients.

k	m_k^*	n_k^*	k	m_k^*	n_k^*
1	9.06	10	**7**	66	10^4
2	−4.05	$10^{1.5}$	**8**	114	$10^{4.5}$
3	12	10^2	**9**	210	10^5
4	8.05	$10^{2.5}$	**10**	337	$10^{5.5}$
5	22.7	10^3	**11**	829	10^6
6	35.1	$10^{3.5}$			

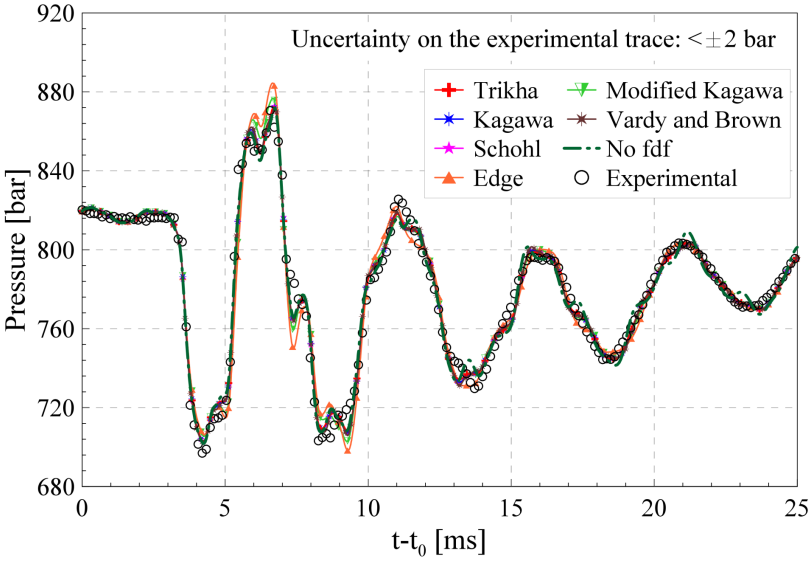

Figure 6.10: Pressure numerical results ($p_{nom} = 800$ bar and $ET = 1000$ μs).

Table 6.5: Computational time for simulations pertaining to the Fig. 6.1a layout.

Method	Δt [μs]	Computational time [s]
Zielke	2	$> 10^5$
Trikha	16	0.8
Kagawa	8	3.6
Schohl	8	3.5
Edge	8	3.5
Modified Kagawa	8	4.3
Vardy and Brown	2	60.3
No unsteady f.	8	3

kind of numerical problem is to establish the space step Δx based on the accuracy requirements and, by applying the CFL condition, the Δt is then evaluated. As has been shown in Sect. 6.4, the weight function approximation accuracy for the different methods depends on the dimensionless time τ, which is proportional to Δt. Therefore, in this work a suitable Δt has been chosen (in order to have the best approximation of $W(\tau)$) and, consequently, by means of the CFL condition, Δx is obtained.

Figure 6.11, which refers to a working condition with $p_{nom} = 600$ bar and $ET = 800$ μs for the layout presented in Fig. 6.1a, reports different numerical pressure time histories, obtained for different Δt values. In this case, only the

steady-state friction has been considered. Below $\Delta t = 30$ µs the pressure traces are almost overlapped, therefore a solution obtained with $\Delta t < 30$ µs can be considered as grid independent.

As can be seen in Figs. 6.9 and 6.10, the different numerical pressures pertaining to the different frequency dependent friction models tend to overlap. Furthermore, also the numerical results referring to the solution where only the steady-state friction is considered accurately match the experimental pressure data (p_{exp})

From Figs. 6.9 and 6.10, it results that the implementation of the frequency dependent friction model is not determinant when the provided boundary conditions are two pressure time histories (the numerical distributions tend to the solution obtained by means of the d'Alembert equation for the pressure, where two pressures at the boundaries are required). In fact, in this condition, the pressure signals of Transducer 1 and 3 imposed at the boundaries restore the right pressure values at the pipe extremities, and this results to be a compensation for the absence of the unsteady friction model, or hides the possible inaccuracy of a certain model. As a consequence, the numerical pressure trace obtained in correspondence of Transducer 2 can be satisfactorily predicted. However, a slight inaccuracy of the free pressure waves propagation can be noticed.

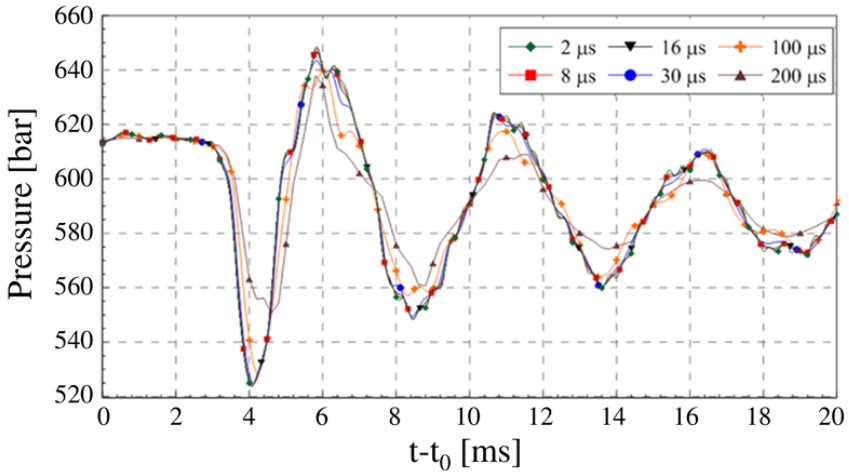

Figure 6.11: Numerical pressure traces for different Δt ($p_{nom} = 600$ bar and $ET = 800$ µs).

In Figs. 6.12 and 6.13 the numerical flow velocity time histories are reported, detected at the Transducer 2 location, pertaining to the same working conditions as those considered in Figs. 6.9 and 6.10, respectively. In these cases, appreciable differences can be noticed for the different frequency dependent friction models; however, since the experimental pressure traces are imposed as

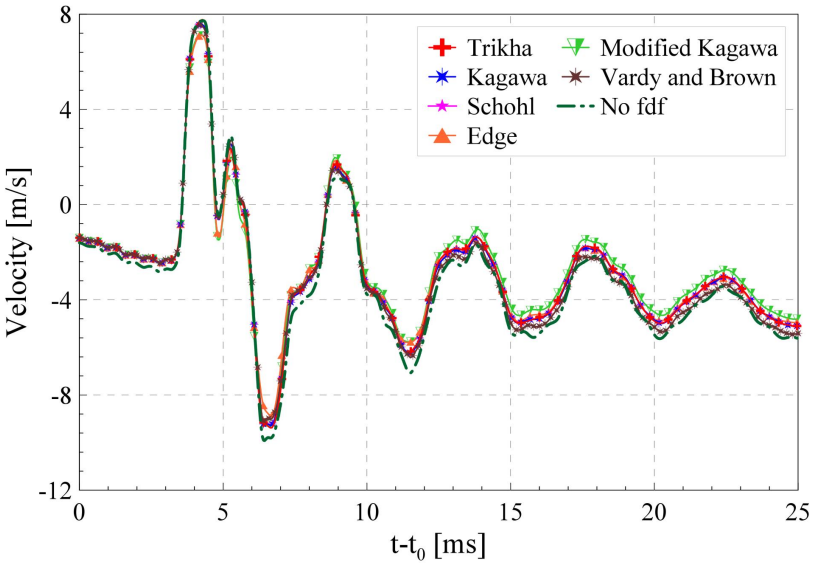

Figure 6.12: Numerical flow velocity field ($p_{nom} = 1400$ bar and $ET = 600$ μs).

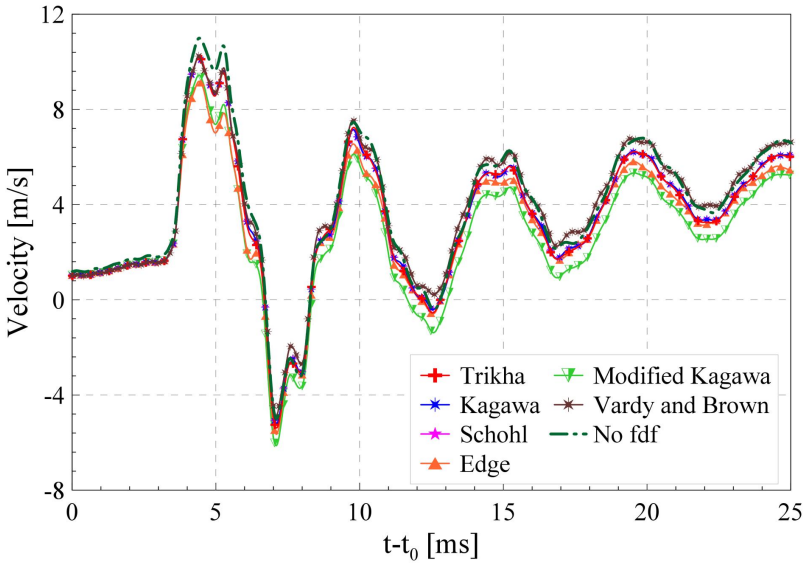

Figure 6.13: Numerical flow velocity field ($p_{nom} = 800$ bar and $ET = 1000$ μs).

boundary conditions, this may lead to a loss in accuracy in the flow velocity field simulation.

The experimental layout presented in Fig. 6.1b has been used for the comparison of the results referring to the different friction models. An already validated 1D diagnostic model of a Common Rail diesel injection system has been used [31], similar to the one presented in Sect. 2.4. Boundary conditions of the model are the current signal, measured by means of a clamp, provided to the injector pilot stage to trigger the injection event [70] and the rail pressure time history, measured by means of a piezoresistive transducer.

The different unsteady friction models have been implemented to the rail-to-injector pipe and in the internal injector drilled pipe, which connects the injector inlet to the nozzle.

Figures 6.14 and 6.15 show the comparison between the numerical pressure traces along the 2 m long injector feeding pipe, calculated at a distance of 300 mm from the injector inlet (cf. Fig. 6.1b) and the experimental one, pertaining to the working conditions with $p_{nom} = 800$ bar, $ET = 1000$ µs and $p_{nom} = 1200$ bar, $ET = 1000$ µs, respectively.

It is evident that the unsteady friction improves the quality of the numerical results, in fact it helps to correctly predict the frequency and the amplitude of the free pressure waves travelling forth and back along the injector feeding pipe,

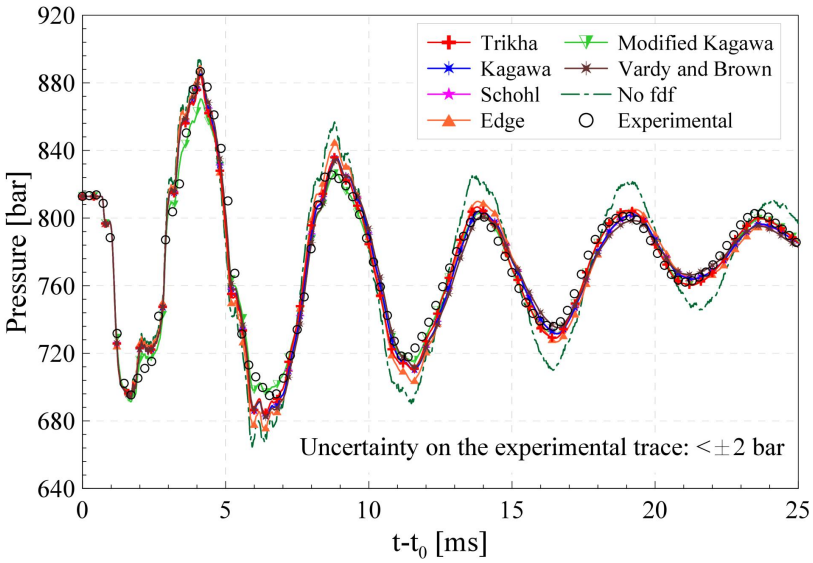

Figure 6.14: Numerical pressure time histories for different unsteady friction methods ($p_{nom} = 800$ bar and $ET = 1000$ µs).

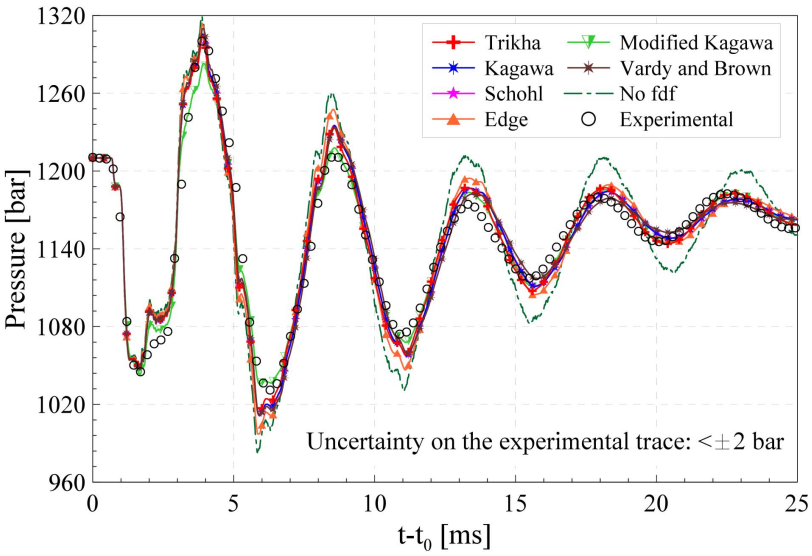

Figure 6.15: Numerical pressure time histories for different unsteady friction methods ($p_{nom} = 1200$ bar and $ET = 1000$ µs).

after the end of the injection. Contrarily to the setup presented in Fig. 6.1a, in this layout only one pressure signal (the p_{rail}) is provided as a boundary condition, hence the numerical pressures result to be more sensitive to the pressure wave propagation model accuracy. However, as can be inferred by Figs. 6.14 and 6.15, the choice of a specific unsteady friction model does not affect appreciably the numerical results.

In the considered working conditions, differences in the maximum and minimum velocity values between the approaches with and without the unsteady friction are below 1 m/s. Concerning to the working condition with $p_{nom} = 800$ bar, $ET = 1000$ µs, the maximum velocity value was around 9 m/s, instead for the point with $p_{nom} = 1200$ bar, $ET = 1000$ µs it was 11 m/s. For both these injections the maximum Reynolds number was below 10^4.

Fig. 6.16 reports the Fourier analysis of the signals presented in Fig. 6.15, performed only by considering the oscillations around the time averaged value, furthermore, the spectra have been normalized with respect to the maximum experimental pressure time history spectrum value. In accordance with the time-domain analysis of Fig. 6.15, the most representative wave pertaining to the steady-state friction simulation results to have an overestimated amplitude. Moreover, its frequency is reduced with respect to the unsteady friction spectra.

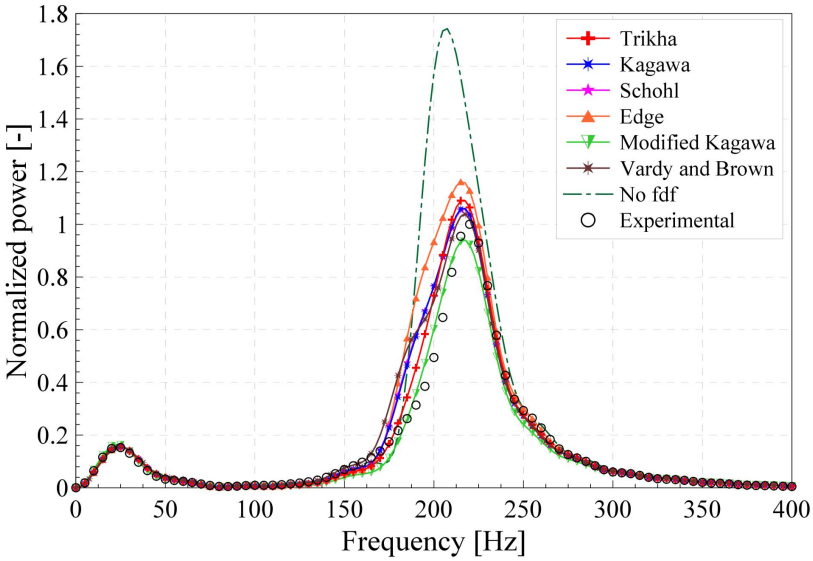

Figure 6.16: Fourier spectra of pressure time histories for different unsteady friction methods ($p_{nom} = 1200$ bar and $ET = 1000$ µs).

A quantitative comparison between the different numerical time histories has been performed by defining an index of performance (IP), defined by means of the experimental pressure trace (p_{exp}), the numerical simulation with ($p_{num,u}$) and without ($p_{num,wou}$) the unsteady friction:

$$IP = \frac{\left| \int_0^T |p_{num,u}(t) - p_{exp}(t)|\, dt - \int_0^T |p_{num,wou}(t) - p_{exp}(t)|\, dt \right|}{\int_0^T |p_{num,wou}(t) - p_{exp}(t)|\, dt} \cdot 100 \quad (6.52)$$

IP gives an idea of the improvement provided in the prediction of pressure transients by the implementation of a certain unsteady friction model. More accurate simulation results referred to a particular unsteady friction model, compared to the corresponding ones obtained with only the steady-state friction, lead to an higher value of the defined index. IP values referred to the working condition in Fig. 6.14 and 6.15 are shown in Table 6.6. As can be inferred, the unsteady friction helps to improve the simulation results appreciably. The Trikha method results to be the most efficient, in fact the IP value is high and the corresponding computational time is the lowest, compared to the other methods.

By taking into account the results of the benchmark established in Figs. 6.9-6.10 and 6.12-6.16 and in Tables 6.5-6.6, and based on additional tests

performed for other working conditions (in terms of ET and p_{nom}), Trikha's method is recommended for the simulation of transient flows in high-pressure pipes featuring an aspect ratio lower than 800 and Reynolds number below 10^4. The abovementioned range is able to cover many engineering applications in fluid-power systems.

Table 6.6: Values of IP for the injector diagnostic model simulations.

Method	Fig. 6.14	Fig. 6.15
Trikha	62.66%	62.66%
Kagawa	57.17%	57.35%
Schohl	56.84%	56.84%
Edge	40.57%	40.32%
Modified Kagawa	68.13%	71.32%
Vardy and Brown	55.80%	58.50%

Chapter 7

Polytropic approach in modelling 1D compressible flows

7.1 Analytical relations for polytropic flows

Generally, a polytropic process is governed by a link between the fluid pressure p and the density ρ by means of the polytropic exponent m :

$$\frac{dp}{p} - m\frac{d\rho}{\rho} = 0 \tag{7.1}$$

If a viscous steady-state flow in a constant cross-section pipe is considered, with the assumption of barotropic flow, the energy equation can be neglected. By following a procedure similar to the one introduced in the Fanno model, Eq. (7.1) is solved coupled with the perfect gas state equation (Eq. (7.2)), the continuity equation (Eq. (7.3)), the momentum balance equation (Eq. (7.4)), the definition of the isentropic Mach number Ma (Eq. (7.5)), the equations which define the isentropic stagnation pressure p_0 and isentropic stagnation temperature T_0 (Eq. (7.6) and Eq. (7.7)), the impulse function (Eq. (7.8)) and the entropy variation s between two points 1 and 2 (Eq. (7.9)), in their suitable differential forms [155]:

$$\frac{dp}{p} = \frac{d\rho}{\rho} + \frac{dT}{T} \tag{7.2}$$

$$\frac{d\rho}{\rho}+\frac{du^2}{2u^2}=0 \tag{7.3}$$

$$\frac{dp}{p}+\frac{\gamma Ma^2}{2}\frac{4fdx}{D}+\frac{\gamma Ma^2 du^2}{2u^2}=0 \tag{7.4}$$

$$\frac{dMa^2}{Ma^2}=\frac{du^2}{u^2}-\frac{dT}{T} \tag{7.5}$$

$$\frac{dp_0}{p_0}=\frac{dp}{p}+\frac{\gamma Ma^2}{2+(\gamma-1)\,Ma^2}\cdot\frac{dMa^2}{Ma^2} \tag{7.6}$$

$$\frac{dT_0}{T_0}=\frac{dT}{T}+\frac{(\gamma-1)Ma^2}{2+(\gamma-1)\,Ma^2}\cdot\frac{dMa^2}{Ma^2} \tag{7.7}$$

$$\frac{dJ}{J}=\frac{dp}{p}+\frac{\gamma Ma^2}{1+\gamma Ma^2}\cdot\frac{dMa^2}{Ma^2} \tag{7.8}$$

$$\frac{s_2-s_1}{c_p}=\ln\frac{T_{0,2}/T_{0,1}}{\left(p_{0,2}/p_{0,1}\right)^{\frac{\gamma-1}{\gamma}}} \tag{7.9}$$

where u, T, A, J, c_p and γ respectively represent the flow velocity, the flow temperature, the hydraulic cross-section ($A=\pi D^2/4$, where D is the pipe diameter), the impulse, the heat capacity at constant pressure and the ratio between the heat capacity at constant pressure and the one at constant volume [156]. In addition, the Fanning friction factor f can be substituted in the momentum balance equation by means of the following formula:

$$f\equiv\frac{\tau_w}{\rho u^2/2} \tag{7.10}$$

where τ_w stands for the wall shear stress.

After some manipulations, one can obtain eight different equations in which the new differential variables $\mathrm{d}p/p$, $\mathrm{d}\rho/\rho$, $\mathrm{d}u/u$, $\mathrm{d}T/T$, $\mathrm{d}Ma^2/Ma^2$, $\mathrm{d}p_0/p_0$, $\mathrm{d}T_0/T_0$, $\mathrm{d}J/J$ and $\mathrm{d}s$ are defined in terms of $4fdx/D$:

$$
\begin{cases}
\dfrac{dMa^2}{Ma^2} = -\dfrac{(m+1)\,Ma^2}{2(Ma^2-m/\gamma)} \cdot \dfrac{4fdx}{D} \\
\dfrac{dp}{p} = \dfrac{Ma^2 m}{2(Ma^2-m/\gamma)} \cdot \dfrac{4fdx}{D} \\
\dfrac{d\rho}{\rho} = \dfrac{Ma^2}{2(Ma^2-m/\gamma)} \cdot \dfrac{4fdx}{D} \\
\dfrac{du}{u} = -\dfrac{Ma^2}{2(Ma^2-m/\gamma)} \cdot \dfrac{4fdx}{D} \\
\dfrac{dT}{T} = \dfrac{(m-1)\,Ma^2}{2(Ma^2-m/\gamma)} \cdot \dfrac{4fdx}{D} \\
\dfrac{dp_0}{p_0} = \dfrac{mMa^2}{2\,(Ma^2-m/\gamma)} \left[1 - \dfrac{\gamma\frac{(m+1)}{m}Ma^2}{2+(\gamma-1)\,Ma^2}\right] \dfrac{4fdx}{D} \\
\dfrac{dT_0}{T_0} = \dfrac{mMa^2}{2\,(Ma^2-m/\gamma)} \left[(1-\dfrac{1}{m}) - \dfrac{(\gamma-1)\frac{(m+1)}{m}Ma^2}{2+(\gamma-1)\,Ma^2}\right] \dfrac{4fdx}{D} \\
\dfrac{dJ}{J} = \dfrac{mMa^2}{2\,(Ma^2-m/\gamma)} \left[1 - \dfrac{\gamma\frac{(m+1)}{m}Ma^2}{1+\gamma Ma^2}\right] \dfrac{4fdx}{D} \\
\dfrac{ds}{c_v} = \dfrac{m-\gamma}{2} \cdot \dfrac{Ma^2}{Ma^2-m/\gamma} \cdot \dfrac{4fdx}{D}
\end{cases}
\tag{7.11}
$$

As can be inferred by Eq. (7.11), the presented flow results to be choked when $Ma^2 = m/\gamma$, in fact for this Mach value the denominators become null, furthermore, all the logarithmic differential variables change their signs if that Ma value is crossed, starting from either a supersonic or a subsonic flow. Moreover, the stagnation temperature results to be not constant along the pipe since the heat transfer with the walls can occur in this flow model. Finally, it can be observed that if $m = 1$ the analytical expressions pertaining to an isothermal flow can be obtained, coincident to the ones presented in [155]. This proves the consistency of Eq. (7.11).

It is a common choice, in practical calculations on compressible flows, to select the Mach number as the parameter of a parametric solution. Therefore, the formula linking dMa^2 and $4fdx/D$ in Eq. (7.11) can be used to substitute the terms $4fdx/D$ in the other expressions. Furthermore, the obtained relations can be integrated from a general initial state to the choking condition (where

$Ma = \sqrt{m/\gamma}$), and one has:

$$\begin{cases} 4f\dfrac{L_{ch}}{D} = \dfrac{2}{m+1}[\ln\left(\dfrac{\gamma}{m}Ma^2\right) + \dfrac{m-\gamma Ma^2}{\gamma Ma^2}] \\ \dfrac{p}{p_*} = (\dfrac{\gamma}{m}Ma^2)^{-\frac{m}{m+1}} \\ \dfrac{\rho}{\rho_*} = (\dfrac{\gamma}{m}Ma^2)^{-\frac{1}{m+1}} \\ \dfrac{u}{u_*} = (\dfrac{\gamma}{m}Ma^2)^{\frac{1}{m+1}} \\ \dfrac{T}{T_*} = (\dfrac{\gamma}{m}Ma^2)^{-\frac{m-1}{m+1}} \\ \dfrac{p_0}{p_{0*}} = (\dfrac{\gamma}{m}Ma^2)^{-\frac{m}{m+1}} \cdot (\dfrac{1+\frac{\gamma-1}{2}Ma^2}{1+\frac{\gamma-1}{2}\cdot\frac{m}{\gamma}})^{\frac{\gamma}{\gamma-1}} \\ \dfrac{T_0}{T_{0*}} = \left(\dfrac{\gamma}{m}Ma^2\right)^{-\frac{m-1}{m+1}} \cdot (\dfrac{1+\frac{\gamma-1}{2}Ma^2}{1+\frac{\gamma-1}{2}\cdot\frac{m}{\gamma}}) \\ \dfrac{J}{J_*} = (\dfrac{\gamma}{m}Ma^2)^{-\frac{m}{m+1}} \cdot \dfrac{1+\gamma Ma^2}{1+m} \\ s_* - s = c_v\dfrac{m-\gamma}{m+1}\cdot\ln\left(\dfrac{\gamma}{m}Ma^2\right) \end{cases} \tag{7.12}$$

where L_{ch} is the choking length of the duct and the subscript "$*$" refers to the choked flow variables. If the relation between dMa^2 and $4fdx/D$ in Eq. (7.11) is integrated from the initial state with $Ma = Ma_1$ at the pipe inlet ($x = 0$) to a generic position x along the pipe whit a certain Mach number Ma, a non-linear algebraic function which express x in terms of Ma^2 is obtained:

$$\begin{aligned} 4f\frac{x}{D} &= \frac{2}{m+1}\left[\ln\left(\frac{\gamma}{m}Ma_1^2\right) + \frac{m-\gamma Ma_1^2}{\gamma Ma_1^2}\right] + \\ &- \frac{2}{m+1}\left[\ln\left(\frac{\gamma}{m}Ma^2\right) + \frac{m-\gamma Ma^2}{\gamma Ma^2}\right] \end{aligned} \tag{7.13}$$

where the subscript "1" indicates the quantities at the pipe inlet. If the Eq. (7.13) is combined with the algebraic expression of p and u defined in terms of Ma^2 in Eq. (7.12), the following explicit relations can be obtained:

$$\begin{cases} 4f\dfrac{x}{D} &= \dfrac{2}{m}\left[\ln\left(\dfrac{p}{p_*}\right)-\dfrac{m}{m+1}\left(\dfrac{p}{p_*}\right)^{\frac{m+1}{m}}\right]+ \\ &- \dfrac{2}{m}\left[\ln\left(\dfrac{p_1}{p_*}\right)-\dfrac{m}{m+1}\left(\dfrac{p_1}{p_*}\right)^{\frac{m+1}{m}}\right] \\ 4f\dfrac{x}{D} &= 2\left[\ln\left(\dfrac{u_1}{u_*}\right)+\dfrac{1}{m+1}\left(\dfrac{u_1}{u_*}\right)^{-(m+1)}\right]+ \\ &- 2\left[\ln\left(\dfrac{u}{u_*}\right)+\dfrac{1}{m+1}\left(\dfrac{u}{u_*}\right)^{-(m+1)}\right] \end{cases} \tag{7.14}$$

These relations result to be manageable to evaluate p and u along the pipe. With the same procedure, similar expressions can be obtained for other flow properties.

7.1.1 Comparison between the polytropic flow and the Fanno or Rayleigh flow

A Fanno subsonic flow is taken into account, the length of a pipe, namely L_{Fanno}, and the duct diameter D are selected ($\gamma = 1.4$). In all the considered cases, a constant friction factor $f = 0.003$ has been selected, if fact it results to be a good approximation of the mean value for both the subsonic and supersonic flow regimes. The stagnation pressure $p_{0,1}$ and temperature T_0 are fixed at the pipe inlet, while the pressure p_2 is selected as the downstream environment pipe. With this set of data, the Mach numbers at the pipe inlet and outlet, i.e. Ma_1 and Ma_2, and the inlet pressure p_1 can be evaluated with the Fanno model.

The constant polytropic exponent m can be evaluated, for a polytropic flow, based on the flow properties of the Fanno model, by applying:

$$m = \frac{\ln\left(p_{in}/p_{out}\right)}{\ln\left(\rho_{in}/\rho_{out}\right)} \tag{7.15}$$

Experimental pressures and temperatures measured at the pipe inlet and outlet can also be used in Eq. (7.15) when a real case is considered. Eqs. (7.12) and (7.13), coupled with the polytropic law, have been used in the flow property distributions evaluation along the duct. In Figs. 7.1-7.4, four different cases

for both subsonic and supersonic flows are shown. A slight difference can be noticed in the duct length between the polytropic and the Fanno model, for this reason the abscissa reported in the figures is the ratio between the space coordinate x and the corresponding duct length (both L_{Fanno} or L_{pol}). For all the cases, the geometry and the boundary conditions are fixed, hence the pipe length L_{pol} can be evaluated based on m value by means of the first expression in Eq. (7.12):

$$\frac{4fL_{pol}}{D} = \left(\frac{4fL}{D}\right)_{Ma_1} - \left(\frac{4fL}{D}\right)_{Ma_2} \tag{7.16}$$

where the right-side terms are a function of Ma_1 and Ma_2, respectively.

The Ma, p, T, T_0 and u distributions reported in Fig. 7.1 refer to $p_{0,1} = 1$ bar, $T_0 = 400$ K, $p_2 = 0.6$ bar, $L_{Fanno} = 80$ cm and $D = 1.96$ cm. By means of Eq. (7.15), one has $m \approx 1.18$ ($m < \gamma$ for a subsonic flow) and consequently the pipe length for the polytropic flow is $L_{pol} \approx 80.28$ cm, which is almost coincident to L_{Fanno}. As can be inferred, the difference between L_{Fanno} and L_{pol} only depends on the selected m, therefore, it can be assumed as an index of the polytropic model accuracy to approximate the Fanno flow. The Mach number distribution, represented by a continuous line for the polytropic model and with rhombus symbols for the Fanno one never reaches the choking value $\sqrt{m/\gamma} \approx 0.915$, therefore the outlet pressure can be fixed at p_2 in all the cases.

In general, the flow properties distributions along the duct are analogous for both the considered models. Mass flow-rates $G = \rho_1 u_1 A$ are the same, in fact the flow conditions at the pipe inlet are coincident in the two cases.

If the MSPE (mean squared percentage error) is introduced, evaluated for the different properties of the polytropic flow with respect to the one of Fanno's flow, it has been found that the maximum value occurs for the density, and it is equal to 0.36%. From Fig. 7.1, it can be seen that the total temperature is not constant along the pipe, for the polytropic model. Even if the overall heat exchanged is null ($T_{0,2} = T_{0,1}$), the evolution, contrarily to the Fanno flow one, is not strictly adiabatic. Therefore, the polytropic flow expels some heat and then it absorbs the same amount of heat.

The results reported in Fig. 7.2 refer to a subsonic choked flow, with $p_{0,1} = 1$ bar, $T_0 = 400$ k, $p_2 = 0.3$ bar $< p^* \approx 0.48$ bar, where p^* represents Fanno's flow choked value of the pressure, $L_{Fanno} = 40$ cm and $D = 1.96$ cm. In this case, it

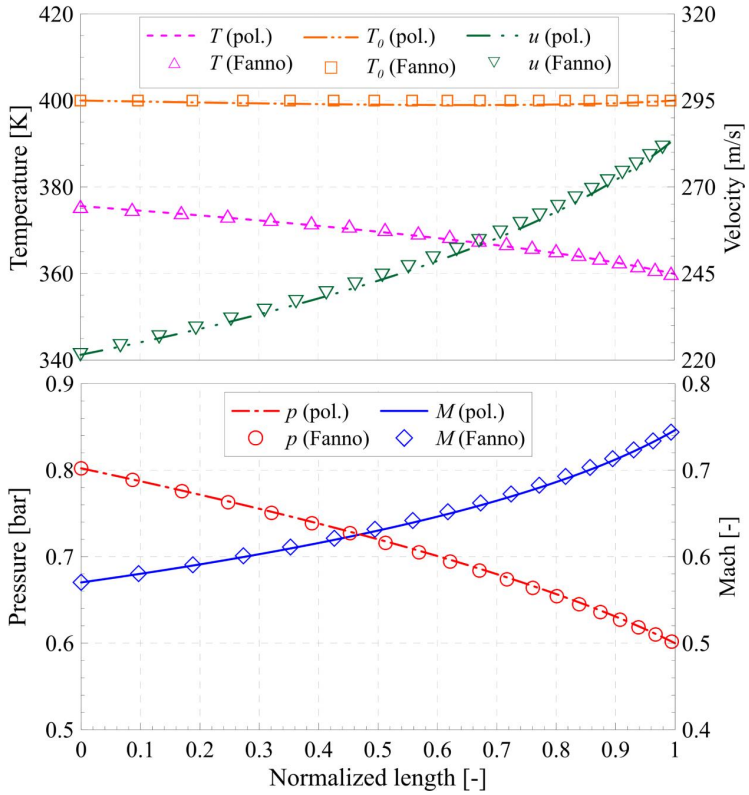

Figure 7.1: Comparison between the polytropic and the Fanno flows ($p_{0,1} = 1$ bar, $T_0 = 400$ K, $p_2 = 0.6$ bar, $L_{Fanno} = 80$ cm, $D = 1.96$ cm).

results that $m \approx 1.28$ and $L_{pol} \approx 41.34$ cm, therefore the difference with respect to L_{Fanno} is slightly increased, while m is closer to γ.

An evident discrepancy between the two flows is that the Mach number in the polytropic model cannot reach 1, since in this case the choking conditions occurs for $Ma = \sqrt{m/\gamma} \approx 0.956$. As a consequence, none of the presented variables of the polytropic flow are able to match the Fanno flow ones at the pipe outlet. The maximum MSPE occurs in the pressure, and it is equal to 2.1%.

Similarly to Fig. 7.1, the polytropic flow is not adiabatic, rejecting heat at the beginning and then some heat is absorbed. However, since the value $p_2 < p^*$ cannot be reached at the pipe exit (the polytropic pressure is $p_* \approx 0.50$ bar $> p^* \approx 0.48$ bar, the absorbed heat quantity does not compensate the previously rejected one. Therefore, a small difference exists between the stagnation temperatures at the duct exit (around 1.4 K, which corresponds to

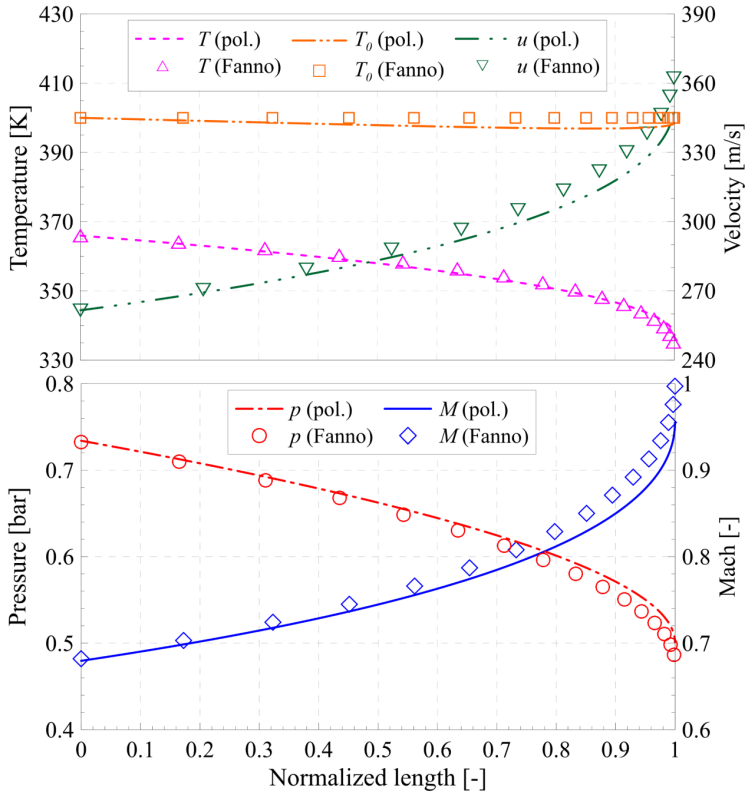

Figure 7.2: Comparison between the polytropic and the Fanno flows ($p_{0,1} = 1$ bar, $T_0 = 400$ K, $p_2 = 0.3$ bar, $L_{Fanno} = 40$ cm, $D = 1.96$ cm).

around 0.35%). In general, discrepancies between the Fanno and the polytropic models are larger in Fig. 7.2 than in Fig. 7.1.

From a wide range of tests, with different couples of Ma_1 and Ma_2 (with $Ma_2 < \sqrt{m/\gamma}$) it has been observed that the MSPE pertaining to all the flow properties is always lower than 3%.

In Figs. 7.3 and 7.4 the same distributions of Figs. 7.1 and 7.2 are reported, for two supersonic flow cases with $p_{0,1} = 5.57$ bar, $T_0 = 900$ K, $u_1 = 1000$ m/s, $L_{Fanno} = 35$ cm and $D = 1.96$ cm and with $p_{0,1} = 5.57$ bar, $T_0 = 1000$ K, $u_1 = 1000$ m/s, $L_{Fanno} = 60.15$ cm and $D = 1.96$ cm, respectively. The latter, refers to a choked supersonic flow. It can be obtained that $L_{pol} \approx 34.7$ cm and $m \approx 2.72$ in Fig. 7.3 and that $L_{pol} \approx 62.3$ cm and $m \approx 1.93$ for the case reported in Fig. 7.4 (it can be inferred that $m > \gamma$ for a supersonic flow). Pertaining to the properties distributions of the unchoked polytropic flow in Fig. 7.3, they start and end at the same values as those of the Fanno model by following

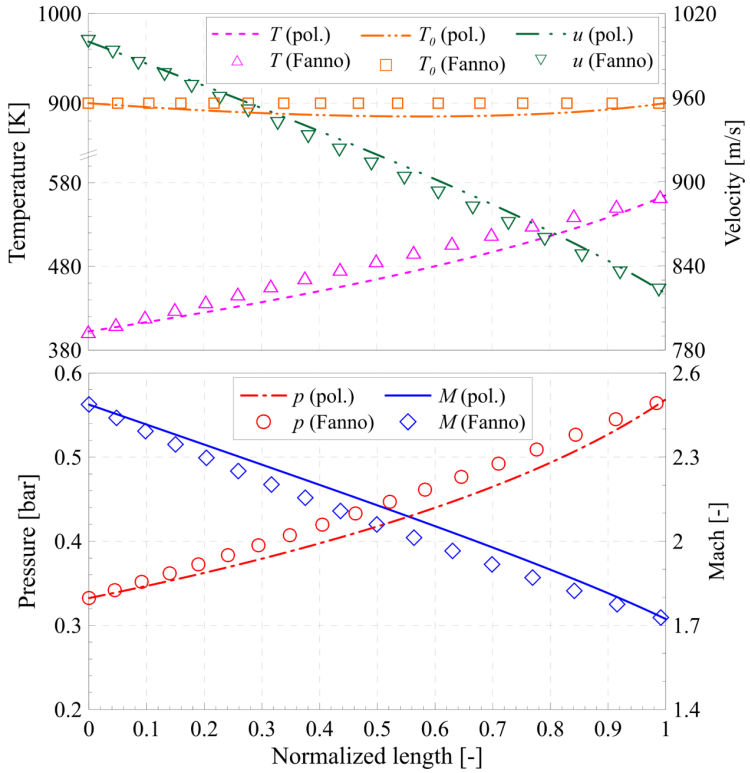

Figure 7.3: Comparison between the polytropic and the Fanno flows ($p_{0,1} = 5.57$ bar, $T_0 = 900$ K, $u_1 = 1000$ bar, $L_{Fanno} = 35$ cm, $D = 1.96$ cm).

analogous trends. However, in this case a more evident discrepancy can be noticed from the comparison of the different traces than the ones pertaining to the subsonic flow in Fig. 7.1. The maximum MSPE experienced in Fig. 7.3 occurs for the pressure, and it is 3.3%.

From a wide range of tests pertaining to a supersonic flow, with different couples of Ma_1 and Ma_2 (with $Ma_2 > \sqrt{m/\gamma}$) it has been observed that, generally, the greater is Ma_1 and the difference with Ma_2, the bigger is the MSPE for all the flow properties. As an example, for the case with Ma_1=2 and $Ma_2 = 1.2$, the maximum MSPE refers to the pressure and it is close to 7%.

Concerning to the choked Fanno flow in Fig. 7.4, the corresponding polytropic flow features $Ma_2 = \sqrt{m/\gamma} \approx 1.17$. Similarly to the choked subsonic flow in Fig. 7.2, all the polytropic flow properties are not able to match the Fanno ones at the pipe outlet. Furthermore, a greater discrepancy can be noticed for

the polytropic in Fig. 7.4 than in Fig. 7.2. The considered choked supersonic flow features a maximum MSPE of 15.7%, referred to the pressure distribution.

Based on the presented results, it can be deduced that the best accuracy of the polytropic model is obtained for a subsonic flow with the outlet Mach number of the corresponding Fanno flow lower than $\sqrt{m/\gamma}$ (cf. Fig. 7.1).

In addition, the polytropic model accuracy is higher for a subsonic flow than for a supersonic one. However, a supersonic flow with the outlet Mach number of the corresponding Fanno flow higher than $\sqrt{m/\gamma}$ can be still satisfactorily modelled (cf. Fig. 7.3). When one has for, a subsonic flow, $\sqrt{m/\gamma} < Ma_2 \leq 1$ or, for a supersonic flow, $1 \leq Ma_2 < \sqrt{m/\gamma}$, the difference between L_{Fanno} and L_{pol} tends to increases. Hence, the polytropic model assumption results to be inconsistent in the compressible adiabatic viscous flows simulation along a constant cross-section pipes (the downstream pressure p_2 cannot be reached).

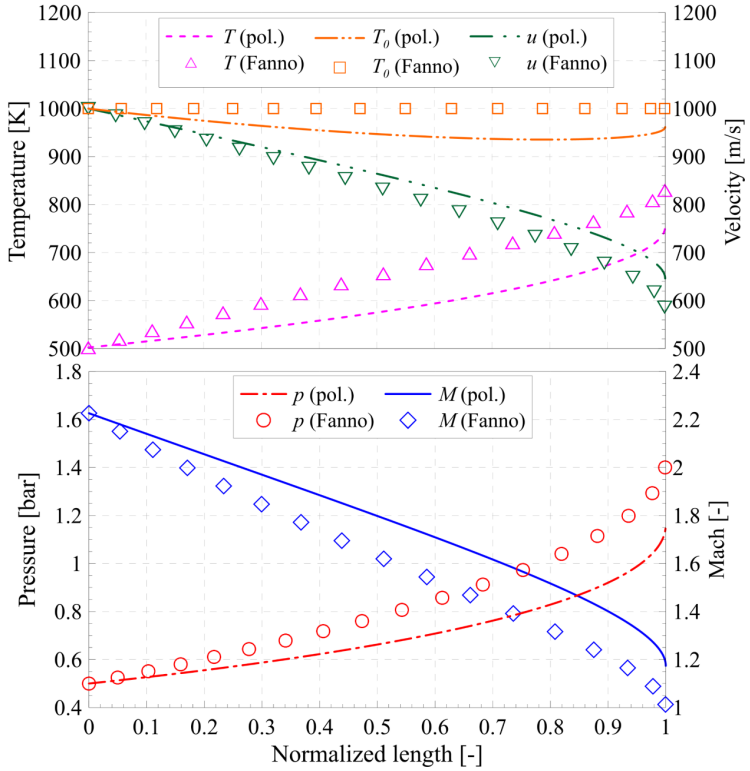

Figure 7.4: Comparison between the polytropic and the Fanno flows ($p_{0,1} = 5.57$ bar, $T_0 = 1000$ K, $u_1 = 1000$ m/s, $L_{Fanno} = 60.15$ cm, $D = 1.96$ cm).

For both the cases with $Ma_2 < \sqrt{m/\gamma}$ or $Ma_2 > \sqrt{m/\gamma}$, by means of the polytropic model a correct evaluation of the global viscous power dissipation per unit of mass flow-rate is achieved, where the latter is evaluated with the formula $l_w = c(T_2 - T_1)$ where $c = c_v(m-\gamma)/(m-1)$ stands for the constant specific heat of the polytropic process.

As far as the Rayleigh flow modelling is concerned, the polytropic flow with a constant m is not capable to fit the flow properties distributions. As can be inferred for a flow with heat transfer where the friction is neglected, the velocity can be written as $u = \sqrt{dp/d\rho}$ [155], therefore, for a polytropic process, a constant Mach number equal to $\sqrt{m/\gamma}$ would be maintained along the pipe, that is in contrast with the results of the Rayleigh flow. For this reason, a polytropic flow cannot be used to model compressible inviscid diabatic flow characterized by a significant transfer of kinetic energy.

Finally, a set of analytical equations equivalent to the one reported in Eq. (7.12) could be obtained by maintaining the energy equation and by substituting the momentum balance equation with the equation of the polytropic evolution. As a consequence, the energy equation would feature the heat transfer between the flow and the pipe walls and it should be appropriately modelled, in accordance to the entropy equation, by means of the constant specific heat for the polytropic heat expression. In fact, as has been previously shown, a viscous adiabatic flow modelled with a constant polytropic exponent presents a local heat exchange (cf. the non-constant stagnation temperature distributions in Figs. 7.1-7.4). The selected m value is able to guarantee only a null global heat (not the local one) with the correct computation of the global viscous power dissipation.

7.2 Numerical model with variable m and its application

In order to better understand limits in modelling a viscous flow in choking conditions by means of a polytropic flow, a numerical barotropic model where the polytropic exponent is a function of x has been developed. The governing equations are the generalized Euler partial differential equations, namely the mass conservation and the momentum balance. Concerning to the energy

equation, this has been substituted by the polytropic speed of sound relation, $dp = \frac{m}{\gamma} a_s^2 d\rho$, expressed in terms of Lagrangian derivatives. One obtains:

$$\begin{cases} \dfrac{\partial \rho}{\partial t} + \dfrac{\partial (\rho u)}{\partial x} = 0 \\ \dfrac{\partial p}{\partial t} - \dfrac{a_s^2 m}{\gamma} \dfrac{\partial \rho}{\partial t} + u \left[\dfrac{\partial p}{\partial x} - \dfrac{a_s^2 m}{\gamma} \dfrac{\partial \rho}{\partial x} \right] = 0 \\ \dfrac{\partial (\rho u)}{\partial t} + \dfrac{\partial \left(\rho u^2 + p \right)}{\partial x} = -\dfrac{4\tau_w}{D} \end{cases} \tag{7.17}$$

where $a_s = \sqrt{\gamma RT}$ stands for the isentropic speed of sound (R is the elasticity constant of a perfect gas). The function $m(x)$ has been obtained by applying Eq. (7.15) based on the fluid properties corresponding to two consecutive points along the axis of the Fanno flow solution. The $m(x)$ function can also be graphically obtained by evaluating the local slope of the Fanno curve represented in the enthalpy-entropy diagram.

As can be inferred from Figs. 7.1-7.4, solutions are smooth, hence Eq. (7.17) can be written in non-conservative diagonal form, as follow [157]:

$$\frac{\partial \boldsymbol{w}}{\partial t} + [\mathbf{C}] \frac{\partial \boldsymbol{w}}{\partial x} = \boldsymbol{H} \tag{7.18}$$

where $[\mathbf{C}]$ is the diagonalized Jacobian matrix, written as a function of m, γ, u and a_s:

$$[\mathbf{C}] = \begin{bmatrix} u - \sqrt{\dfrac{m}{\gamma}} a_s & 0 & 0 \\ 0 & u & 0 \\ 0 & 0 & u + \sqrt{\dfrac{m}{\gamma}} a_s \end{bmatrix} \tag{7.19}$$

and $\boldsymbol{w}$ represents the vector of the Riemann variables, defined as

$$\delta \boldsymbol{w} = \begin{bmatrix} \delta w_1 \\ \delta w_2 \\ \delta w_3 \end{bmatrix} = \begin{bmatrix} -\dfrac{\rho}{2\sqrt{(m/\gamma)} a_s} \delta u + \dfrac{1}{(2m/\gamma) a_s^2} \delta p \\ \delta \rho - \dfrac{1}{(m/\gamma) a_s^2} \delta p \\ \dfrac{\rho}{2\sqrt{(m/\gamma)} a_s} \delta u + \dfrac{1}{(2m/\gamma) a_s^2} \delta p \end{bmatrix} \tag{7.20}$$

Finally, $\boldsymbol{H}$ stands for the vector of the source terms

$$\boldsymbol{H} = \begin{bmatrix} H_1 \\ H_2 \\ H_3 \end{bmatrix} = \begin{bmatrix} \dfrac{1}{2\sqrt{(m/\gamma)}a_s} \cdot \dfrac{4\tau_w}{D} \\ 0 \\ -\dfrac{1}{2\sqrt{(m/\gamma)}a_s} \cdot \dfrac{4\tau_w}{D} \end{bmatrix} \tag{7.21}$$

As can be noticed, the acoustic eigenvalues of the Jacobi matrix, namely $u \pm \sqrt{(m/\gamma)}a_s = u \pm \sqrt{mRT}$, result to be different than the values $u \pm a_s$, typical of the one-dimensional Euler equations [157]. Therefore, in the polytropic model acoustic waves propagate with different speeds with respect to the Fanno flow, but this does not produce any inaccuracy in the steady-state (time asymptotic) solution.

In order to discretize Eq. (7.18) a finite-difference second-order accuracy upwind numerical scheme has been adopted, by following the Riemann decoupling approach. A time step Δx has been selected and, based on the Courant number (fixed at 0.9 for all the simulations), Δt has been obtained by applying the CFL condition. All the Δx values have been chosen in order to guarantee grid independent numerical solutions. Since the investigation is focused on time asymptotic properties, the simulation stops when the flow properties variation become negligible between two time steps. Boundary conditions are assigned in accordance to the hyperbolic partial differential equations theory [157].

7.3 Numerical results

The numerical simulations with a variable m have been performed by considering the choking cases, for both a subsonic and a supersonic Fanno flow, reported in Figs. 7.2 and 7.4. The comparison between the analytical results from Fanno's model and the steady-state solutions provided by the numerical model are reported in Figs. 7.5 and 7.6.

Fig. 7.5 represents the subsonic flow tested in Fig. 7.2. The numerical model has $\Delta x = 2$ mm, hence the computational grid is formed by 201 nodes (L_{Fanno}= 40 cm), providing a grid independent solution. The length L_{pol} results to be coincident with L_{Fanno}, as well as all the flow properties distributions. As can be inferred, the polytropic exponent $m(x)$ increases along x, reaching

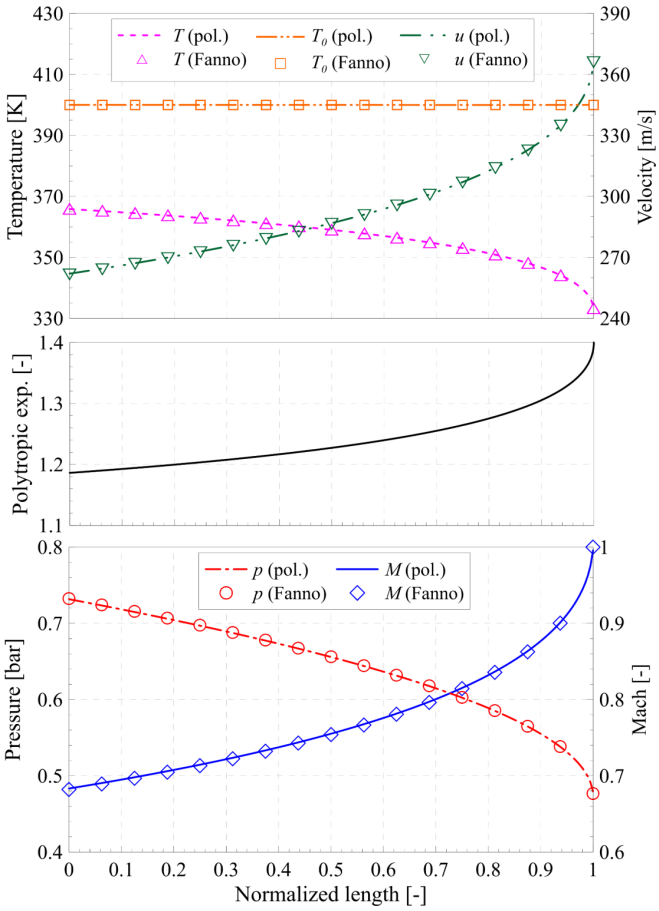

Figure 7.5: Comparison between the numerical model solution and the Fanno flow ($p_{0,1} = 1$ bar, $T_0 = 400$ K, $p_2 = 0.3$ bar, $L_{Fanno} = 40$ cm, $D = 1.96$ cm).

the value $\gamma = 1.4$ at the duct outlet. Therefore, the numerical model solution is able to accurately follow Fanno's distributions along the entire pipe till the choking condition, where $\sqrt{m(x_2)/\gamma} = 1$.

In Fig. 7.6 the comparison between the Fanno flow and the numerical model outcomes are reported pertaining to the same supersonic choked flow presented in Fig. 7.4. In this case 401 nodes have been considered ($\Delta x = 1.5$ mm for $L_{Fanno} = 60.15$ cm). Also in this case the numerical properties distributions match perfectly the Fanno flow ones. The m distribution decreases till the choking value $m(x_2) = \gamma$ reached at the pipe exit, corresponding to Mach number equals to 1.

From the results of this Section it is evident that only a polytropic model with a variable m is able to correctly simulate a compressible viscous flow in

choking condition. Furthermore, from Eq. (7.11) can be noticed that when $Ma \to \sqrt{m/\gamma}$ all the flow properties start to change rapidly with respect to x, due to the denominators which start to approach zero, hence, the process starts to be adiabatic. This is the reason why the polytropic model with $m \neq \gamma$ is not consistent for a choked flow.

As can be seen from Figs. 7.5 and 7.6, the numerical model with a variable m is able to accurately converge to the Fanno analytical steady-state solution, although the polytropic eigenvalues $u \pm \sqrt{m/\gamma} a_s$ are different from $u \pm a_s$. Nevertheless, this difference on the eigenvalues leads to a discrepancy on the solutions over the time transient, i.e., the time histories of p, u, T and Ma along the pipe do not reproduce the real ones. Hence, only the time asymptotic solution can be compared with the analytical ones.

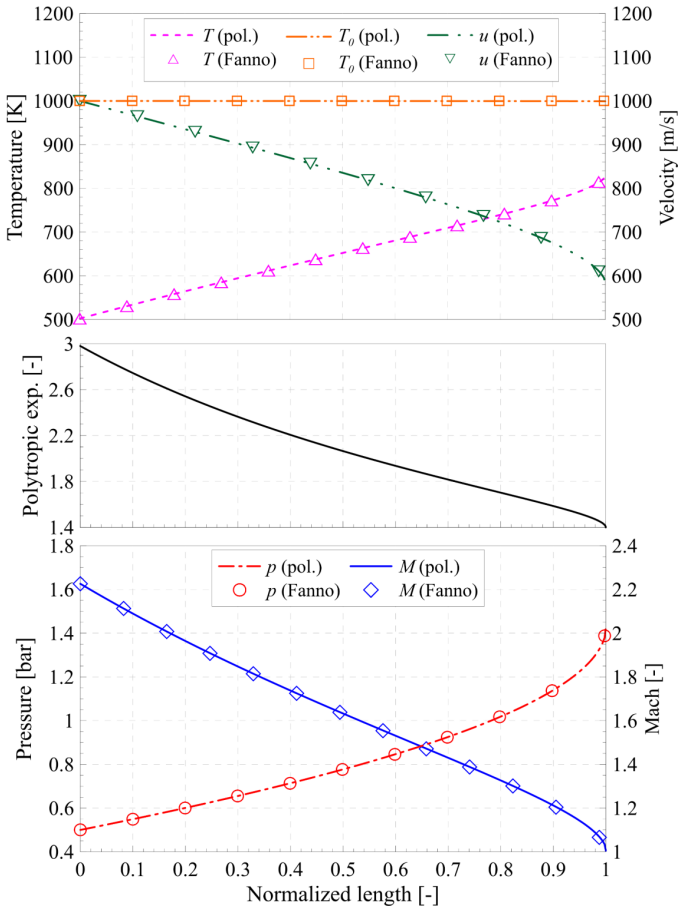

Figure 7.6: Comparison between the numerical model solution and the Fanno flow ($p_{0,1} = 5.57$ bar, $T_0 = 1000$ K, $u_1 = 1000$ m/s, $L_{Fanno} = 60.15$ cm, $D = 1.96$ cm).

A similar analysis has been performed for the Rayleigh flow: also in this case all the polytropic steady-state properties distributions perfectly converge to the analytical ones of the inviscid diabatic flow.

7.4 Results for a viscous diabatic flow

The numerical model presented in Sect. 7.2 has been modified in order to solve the entire set of Euler's partial differential equations, that are the mass conservation equation, the momentum balance equation and the total energy conservation for a flow with both wall friction and heat transfer:

$$\frac{\partial}{\partial t}\begin{bmatrix}\rho\\ \rho u\\ E\end{bmatrix}+\frac{\partial}{\partial x}\begin{bmatrix}\rho u\\ \rho u^2+p\\ u(E+p)\end{bmatrix}=\begin{bmatrix}0\\ -\dfrac{4\tau_w}{D}\\ \dfrac{4\dot{q}_f}{D}\end{bmatrix} \tag{7.22}$$

where E represents the total energy per unit of volume (given by the sum of the kinetic energy per unit of volume and the internal energy per unit of volume) and $\dot{q}_f$ stands for the heat flux, i.e., the heat transfer power per unit of wall area. Different conditions have been taken into account and, based on Eq. (7.15), m has been evaluated. The polytropic model with constant m (cf. Eqs. (7.12)-(7.14)) has been applied. The comparison between the polytropic model results and the numerical simulations ones (where the energy equation is considered, cf. Eq. (7.22)) are shown in Figs. 7.7-7.9. In this Section, only subsonic flows not close to be sonic have been considered, in fact the lower accuracy regarding a supersonic flow or a choked flow modelled by means of a polytropic approach has been already discussed in Sect. 7.1.1. Also in these cases, the maximum Courant number has been selected equal to 0.9.

Fig. 7.7 shows the properties distributions for the case with $p_{0,1} = 1$ bar, $T_0 = 400$ K, $p_2 = 0.6$ bar, $L_{Fanno} = 20$ cm ($\Delta x = 0.5$ mm), $D = 1.96$ cm, $f = 0.003$ and $\dot{q}_f = 2 \cdot 10^4$ W/m^2 while Fig. 7.8 refers to $p_{0,1} = 1$ bar, $T_0 = 400$ K, $p_2 = 0.75$ bar, $L_{Fanno} = 30$ cm ($\Delta x = 0.5$ mm), $D = 1.96$ cm, $f = 0.003$ and $\dot{q}_f = 7 \cdot 10^4$ W/m^2. Finally, Fig. 7.9 refers to $p_{0,1} = 1$ bar, $T_0 = 800$ K, $p_2 = 0.59$ bar, $L_{Fanno} = 50$ cm ($\Delta x = 2.5$ mm), $D = 1.96$ cm, $f = 0.004$ and $\dot{q}_f = 2 \cdot 10^4$ W/m^2.

From the results reported in Fig. 7.7 and 7.8, by means of the polytropic approach a very accurate prediction of the generalised Euler equations properties distributions can be achieved. In Fig. 7.7, one has $m = 1.157$ (both the temperature and the pressure decrease along the duct) and the length is $L_{pol} \approx 20.05$ cm, whereas in the case of Fig. 7.8, m is approximately equal to 0.673 (the temperature increases along the pipe, while the pressure reduces) and the polytropic length is $L_{pol} = 30.25$ cm.

Pertaining to Fig. 7.9, the numerical temperature spacial trace obtained by means of Eq. (7.22) exhibits a local maximum along the pipe (the temperature firstly increases, then reduces). Under such conditions, the constant m polytropic model may not provide very consistent results in terms of the properties distributions for the viscous diabatic flow. For the analysed case, one has $m \approx 0.866$ and $L_{pol} \approx 52$ cm. However, with $m < 1$ only a monotonically increasing trend of the temperature along the pipe can be achieved, while a polytropic exponent in the range $1 < m < \gamma$ is required when the temperature

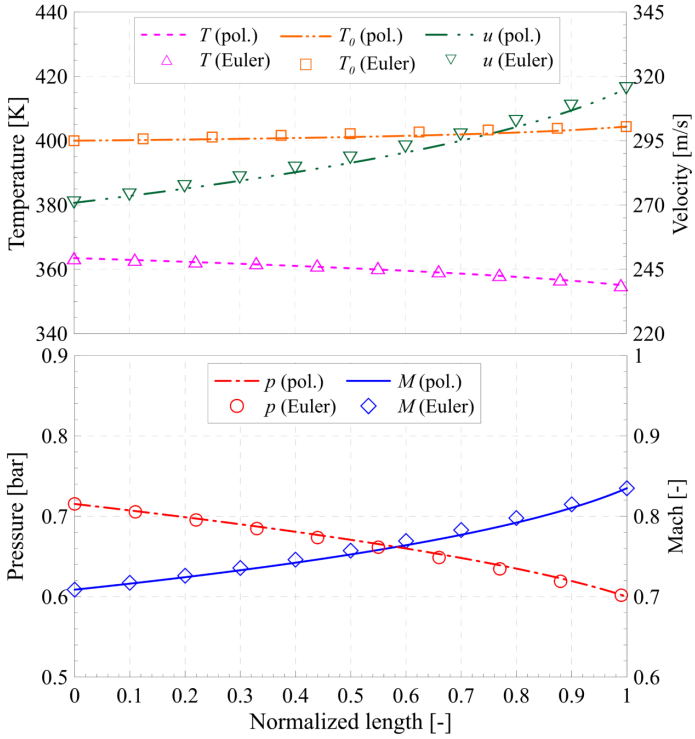

Figure 7.7: Comparison between the polytropic flow and the Euler generalized equations result ($p_{0,1} = 1$ bar, $T_0 = 400$ K, $p_2 = 0.6$ bar, $L = 20$ cm, $f = 0.003$, $\dot{q}_f = 2 \cdot 10^4$ W/m^2, $D = 1.96$ cm)

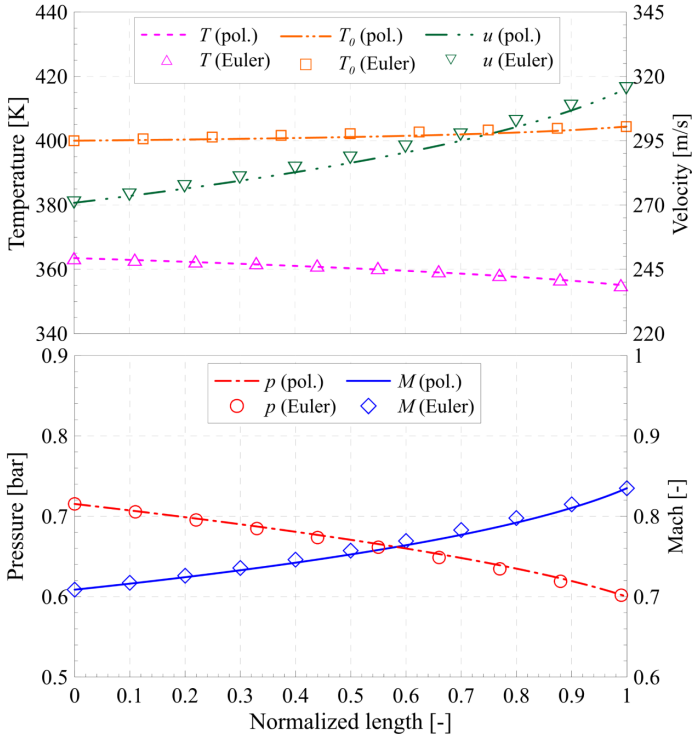

Figure 7.8: Comparison between the polytropic flow and the Euler generalized equations result ($p_{0,1} = 1$ bar, $T_0 = 400$ K, $p_2 = 0.75$ bar, $L = 30$ cm, $f = 0.003$, $\dot{q}_f = 7 \cdot 10^4$ W/m^2, $D = 1.96$ cm)

decreases along the duct. Hence, any local maximum point featured by the temperature cannot be predicted by means of the polytropic model with constant m.

The Mach number corresponding to the maximum temperature value, namely Ma_{Tmax}, can be analytically obtained by summing and put to zero the Fanno and Rayleigh temperature differentials. Even if the steady-state Euler equations are not linear, under the hypothesis of $dT/dx = 0$ (holds when the maximum temperature is reached) they become linear, hence the superposition of effects can be locally applied around the T_{max}:

$$dT_{Fanno} + dT_{Rayleigh} = 0 \tag{7.23}$$

The first term is expressed as [155]:

$$dT_{Fanno} = -\frac{\gamma(\gamma-1)Ma^4}{2(1-Ma^2)} 4f \frac{dx}{D} T_{Fanno} \tag{7.24}$$

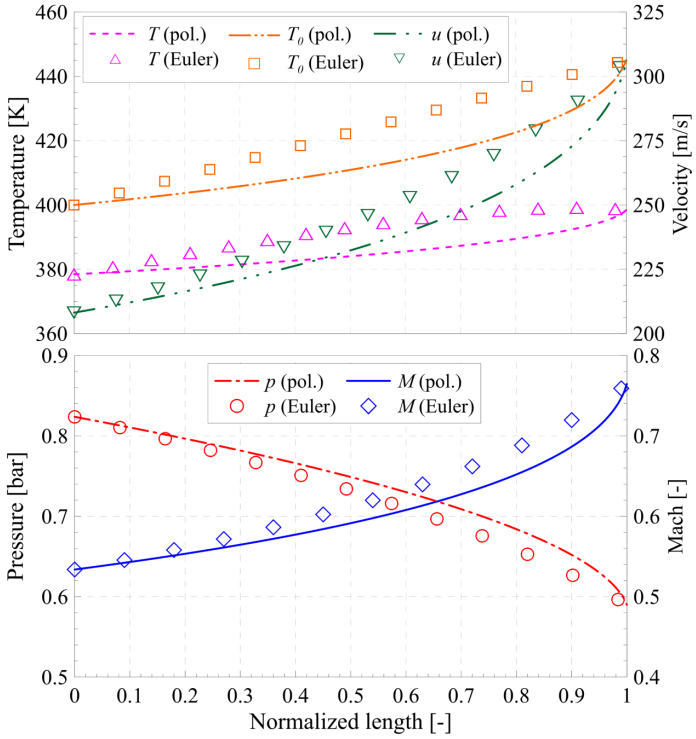

Figure 7.9: Comparison between the polytropic flow and the Euler generalized equations result ($p_{0,1} = 1$ bar, $T_0 = 400$ K, $p_2 = 0.595$ bar, $L = 50$ cm, $f = 0.004$, $\dot{q}_f = 7 \cdot 10^4$ W/m^2, $D = 1.96$ cm)

By taking into account the definition of Fanno's friction power per unit of mass flow-rate for length dx, namely δl_w, one has:

$$\delta l_w = \frac{1}{2}\gamma R M a^2 4 f \frac{dx}{D} T_{Fanno} \tag{7.25}$$

hence, Eq. (7.24) can be rewritten as:

$$dT_{Fanno} = -\frac{\gamma M a^2}{(1 - M a^2)} \frac{\delta l_w}{c_p} \tag{7.26}$$

The term pertaining to the Rayleigh flow in Eq. (7.23) can be written as [158, 159]:

$$dT_{Rayleigh} = \frac{1 - \gamma M a^2}{1 - M a^2} dT_0 \tag{7.27}$$

According to the steady-state energy equation, the variation of the total temperature, dT_0, can be written as $\delta q / c_p$, where δq stands for the heat transfer

power per unit of mass flow-rate for the length dx. Hence, Eq. (7.27) can be written as:

$$dT_{Rayleigh} = \frac{1-\gamma Ma^2}{1-Ma^2}\frac{\delta q}{c_p} \tag{7.28}$$

By substituting Eqs. (7.26) and (7.28) in Eq. (7.23), one has

$$\delta l_w = \frac{1-\gamma Ma_{Tmax}^2}{\gamma Ma_{Tmax}^2}\delta q \tag{7.29}$$

Eq. (7.29) results to be consistent with both the Rayleigh flow (if $\delta l_w = 0$, one has $Ma_{Tmax} = 1/\sqrt{\gamma}$, which is Mach number value at which the maximum temperature occurs for a Rayleigh flow) ant the Fanno flow (if $\delta q \to 0$, one has $Ma_{Tmax} \to 0$, and in fact the Fanno temperature distribution continuously decreases while Ma rises).

Values of δl_w and δq in Eq. (7.29) should be calculated close to the point of the pipe where $Ma = Ma_{Tmax}$. Hence, in order to obtain an effective and accurate formula for Ma_{Tmax}, the Fanno temperature is substituted in Eq. (7.25) by means of the following expression:

$$T_{Fanno} = \frac{T^*(\gamma+1)}{2\left(1+\frac{\gamma-1}{2}Ma^2\right)} \tag{7.30}$$

where T^* represents the critical Fanno temperature corresponding to $Ma = 1$. The term δq in Eq. (7.29) is substituted by means of $\dot{q}_f$ according to the formula

$$\delta q = \frac{\dot{q}_f \pi D dx}{G} \tag{7.31}$$

Finally, Eq. (7.29) becomes:

$$\gamma\left[\frac{1}{2}\gamma R Ma_{Tmax}^2\frac{4f}{D}\frac{T^*(\gamma+1)}{2\left(1+\frac{\gamma-1}{2}Ma_{Tmax}^2\right)}+\frac{\dot{q}_f\pi D}{G}\right]Ma_{Tmax}^2 = \frac{\dot{q}_f\pi D}{G} \tag{7.32}$$

and it can be solved in terms of Ma_{Tmax}, and one obtains:

$$Ma_{Tmax} = \sqrt{\frac{\left(\frac{\gamma-1}{2\gamma}-1\right)+\sqrt{\left(1-\frac{\gamma-1}{2\gamma}\right)^2+\frac{2}{\gamma}\left[(\gamma+1)\frac{2fa^{*2}L}{q_{1,2}D}+(\gamma-1)\right]}}{\left[(\gamma+1)\frac{2fa^{*2}L}{q_{1,2}D}+(\gamma-1)\right]}} \tag{7.33}$$

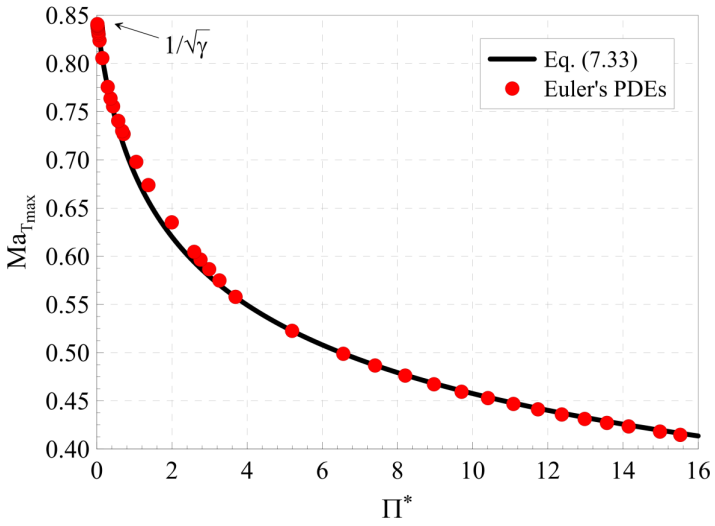

Figure 7.10: Comparison of Ma_{Tmax} for different tests with the trend of Eq. (7.33)

where a^* represents the isentropic speed of sound evaluated at T^* and $q_{1,2} = q(x_2)$ is the total heat power per unit of mass flow-rate.

In Fig. 7.10 Ma_{Tmax} is plotted as a function of the dimensionless parameter $\Pi^* = \frac{2f{a^*}^2 L}{q_{1,2} D}$, which can represent the ratio of a viscous power dissipation to a heat power; the shear wall friction is evaluated by means of the Darcy-Weisbach formula considering a flow velocity equals to the speed of sound a^*. The results reported with a continuous line refer to Eq. (7.33) under the hypothesis of $\dot{q}_f$ =const, while the symbols represent the Ma_{Tmax} obtained from the Euler partial differential equations numerical model (cf. Eq. (7.22)). From the results in Fig. 7.10, Eq. (7.33) can be considered validated. Eq. (7.33) is a new exact formula able to provide the Ma_{Tmax} of a viscous diabatic subsonic flow for a certain set of boundary conditions.

In conclusion, the polytropic model with a constant m is able to provide an excellent prediction of the flow properties distribution when either the Mach number at the duct exit is lower than Ma_{Tmax} or when the Mach number at the pipe inlet is higher than Ma_{Tmax} and the flow is unchoked. Nevertheless, if Ma_{Tmax} is between Ma_1 and Ma_2, the polytropic model can faithfully predict the properties distributions, in fact the error introduced in Fig. 7.10 is not so relevant.

Chapter 8

Conclusions

In this work a numerical-experimental analysis of diesel injection systems and one-dimensional high-pressure pipelines has been performed. The effect of the fuel temperature on the hydraulic performance of a CR system has been studied. Moreover, innovative control strategies based on physical and on TFA approach have been developed. The accuracy of a new flowmeter for high-pressure fluids has been assessed. The CF injection system has been characterized from the hydraulic point of view and the effect of the accumulation volume size has been explored, both numerically and experimentally. The unsteady friction effect on 1D high-pressure transient flows numerical simulations has been analysed. Finally, the scopes of the polytropic flow in modelling gaseous flows involving friction and heat transfer have been investigated.

In Chap. 2, the fuel temperature influence on the CR hydraulic performance has been investigated. An experimental campaign has been performed on single injections, for different nominal rail pressure and ET values, by selecting two different values of fuel temperature in the tank, namely 40 ℃ and 68 ℃. A thermodynamic model has been developed to estimate the fuel temperature at the nozzle exit. The fuel temperature at the injector inlet has been evaluated by assuming an isentropic compression in the pump, then, by means of an isenthalpic process within the injector, the fuel temperature at the nozzle exit has been calculated. This value, for each nominal pressure level, has been compared with the one measured by means of a temperature probe mounted 25 mm below the injector tip. When the measured temperature becomes independent of ET, it is well correlated with the isenthalpic one, which overestimates the real temperature value.

By means of a 1D diagnostic model, the internal injector dynamic has been analysed for different temperature levels. The selected boundary conditions were the electrical current to the pilot stage solenoid and the pressure at the injector inlet. In addition, also the temperature at the injector inlet, evaluated by means of the isentropic compression, has been provided to the model. From the numerical results it can be seen that in the considered fuel temperature range the main effect is on the needle lift trace. When the fuel temperature augments, there is a reduction in the friction force acting on the needle (that is proportional to the viscosity), hence the needle lift peak value increases, leading to an augmented injection temporal length (ITL) and injected quantity for fixed ET and p_{nom}.

In Chap. 3 an innovative flowmeter layout and algorithm to measure the instantaneous high-pressure flow-rate have been presented. The layout consists in two pressure transducers mounted on the examined pipeline at a certain distance. The algorithm is based on the mass conservation equation and the momentum balance equation, written for an incompressible flow. By means of these equations, a relation between the difference of the two pressure time histories and the instantaneous flow-rate (averaged with respect to the spatial coordinate) can be determined. A 3D model of a gear pump and its delivery pipe, validated from the pressure point of view by using an experimental pressure trace along the high-pressure delivery line, has been used to assess the new flowmeter accuracy. For different working conditions, the numerical flow ripples have been compared with the experimental ones and they resulted almost coincident, hence the flowmeter accuracy has been further demonstrated.

In Chap. 4, two different control strategies for the injected mass have been presented. As has been seen in Chap. 2, the injected mass is affected by the fuel temperature, i.e. for a fixed couple of p_{nom} and ET, the injected quantity increases with the fuel temperature. The first presented control strategy is based on a physical approach. The instantaneous mass flow-rate entering the injector has been measured by means of one or two pressure traces obtained along the rail-to-injector pipe. In fact, if the required injected mass $M_{inj,ref}$ is lower than 5 mg, one pressure signal is enough to evaluate the inlet flow-rate, while if $M_{inj,ref} > 5$ mg or a pilot-main schedule is considered, two pressure time histories are needed (the measuring principle is the same described in Chap. 3). The obtained instantaneous flow-rate along the injector feeding

pipe is integrated between two optimized time instants and therefore the inlet mass is evaluated. This fuel mass, based on the mass conservation equation, results to be well correlated with the injected mass, hence a piecewise linear correlation is obtained, and it results to be independent with respect to the fuel temperature, the rail pressure level and the pump speed.

During an engine cycle the inlet mass is measured and, by means of the correlation, the injected mass is estimated. The difference between the target injected mass and the estimated one is evaluated and this is used as the input of a PID controller: based on the evaluated error, the ET is corrected to compensate the inaccuracy on the injected quantity.

The developed algorithm has been implemented on a NI PXI platform: it receives the two pressure signal and estimates the injected mass. This datum is sent to a Flexible ECU through a CAN cable. Both the innovative injected mass control strategy and the standard pressure control strategy have been implemented on the Flexible ECU, by means of the entire diesel injection system is controlled.

A CR system equipped with CRI 2.20 injector has been employed for single injection tests and has been used as a reference to investigate the advantages of the presented control strategy. Results have shown that for the Polito system (where the injected mass is controlled through the new control strategy) the inaccuracy on the injected mass is lower than 1 mg for all the thermal regimes considered and the different operating conditions (in terms of ET and p_{nom}), whereas the standard systems exhibits an error higher than 2 mg. The best performance of the Polito system has been experienced for the highest T_{tank}, especially with high values of p_{nom} and $M_{inj,ref}$. In fact, in line with the results of Chap. 2, the higher the fuel temperature and the nominal rail pressure are, the higher the nozzle fuel temperature is. The developed control strategy is sensitive to the nozzle fuel temperature, hence, it can compensate the inaccuracy on M_{inj}. Satisfactory results have been obtained also in terms of dynamic response to ramps and steps, in terms of p_{nom} and $M_{inj,ref}$, while no appreciable improvements have been achieved in terms of repeatability of the injected quantity.

Regarding the pilot-main injections, another correlation between the inlet and the injected mass has been obtained and used to estimated the effective overall injected mass. In this case, a CR system with CRI 2.18 injectors has

been considered. The well-known patter of the overall injected mass of a pilot-main injection with respect to the DT (where the injected mass dramatically increases in the short dwell-time range) has been significantly improved, in fact the error on the injected mass has been reduced below 2 mg over the entire DT range.

As far as the second strategy is concerned, the hydraulic injection duration is estimated by means of a TFA-based needle virtual sensor. It has been seen that the $ITL - M_{inj}$ correlation is not dependent on the fuel temperature, hence, if the injected mass is controlled by means of this correlation, the thermal regime effect can be compensated. The MIF trace obtained from the pressure signal measured along the rail-to-injector pipe is obtained and two time instants strictly related to the SOI and EOI have been identified. In fact, the former is represented by the first maximum experienced by the MIF after the current rise, the latter coincides with the absolute maximum of the MIF trace. By means of the $M_{inj} = M_{inj}(p_{nom}, ITL)$ correlation, an estimation of the injected mass is obtained by using the estimated injection duration. In terms of accuracy, it has been seen, for single injections, that the algorithm predicts the injected mass with an error lower than 1.5 mg. The sources of error can be identified in the inaccuracy of the ITL prediction and in the error related to the applied correlation. Future works will be focused on the improvement of the hydraulic injection duration and on the double injection schedules application.

In Chap. 5 the CF injection system has been analysed from both the experimental and the numerical point of view. At the beginning, a standard CR system layout has been considered and has been hydraulically characterized by taking into account different rail sizes. Regarding to single injections, no differences between the different accumulation volumes employed can be detected, while, for high values of injected mass, the system featuring the smallest accumulator presents an augmented injection rate and, for fixed ET and p_{nom}, an increased injected mass. Pertaining to the CF system, the one considered has a cross-shape accumulation volume of 10 cm^3, and the only evident difference is on the frequency of the free pressure waves travelling back and forth in the rail-to-injector pipe after an injection event.

Static leakages reduce with the rail volume for the CR system when a high nominal rail pressure is considered. In addition, no particular trends

with respect to the accumulator size can be noticed regarding to the dynamic leakage. For all the CR layouts, the cycle-to-cycle dispersion is within the acceptable limit, although it increases when V_{rail} is reduced. NOD and NCD do not vary for the different layouts.

Pertaining to the double injections, both pilot-main and main-after shots have been considered. The amplitude of oscillations with DT of the $V_{inj,main}$ (for pilot-main injections) and of $V_{inj,aft}$ (for main-after injections) for the CF system are similar to the one present in the CR systems and $V_{inj,main}$ oscillation amplitude has been reduced by means of gauged orifices installed at the CF accumulation volume.

By means of a 1D numerical diagnostic model the internal injector dynamics has been analysed. For the smallest rail size, the highest needle lift peak is reached, leading to an increased injection duration, for fixed ET and p_{nom}. Pertaining to a pilot-main injection, the augment in the $V_{inj,main}$ for the reduced rail size is ascribed to the higher pressure level in the delivery chamber at the start of the injection, due to the different ET_{pil} values for the different CR layouts.

In Chap. 6 an investigation on the influence of the unsteady friction in numerical simulation of transient high-pressure flows is shown. The Zielke mathematical model, which define the analytical formulation of the frequency dependent friction, has been analysed, together with the most popular approximation techniques, developed in the last decades to reduce the computational efforts required to take into account this friction contribution.

Two different layout have been considered in the numerical tests. In the first, a 2 m long pipe equipped with 3 pressure transducers has been used. The two pressure signals at the extremities have been assigned as boundary conditions of the pipe numerical model, while the one in the middle has been compared with the simulation results. In the second, a CR system with a 2 m long rail-to-injector pipe has been considered. A one-dimensional CR system numerical model has been used, with the rail pressure signal and the current time history to the injector as boundary conditions. The different unsteady friction models have been applied in the various submodels of the 1D diagnostic tool.

It has been observed that, if two pressure signals are provided as boundary conditions (as in the first layout) the effect of the unsteady friction is negligible.

In fact, the two pressures at the boundaries are able to restore, for each time instant, the correct pressure value at the extremities, hence, the inaccuracy due to the friction model technique is masked and all the numerical outcomes (included the one where only the steady friction is considered) are almost overlapped.

However, if the numerical simulation has only one pressure signal as boundary condition, evident benefits can be noticed if the frequency dependent friction is taken into account. A more accurate prediction of the free pressure waves amplitude (travelling back and forth along the injector feeding pipe) is achieved if this friction contribution is considered, however, no significant differences have been detected between the different models, for both the laminar and the turbulent ones (the maximum Reynolds number for the CR system, in the considered conditions, was around 10^4). As a conclusion, in high-pressure transient flow pipelines with $Re < 10^4$ and an aspect ratio lower than 800, frequency dependent friction can help to improve the numerical outcomes if only one pressure signal is assigned as boundary condition and the simplest model, i.e. the Trikha one, is recommanded for the unsteady friction modelling.

In Chap. 7 a new set of analytical equations for a polytropic flow in a constant cross-section pipe has been presented. For this flow, choking occurs for a Mach number equals to $\sqrt{m/\gamma}$. The results of the obtained analytical relations have been compared with the analytical solution of Fanno's flow. The value of m has been obtained by taking into account the flow properties at the pipe inlet and at the outlet of the Fanno flow solution.

The polytropic flow distributions faithfully reproduce the ones of the Fanno flow when the flow is subsonic at the duct inlet and the outlet Mach number is below $\sqrt{m/\gamma}$ ($m < \gamma$ for a subsonic flow). Moreover, the prediction of a subsonic flow is generally better than the one pertaining to a supersonic flow. However, if a flow is supersonic at the pipe inlet and the Mach at the duct exit is higher than $\sqrt{m/\gamma}$, the prediction is still satisfactory, even if the quality is lower than a non choked subsonic flow.

If the choking condition is reached, i.e. $\sqrt{m/\gamma} < Ma_2 \leq 1$ for a subsonic flow and $1 \leq Ma_2 < \sqrt{m/\gamma}$ for a supersonic flow, the standard polytropic model is not able to correctly simulate the considered flow since the outlet pressure cannot be reached. In these cases, the difference between L_{pol} and L_{Fanno}, which is representative of the prediction accuracy, increases.

A diabatic inviscid flow with a significant kinetic energy transfer, i.e. a Rayleigh flow, cannot be modelled by means of a polytropic approach.

If a variable m numerical model is used, the obtained flow distribution perfectly match with the ones obtained for a Fanno or a Rayleigh flow, including the choked flow conditions.

A comparison between the polytropic model and the numerical solutions pertaining to a diabatic viscous flow has been performed. For a subsonic flow, if the temperature does not experience any local maximum and $Ma_2 < \sqrt{m/\gamma}$, the polytropic prediction is satisfactory. A new analytical formula to evaluate the Mach number at which the flow experiences a local maximum in the temperature (Ma_{Tmax}) has been derived and validated. The standard polytropic approach has excellent performance if the inlet Mach number is higher than the Ma_{Tmax} or if $Ma_2 < Ma_{Tmax}$, in fact the constant m flow does not allow the presence of any local maximum in the temperature distribution.

References

[1] Fuquan Zhao, Kangda Chen, Han Hao, and Zongwei Liu. Challenges, potential and opportunities for internal combustion engines in china. *Sustainability*, 12(12):4955, Jun 2020.

[2] P. Arya F. Millo and F. Mallamo. Optimization of automotive diesel engine calibration using genetic algorithm techniques. *Energy*, 158:807–819, 2018.

[3] F. Leach, R. Ismail, M. Davy, A. Weall, and B. Cooper. The effect of a stepped lip piston design on performance and emissions from a high-speed diesel engine. *Applied Energy*, 215:679–689, 2018.

[4] C. Chen, W. Lee, L. Wang, Y. Chang, H. Yang, L. Young, J. Lu, Y. I. Tsai, M. Cheng, and J. K. Mwangi. Impact of high soot-loaded and regenerated diesel particulate filters on the emissions of persistent organic pollutants from a diesel engine fueled with waste cooking oil-based biodiesel. *Applied Energy*, 191:35–43, 2017.

[5] F. Yang, C. Yao, J. Wang, and M. Ouyang. Load expansion of a dieseline compression ignition engine with multi-mode combustion. *Fuel*, 171:5 – 17, 2016.

[6] Karthik Vakiti, Joel Deussen, Claude Pilger, Harsha K. Nanjundaswamy, Tamas Szailer, Michael Franke, Dean Tomazic, Korfer Thomas, Marcel Romijn, Kai Deppenkemper, and Giovanni Vagnoni. In-use compliance opportunity for diesel powertrains. In *SAE Technical Paper*. SAE International, 04 2018.

[7] Giulio Boccardo, Federico Millo, Andrea Piano, Luigi Arnone, Stefano Manelli, Simon Fagg, Paolo Gatti, Olaf Erik Herrmann, Dirk Queck, and Jost Weber. Experimental investigation on a 3000 bar fuel injection system for a scr-free non-road diesel engine. *Fuel*, 243:342 – 351, 2019.

[8] Z. Sun, G. Li, C. Chen, Y. Yu, and G. Gao. Numerical investigation on effects of nozzle's geometric parameters on the flow and the cavitation characteristics within injector's nozzle for a high-pressure common-rail DI diesel engine. *Energy Conversion and Management*, 89:843–861, 2015.

[9] V. Macián, R. Payri, Santiago Garcia Ruiz, M. Bardi, and A. H. Plazas. Experimental study of the relationship between injection rate shape and diesel ignition using a novel piezo-actuated direct-acting injector. *Applied Energy*, 118:100–113, 2014.

[10] Y. Bai, Li yun Fan, Xiu zhen Ma, H. Peng, and Enzhe Song. Effect of injector parameters on the injection quantity of common rail injection system for diesel engines. *International Journal of Automotive Technology*, 17:567–579, 2016.

[11] Y. Ma, L. Cui, X. Ma, and J. Wang. Optical study on spray combustion characteristics of pode/diesel blends in different ambient conditions. *Fuel*, 272:117691, 2020.

[12] H. Liu, Ma Jun-sheng, F. Dong, Y. Yang, X. Liu, Ma Gui-xiang, Z. Zheng, and M. Yao. Experimental investigation of the effects of diesel fuel properties on combustion and emissions on a multi-cylinder heavy-duty diesel engine. *Energy Conversion and Management*, 171:1787–1800, 2018.

[13] K. Nishida, W. Zhang, and T. Manabe. Effects of micro-hole and ultra-high injection pressure on mixture properties of d.i. diesel spray. *SAE Transactions*, 116:421–429, 2007.

[14] X. Wang, Z. Huang, W. Zhang, O. Kuti, and K. Nishida. Effects of ultra-high injection pressure and micro-hole nozzle on flame structure and soot formation of impinging diesel spray. *Applied Energy*, 88:1620–1628, 2011.

[15] S. Moon, Y. Gao, S. H. Park, J. Wang, N. Kurimoto, and Y. Nishijima. Effect of the number and position of nozzle holes on in- and near-nozzle dynamic characteristics of diesel injection. *Fuel*, 150:112–122, 2015.

[16] M. Kubota, K. Yoshida, H. Shoji, and H. Tanaka. A study of the influence of fuel temperature on emission characteristics and engine performance of compression ignition engine. *SAE technical paper*, 2002.

[17] G. Guangxin, Y. Zhu-lin, Z. Apeng, L. Sheng-hua, and W. Yanju. Effects of fuel temperature on injection process and combustion of dimethyl ether engine. *Journal of energy resources technology*, 135:422021–422025, 2013.

[18] M. N. Babadi, S. Kheradmand, and C. Bae. Experimental and computational investigation of diesel and gasoline injection in a direct injection compression ignition engine. *International Journal of Automotive Technology*, 21:23–32, 2020.

[19] R. Mamat, N. Abdullah, H. Xu, M. Wyszynski, and A. Tsolakis. Effect of fuel temperature on performance and emissions of a common rail diesel engine operating with rapeseed methyl ester (rme). *SAE technical paper*, 2009.

[20] R. Payri, J. M. García-Oliver, M. Bardi, and J. Manin. Fuel temperature influence on diesel sprays in inert and reacting conditions. *Applied Thermal Engineering*, 35:185–195, 2012.

[21] S. Anis and G. N. Budiandono. Investigation of the effects of preheating temperature of biodiesel-diesel fuel blends on spray characteristics and injection pump performances. *Renewable Energy*, 140:274–280, 2019.

[22] J. S. Park, J. H. Jang, and S. Park. Effect of fuel temperature on heavy fuel oil spray characteristics in a common-rail fuel injection system for marine engines. *Ocean Engineering*, 104:580–589, 2015.

[23] A. E. Elsharkawy. Transient thermal analysis of diesel fuel systems. *SAE International Journal of Materials and Manufacturing*, 5:461–472, 2012.

[24] A. Catania, A. Ferrari, M. Manno, and E. Spessa. Thermal effect simulation in high-pressure injection system transient flows. *SAE technical paper*, 2004.

[25] R. Payri, F. Salvador, M. Carreres, and M. Belmar-Gil. An investigation on the fuel temperature variations along a solenoid operated common-rail ballistic injector by means of an adiabatic 1d model. *SAE technical paper*, 2018.

[26] F. Salvador, J. Gimeno, M. Carreres, and M. Crialesi-Esposito. Experimental assessment of the fuel heating and the validity of the assumption of adiabatic flow through the internal orifices of a diesel injector. *Fuel*, 188:442–451, 2017.

[27] O. Armas, S. Martínez-Martínez, C. Mata, and C. Pacheco. Alternative method for bulk modulus estimation of diesel fuels. *Fuel*, 167:199–207, 2016.

[28] A. Ferrari and T. Zhang. Influence of the injector setup on digital and continuous injection rate-shaping performance in diesel engine passenger cars. *Energy Conversion and Management*, 205:112259, 2020.

[29] J. Kim, J. Lee, and K. Kim. Numerical study on the effects of fuel viscosity and density on the injection rate performance of a solenoid diesel injector based on amesim. *Fuel*, 256:115912, 2019.

[30] F. Salvador, M. Carreres, J. D. L. Morena, and E. Martínez-Miracle. Computational assessment of temperature variations through calibrated orifices subjected to high pressure drops: Application to diesel injection nozzles. *Energy Conversion and Management*, 171:438–451, 2018.

[31] A. E. Catania, A. Ferrari, and M. Manno. Development and application of a complete multijet common-rail injection-system mathematical model for hydrodynamic analysis and diagnostics. *ASME J. Eng. Gas Turbines Power*, 130(6):062809, 2008.

[32] E. O. Doebelin. *Measurement Systems Application and Design*. McGraw-Hill, 1990.

[33] KO Plache. Coriolis/gyroscopic flow meter. *American Society of Mechanical Engineers*, 1977.

[34] Zimmerman R. and Deeri D. *Turbine Flowmeter Handbook*. Flow Technology, Inc., 1977.

[35] Micro Motion. Coriolis flow and density management.". Technical report, Technical Report, 2007.

[36] American Society of Mechanical Engineers. Research Committee on Fluid Meters. *Fluid Meters: Their Theory and Application*. ASME, RCFM, 1971.

[37] Shercliff J. A. *The theory of electromagnetic flow-measurement*. CUP Archive, 1962.

[38] Durst F., Ismailov M., and Trimis D. Measurement of instantaneous flow rates in periodically operating injection systems. *Experiments in fluids*, 20(3):178–188, 1996.

[39] Ismailov M., Ishima T., Obokata T., Tsukagoshi M., and Kobayashi K. Visualization and measurements of sub-millisecond transient spray dynamics applicable to direct injection gasoline engine: Part3: Measurements of instantaneous and integrated flow rates in high pressure injection system using lda-based meter. *JSME International Journal Series B Fluids and Thermal Engineering*, 42(1):39–47, 1999.

[40] Kulite. Innovative piezoresistive transducers. 2007.

[41] W. Bosch. The fuel rate indicator: a new measuring instrument for display of the characteristics of individual injection. *SAE Transactions*, pages 641–662, 1967.

[42] AE Catania and A Ferrari. Advanced mathematical modeling of electronic unit-injector systems for heavy duty diesel engine application. *SAE International Journal of Commercial Vehicles*, 1(2008-01-1195):134–151, 2008.

[43] A. E. Catania and A. Ferrari. Development and performance assessment of the new-generation CF fuel injection system for diesel passenger cars. *Applied Energy*, 91:483–495, 2012.

[44] L. Wang, G. Li, C. Xu, X. Xi, X. Wu, and S. Sun. Effect of characteristic parameters on the magnetic properties of solenoid valve for high-pressure common rail diesel engine. *Energy Conversion and Management*, 127:656–666, 2016.

[45] Thomas Wintrich, J. Hammer, D. Naber, M. Raff, Claudius Rath, Andreas Stapelmann, Jürgen Meusel, Holger Gödeke, and K. Prevel. Motorsysteme. In Johannes Liebl and Christian Beidl, editors, *Internationaler Motorenkongress 2015*, pages 165–211, Wiesbaden, 2015. Springer Fachmedien Wiesbaden.

[46] A. Ferrari and A. Mittica. Response of different injector typologies to dwell time variations and a hydraulic analysis of closely-coupled and continuous rate shaping injection schedules. *Applied Energy*, 169:899–911, 2016.

[47] F. J. Salvador, P. Marti-Aldaravi, M. Carreres, and D. Jaramillo. An investigation on the dynamic behaviour at different temperatures of a solenoid operated common-rail ballistic injector by means of a one-dimensional model. Technical Report 2014-01-1089, SAE Technical Paper, 2014.

[48] R. Finesso, E. Spessa, and Y. Yang. Fast estimation of combustion metrics in DI diesel engines for control-oriented applications. *Energy Conversion and Management*, 112:254–273, 2016.

[49] C. A. MacCarley, W. D. Clark, and K. T. Nakae. An indirect sensing technique for closed-loop diesel fuel quantity control. *SAE transactions*, pages 188–196, 1990.

[50] F. Yan and J. Wang. Common rail injection system iterative learning control based parameter calibration for accurate fuel injection quantity control. *International Journal of Automotive Technology*, 12(2):149–157, 2011.

[51] F. Yan and J. Wang. In-cylinder oxygen mass fraction cycle-by-cycle estimation via a lyapunov-based observer design. In *Proceedings of the 2010 American Control Conference*, pages 652–657, 2010.

[52] U. Schmid, G. Krötz, and D. Schmitt-Landsiedel. A volumetric flow sensor for automotive injection systems. *Journal of Micromechanics and Microengineering*, 18(4):045006, 2008.

[53] K. Ishiduka, K. Uchiyama, K. Higuchi, N. Yamada, K. Takeuchi, and O. E. Herrmann. Further innovations for diesel fuel injection systems: Close-loop control of fuel quantity by i-Art & ultra high injection pressure. In *19th Aachen colloquium*, Aachen, 2010.

[54] K. Serizawa, D. Ueda, N. Mikami, Y. Tomida, and J. Weber. Realizing robust combustion with high response diesel injector with controlled diffusive spray nozzle and closed loop injection control. Technical Report 2017-01-0845, SAE Technical Paper, 2017.

[55] T. Miyaura, A. Morikawa, Y. Ito, K. Ishizuka, and T. Tsuiki. Development of diesel engine using new fuel injection system-direct monitoring of fuel injection pressure using injector with built-in sensor, and its applications. Technical Report 2013-01-1739, SAE Technical Paper, 2013.

[56] J. Hammer, M. Raff, and D. Naber. Advanced diesel fuel injection equipment–a never ending BOSCH story. In *14. Internationales Stuttgarter Symposium*, pages 31–45. Springer, 2014.

[57] P. Voigt, H. Schiffgens, C. Daveau, J. Ogé, J. Béduneau, G. Meissonier, C. Tapin, and X. Lalé. Delphi injector closed loop control strategy using the "Switch" technology for diesel passenger cars–injector hardware. In *10. Tagung Diesel-und Benzindirekteinspritzung 2016*, pages 41–66. Springer, 2017.

[58] Stefan Stojanovic, Andrew Tebbs, Stephen Samuel, and John Durodola. Cepstrum analysis of a rate tube injection measurement device. Technical Report 2016-01-2196, SAE Technical Paper, 2016.

[59] F. Sapio, A. Piano, F. Millo, and F. C. Pesce. Digital shaping and optimization of fuel injection pattern for a common rail automotive diesel engine through numerical simulation. Technical Report 2017-24-0025, SAE Technical Paper, 2017.

[60] S. Shuai, N. Abani, T. Yoshikawa, R. D. Reitz, and S. W. Park. Evaluation of the effects of injection timing and rate-shape on diesel low temperature combustion using advanced CFD modeling. *Fuel*, 88(7):1235–1244, 2009. Selected Papers from the 2007 World of Coal Ash Conference.

[61] S. d'Ambrosio and A. Ferrari. Potentialities of boot injection combined with after shot for the optimization of pollutant emissions, fuel consumption and combustion noise in passenger car diesel engines. *SAE International Journal of Engines*, 10(2):144–159, 2017.

[62] S. d'Ambrosio and A. Ferrari. Effects of pilot injection parameters on low temperature combustion diesel engines equipped with solenoid injectors featuring conventional and rate-shaped main injection. *Energy Conversion and Management*, 110:457–468, 2016.

[63] S. Busch, K. Zha, and P. C. Miles. Investigations of closely coupled pilot and main injections as a means to reduce combustion noise in a small-bore direct injection diesel engine. *International Journal of Engine Research*, 16(1):13–22, 2015.

[64] Y. Yang, Z. Peng, W. Zhang, and G. Meng. Parameterised time-frequency analysis methods and their engineering applications: A review of recent advances. *Mechanical Systems and Signal Processing*, 119:182–221, 2019.

[65] Z. Feng, M. Liang, and F. Chu. Recent advances in time–frequency analysis methods for machinery fault diagnosis: A review with application examples. *Mechanical Systems and Signal Processing*, 38(1):165–205, 2013.

[66] Z. Feng, W. Zhu, and D. Zhang. Time-frequency demodulation analysis via vold-kalman filter for wind turbine planetary gearbox fault diagnosis under nonstationary speeds. *Mechanical Systems and Signal Processing*, 128:93–109, 2019.

[67] A. Taghizadeh-Alisaraei, B. Ghobadian, T. Tavakoli-Hashjin, S. S. Mohtasebi, A. Rezaei-asl, and M. Azadbakht. Characterization of engine's combustion-vibration using diesel and biodiesel fuel blends by time-frequency methods: A case study. *Renewable Energy*, 95:422–432, 2016.

[68] A. Taghizadeh-Alisaraei and A. Mahdavian. Fault detection of injectors in diesel engines using vibration time-frequency analysis. *Applied Acoustics*, 143:48–58, 2019.

[69] S. Ji, X. Lan, J. Lian, H. Wang, M. Li, Y. Cheng, and W. Yin. Combustion parameter estimation for ICE from surface vibration using frequency spectrum analysis. *Measurement*, 128:485–494, 2018.

[70] A. Ferrari, F. Paolicelli, and P. Pizzo. The new-generation of solenoid injectors equipped with pressure-balanced pilot valves for energy saving and dynamic response improvement. *Applied Energy*, 151:367–376, 2015.

[71] J. Hammer, D. Naber, M. Raff, and D. Zeh. Bosch diesel fuel injection system – with modularity from entry up to high-end segment. In *9. Tagung Diesel- und Benzindirekteinspritzung 2014, Proceedings*, pages 1–15, Wiesbaden, 2015. Springer Vieweg.

[72] A. Ferrari, A. Mittica, and E. Spessa. Benefits of hydraulic layout over driving system in piezo-injectors and proposal of a new-concept CR injector with an integrated minirail. *Applied Energy*, 103:243–255, 2013.

[73] K. Zhang, Z. Xie, and M. Zhou. Model-based optimization and pressure fluctuation control of pressure reservoir in electrically controlled fuel injection system for single cylinder diesel engine. In *Proceedings of the ASME 2017 Internal Combustion Engine Division Fall Technical Conference*, Seattle, Washington, USA, October 15-18 2017.

[74] A Ferrari, F Paolicelli, and P Pizzo. Hydraulic performance comparison between the newly designed common feeding and standard common rail injection systems for diesel engines. *Journal of Engineering for Gas Turbines and Power*, 138(9), 2016.

[75] A. E. Catania, A. Ferrari, A. Mittica, and E. Spessa. Common rail without accumulator: Development, theoretical-experimental analysis

and performance enhancement at DI-HCCI level of a new generation FIS. Technical Report 2007-01-1258, SAE Technical Paper, 2007.

[76] N. Johnston, M. Pan, S. Kudzma, and P. Wang. Use of pipeline wave propagation model for measuring unsteady flow rate. *Journal of Fluids Engineering*, 136(3), 2014.

[77] Alan E. Vardy and Jim M. Brown. Approximation of turbulent wall shear stresses in highly transient pipe flows. *Journal of Hydraulic Engineering*, 133(11):1219–1228, 2007.

[78] P. Storli and T.K. Nielsen. Transient friction in pressurized pipes. i: Investigation of zielke's model. *Journal of Hydraulic Engineering*, 137(5):577–584, 2011.

[79] A. Ghodhbani and E. Haj Taïeb. A four-equation friction model for water hammer calculation in quasi-rigid pipelines. *International Journal of Pressure Vessels and Piping*, 151:54–62, 2017.

[80] S. He, C. Ariyaratne, and A.E. Vardy. A computational study of wall friction and turbulence dynamics in accelerating pipe flows. *Computers and Fluids*, 37(6):674–689, 2008.

[81] A. Adamkowski and M. Lewandowski. Experimental examination of unsteady friction models for transient pipe flow simulation. *Journal of Fluids Engineering*, 128:1351–1363, 2006.

[82] H. Ramos, D. Covas, A. Borga, and D. Loureiro. Surge damping analysis in pipe systems: modelling and experiments. *Journal of Hydraulic Research*, 42:413 – 425, 2004.

[83] J. Conejero, C. Lizama, and F. Rodenas. Dynamics of the solutions of the water hammer equations. *Topology and its Applications*, 203:67–83, 2016.

[84] A. Bergant, A. Simpson, and A. Tijsseling. Water hammer with column separation: A historical review. *Journal of Fluids and Structures*, 22:135–171, 2006.

[85] D. Covas, I. Stoianov, H. Ramos, N. Graham, C. Maksimovic, and D. Butler. Water hammer in pressurized polyethylene pipes: conceptual model and experimental analysis. *Urban Water Journal*, 1:177 – 197, 2004.

[86] J. Shu. Modelling vaporous cavitation on fluid transients. *arXiv: Fluid Dynamics*, 2014.

[87] A. Ferrari. Modelling approaches to acoustic cavitation in transmission pipelines. *International Journal of Heat and Mass Transfer*, 53:4193–4203, 2010.

[88] T. Fukuda, S. Ozawa, M. Iida, Toru Takasaki, and Y. Wakabayashi. Distortion of compression wave propagating through very long tunnel with slab tracks. *Jsme International Journal Series B-fluids and Thermal Engineering*, 49:1156–1164, 2006.

[89] X. Wang, M. Lambert, and A. Simpson. Detection and location of a partial blockage in a pipeline using damping of fluid transients. *Journal of Water Resources Planning and Management*, 131:244–249, 2005.

[90] X. Wang, M. Lambert, A. Simpson, J. Liggett, and J. Vítkovský. Leak detection in pipelines using the damping of fluid transients. *Journal of Hydraulic Engineering*, 128:697–711, 2002.

[91] M. Ferrante and B. Brunone. Pipe system diagnosis and leak detection by unsteady-state tests. 1. harmonic analysis. *Advances in Water Resources*, 26:95–105, 2003.

[92] A. Ferrari and P. Pizzo. Optimization of an algorithm for the measurement of unsteady flow-rates in high-pressure pipelines and application of a newly designed flowmeter to volumetric pump analysis. *ASME J. Eng. Gas Turbines Power*, 138(3):031604, 2016.

[93] A. Ferrari, Pietro Pizzo, and M. Rundo. Modelling and experimental studies on a proportional valve using an innovative dynamic flow-rate measurement in fluid power systems. *Proceedings of the Institution of Mechanical Engineers, Part C: Journal of Mechanical Engineering Science*, 232:2404 – 2418, 2018.

[94] F. Yang, Gang yan Li, J. Hua, Xingli Li, and T. Kagawa. A new method for analysing the pressure response delay in a pneumatic brake system caused by the influence of transmission pipes. *Applied Sciences*, 7:941, 2017.

[95] A. E. Catania, A. Ferrari, M. Manno, and E. Spessa. Experimental investigation of dynamics effects on multiple-injection common rail system performance. *ASME J. Eng. Gas Turbines Power*, 131(3):032806, 2008.

[96] A. Ferrari and P. Pizzo. Fully predictive common rail fuel injection apparatus model and its application to global system dynamics analyses. *International Journal of Engine Research*, 18(3):273–290, 2017.

[97] J. Anderson. *Modern Compressible Flow with Historical Perspective, 3rd ed.* McGraw-Hill, Boston, 2003.

[98] E. Urata. A flow rate equation for subsonic Fanno flow. *Proceedings of the Institution of Mechanical Engineers, Part C: Journal of Mechanical Engineering Science*, 227(12):2724–2729, 2013.

[99] D. C. Rennels and H. M. Hudson. *Pipe flow: A practical and comprehensive guide.* John Wiley & Sons, New York, 2012.

[100] M. Cavazzuti, M. A. Corticelli, and T. G. Karayiannis. Compressible fanno flows in micro-channels: An enhanced quasi-2d numerical model for turbulent flows. *International Communications in Heat and Mass Transfer*, 111:104448, 2020.

[101] W. M. Kirkland. A polytropic approximation of compressible flow in pipes with friction. *ASME J. Fluids Eng.*, 141(12), 2019.

[102] M. Cavazzuti and M. A. Corticelli. Numerical modelling of fanno flows in micro channels: a quasi-static application to air vents for plastic moulding. *Thermal Science and Engineering Progress*, 2:43–56, 2017.

[103] C.S. Landram. One-dimensional, steady compressible flow with friction factor and uniform heat flux at the wall specified. 1997.

[104] A. Nouri-Borujerdi and M. Ziaei-Rad. Simulation of compressible flow in high pressure buried gas pipelines. *International Journal of Heat and Mass Transfer*, 52(25):5751–5758, 2009.

[105] E. E. Michaelides and S. Parikh. The prediction of critical mass flux by the use of Fanno lines. *Nuclear Engineering and Design*, 75(1):117–124, 1983.

[106] S. Mekebel and J.C. Loraud. Natural gas transport in pipes; unsteady flow modelization and experimentation. *J. Entropie*, 19(11):18–25, 1983.

[107] Subodh D. Deodhar, Hardik B. Kothadia, K.N. Iyer, and S.V. Prabhu. Experimental and numerical studies of choked flow through adiabatic and diabatic capillary tubes. *Applied Thermal Engineering*, 90:879–894, 2015.

[108] N. Agrawal and S. Bhattacharyya. Adiabatic capillary tube flow of carbon dioxide in a transcritical heat pump cycle. *International journal of Energy Research*, 31(11):1016–1030, 2007.

[109] N. S. Kumar and K. T. Ooi. One dimensional model of an ejector with special attention to fanno flow within the mixing chamber. *Applied Thermal Engineering*, 65(1-2):226–235, 2014.

[110] M. Cioffi, E. Puppo, and A. Silingardi. Fanno design of blow-off lines in heavy duty gas turbine. In *ASME Turbo Expo 2013: Turbine Technical Conference and Exposition*, San Antonio, Texas, USA, 2013. American Society of Mechanical Engineers Digital Collection.

[111] D. Kawashima and Y. Asako. Data reduction of friction factor of compressible flow in micro-channels. *International Journal of Heat and Mass Transfer*, 77:257–261, 2014.

[112] M. Cavazzuti, M. A. Corticelli, and T. G. Karayiannis. Compressible fanno flows in micro-channels: An enhanced quasi-2d numerical model for laminar flows. *Thermal Science and Engineering Progress*, 10:10–26, 2019.

[113] E. N. Sieder and G. E. Tate. Heat transfer and pressure drop of liquids in tubes. *Industrial and Engineering Chemistry*, 28(12):1429–1435, 1936.

[114] F.W. Dittus and L.M.K. Boelter. Heat transfer in automobile radiators of the tubular type. *International Communications in Heat and Mass Transfer*, 12(1):3–22, 1985.

[115] Z.Y. Guo and X.B. Wu. Compressibility effect on the gas flow and heat transfer in a microtube. *International Journal of Heat and Mass Transfer*, 40(13):3251–3254, 1997.

[116] C.Forbes Dewey. A correlation of convective heat transfer and recovery temperature data for cylinders in compressible flow. *International Journal of Heat and Mass Transfer*, 8(2):245–252, 1965.

[117] J. M. Cardemil and S. Colle. A general model for evaluation of vapor ejectors performance for application in refrigeration. *Energy Conversion and Management*, 64:79–86, 2012.

[118] W. F. Stoecher and J. W. Jones. Refrigeration and air conditioning, 1982.

[119] S. K. Chan and W. A. Woods. On Rayleigh and Fanno flows of homogeneous equilibrium two-phase fluids. *International Journal of Heat and Fluid Flow*, 13(3):273–281, 1992.

[120] A. Corvaglia, A. Ferrari, M. Rundo, and O. Vento. Three-dimensional model of an external gear pump with an experimental evaluation of the flow ripple. *Proceedings of the Institution of Mechanical Engineers, Part C: Journal of Mechanical Engineering Science*, 2020.

[121] A. Ferrari, C. Novara, E. Paolucci, O. Vento, M. Violante, and T. Zhang. Design and rapid prototyping of a closed-loop control strategy of the injected mass for the reduction of CO_2, combustion noise and pollutant emissions in diesel engines. *Applied Energy*, 232:358–367, 2018.

[122] A. Ferrari, C. Novara, E. Paolucci, O. Vento, M. Violante, and T. Zhang. A new closed-loop control of the injected mass for a full exploitation of digital and continuous injection-rate shaping. *Energy Conversion and Management*, 177:629–639, 2018.

[123] Z. Jin, O. Vento, T. Zhang, A. Ferrari, A. Mittica, L. Ouyang, and S. Tan. Numerical-experimental optimization of the common-feeding injection system concept for application to light-duty commercial vehicles. *Journal of Energy Resources Technology*, 143(12):122304, 2021.

[124] A. Ferrari and O. Vento. Influence of frequency-dependent friction modeling on the simulation of transient flows in high-pressure flow pipelines. *ASME J. Fluids Eng.*, 142(8):081205, 2020.

[125] J. Seob Kim and N. Radheshyam Singh. A novel adiabatic pipe flow equation for ideal gases. *ASME J. Fluids Eng.*, 134(1), 2012.

[126] J. Christians. Approach for teaching polytropic processes based on the energy transfer ratio. *International Journal of Mechanical Engineering Education*, 40(1):53–65, 2012.

[127] A. Ferrari, O. Vento, and T. Zhang. The polytropic approach in modeling compressible flows through constant cross-section pipes. *Journal Fluids Engineering*, 143(9), 2021.

[128] A. Ferrari and T. Zhang. Benchmark between Bosch and Zeuch method–based flowmeters for the measurement of the fuel injection rate. *International Journal of Engine Research*, in press, 2019.

[129] Blackburn J.F., Reethof G., and Shearer J.L. *Fluid power control*. MIT press, 1960.

[130] R. Payri, F. Salvador, M. Carreres, and J. D. L. Morena. Fuel temperature influence on the performance of a last generation common-rail diesel ballistic injector. part ii: 1d model development, validation and analysis. *Energy Conversion and Management*, 114:376–391, 2016.

[131] A. Ferrari. Fluid dynamics of acoustic and hydrodynamic cavitation in hydraulic power systems. *Proceedings of the Royal Society A: Mathematical, Physical and Engineering Sciences*, 473, 2017.

[132] D. McCloy and H. R. Martin. *Control of fluid power : analysis and design*. Ellis Horwood Limited, 1980.

[133] W. Nurick. Orifice cavitation and its effect on spray mixing. *Journal of Fluids Engineering-transactions of The Asme*, 98:681–687, 1976.

[134] R. Payri, J. M. García, F. Salvador, and J. Gimeno. Using spray momentum flux measurements to understand the influence of diesel nozzle geometry on spray characteristics. *Fuel*, 84:551–561, 2005.

[135] J. Zhao, L. Grekhov, and P. Yue. Limit of fuel injection rate in the common rail system under ultra-high pressures. *International Journal of Automotive Technology*, 21:649–656, 2020.

[136] A. E. Catania, A. Ferrari, M. Manno, and E. Spessa. A comprehensive thermodynamic approach to acoustic cavitation simulation in high-pressure injection systems by a conservative homogeneous two-phase barotropic flow model. *Journal of Engineering for Gas Turbines and Power*, 128(2), 2006.

[137] A. E. Catania and A. Ferrari. Development and assessment of a new operating principle for the measurement of unsteady flow rates in high-pressure pipelines. *Flow Measurement and Instrumentation*, 20(6):230–240, 2009.

[138] A. Ferrari and F. Paolicelli. An indirect method for the real-time evaluation of the fuel mass injected in small injections in common rail diesel engine. *Fuel*, 191:322–329, 2017.

[139] A. Ferrari. Injection system, apparatus and method for controlling the quantity of fuel injected. *Patent Application N. IB2017/050370*, 2017.

[140] S. Busch, K. Zha, P. C. Miles, A. Warey, F. Pesce, R. Peterson, and A. Vassallo. Experimental and numerical investigations of close-coupled pilot injections to reduce combustion noise in a small-bore diesel engine. *SAE International Journal of Engines*, 8(2):660–678, 2015.

[141] H. Akiyama, H. Yuasa, A. Kato, T. Saiki, K. Sanada, and N. Kado. Precise fuel control of diesel common-rail system by using OFEM. Technical Report 2010-01-0876, SAE Technical Paper, 2010.

[142] F. J. Salvador, J. Gimeno, M. Carreres, and M. Crialesi-Esposito. Fuel temperature influence on the performance of a last generation common-rail diesel ballistic injector. part i: Experimental mass flow rate measurements and discussion. *Energy Conversion and Management*, 114:364–375, 2016.

[143] A. Ferrari and F. Paolicelli. A virtual injection sensor by means of time frequency analysis. *Mechanical Systems and Signal Processing*, 116:832–842, 2019.

[144] A. Ferrari, A. Mittica, F. Paolicelli, and P. Pizzo. Hydraulic characterization of solenoid-actuated injectors for diesel engine common rail system. *Energy Procedia*, 101:878–885, 2016.

[145] M. Baratta, A. Catania, and A. Ferrari. Hydraulic circuit design rules to remove the dependence of the injected fuel amount on dwell time in multijet CR systems. *ASME J. Eng. Gas Turbines Power*, 130:121104, 2008.

[146] A. Ferrari and A. Mittica. Fem modeling of the piezoelectric driving system in the design of direct-acting diesel injectors. *Applied Energy*, 99:471–483, 2012.

[147] A. E. Catania, A. Ferrari, and E. Spessa. Temperature variations in the simulation of high-pressure injection-system transient flows under cavitation. *International Journal of Heat and Mass Transfer*, 51:2090–2107, 2008.

[148] W. Zielke. Frequency-dependent friction in transient pipe flow. *ASME J. Basic Eng.*, 90(1):109–115, 1968.

[149] Milton Abramowitz and Irene A. Stegun. *Handbook of Mathematical Functions with Formulas, Graphs, and Mathematical Tables - 9^{th} edition.* Dover, New York, 1964.

[150] A. K. Trikha. An Efficient Method for Simulating Frequency-Dependent Friction in Transient Liquid Flow. *Journal of Fluids Engineering*, 97(1):97–105, 03 1975.

[151] T. Kagawa, I. Y. Lee, A. Kitagawa, and T. Taakenaka. High speed and accurate computing method of frequency-dependent friction in laminar pipe flow for characteristics methods. *Trans. Jpn. Soc. Mech. Eng. Ser. B*, 49(447):2638–2644, 1983.

[152] G. A. Schohl. Improved approximate method for simulating frequency-dependent friction in transient laminar flow. *Journal of Fluids Engineering*, 115(3):420–424, 09 1993.

[153] J. Shu, K. A. Edge, C. R. Burrows, and S. Xiao. Transmission line modelling with vaporous cavitation. pages 1–9, 1993. ASME WAM ; Conference date: 01-01-1993.

[154] A.E. Vardy and J.M.B. Brown. Transient turbulent friction in smooth pipe flows. *Journal of Sound and Vibration*, 259(5):1011–1036, 2003.

[155] A. H. Shapiro. *The dynamics and thermodynamics of compressible fluid flow. Vol. 1.* John Wiley & Sons, New York, 1953.

[156] A. Ferrari and A. Mittica. Thermodynamic formulation of the constitutive equations for solids and fluids. *Energy Conversion and Managements*, 66:77–86, 2013.

[157] E. F. Toro. *Riemann solvers and numerical methods for fluid dynamics: a practical introduction, 3rd ed.* Springer Verlag, Heidelberg, 2009.

[158] R.D. Zucker and O. Biblarz. *Fundamentals of Gas Dynamics, 3rd Edition.* Wiley, New York, 2019.

[159] A. Ferrari. *Fondamenti di Termofluidodinamica per le Macchine, Vol. I.* CittàStudi, Biella, 2018.